Alma Mater Studiorum – Università di Bologna

DOTTORATO DI RICERCA IN

GEOFISICA

Ciclo XXXII

**Settore Concorsuale:** 02/C1

**Settore Scientifico Disciplinare:** FIS/06

# ASSIMILATION OF RADAR REFLECTIVITY VOLUMES THROUGH A LETKF SCHEME FOR A HIGH-RESOLUTION NUMERICAL WEATHER PREDICTION MODEL

**Presentata da:** Thomas Gastaldo

**Coordinatore Dottorato**

Prof.ssa Nadia Pinardi

**Supervisore**

Dott.ssa Chiara Marsigli

**Co-Supervisore**

Prof. Federico Porcù

**Esame finale anno 2020**

# Abstract

Despite the continuous improvements in numerical weather prediction (NWP) models, the quantitative precipitation forecast (QPF) is still a challenge. A crucial role in the accuracy of QPF is played by data assimilation, the technique whereby initial conditions for an NWP model are generated by combining observations of the state of the atmosphere and a previous forecast of the model itself. For convective-scale data assimilation, the use of radar reflectivity volumes should be beneficial since these observations allow to catch small-scale features of the atmosphere and to capture the spatial and temporal evolution of precipitation systems. Nevertheless, up to now, few attempts have been made to directly assimilate reflectivities in an operational set-up, due to the large amount of computational resources needed and to several open issues which arise when dealing with radar data. Among them, particularly relevant are the length of the assimilation window, the estimation of the observation error and the set-up of the radar operator, which is employed to simulate equivalent reflectivity observations from the prognostic model fields. For these reasons, currently, reflectivity observations are assimilated only indirectly in operational NWP models, employing radar-estimated quantities like instantaneous precipitation.

In this work, the crucial aspects of the assimilation of reflectivity volumes are investigated. This is carried out using the COSMO-2I model, the configuration of the convection permitting model of the COnsortium for Small-scale MOdelling (COSMO) employed at the Regional Agency for Prevention, Environment and Energy of Emilia-Romagna region (ARPAE) to provide high resolution weather forecasts over Italy. The reflectivity volumes employed come from the Italian radar network and they are assimilated through a local ensemble transform Kalman filter (LETKF) scheme. Taking advantage of the results obtained from this investigation, a set-up for the direct assimilation of reflectivity volumes suitable for an operational implementation is defined. Accuracy of QPF and of other forecast model variables obtained with this set-up is compared to that obtained with the current operational set-up employed at ARPAE to generate the initial conditions of COSMO-2I, in which radar-estimated precipitation is assimilated through a latent heat nudging (LHN) scheme.

Results obtained in this work show that the use of assimilation cycles shorter than 1 hour is not beneficial, since the model has not the time to remove imbalances which arise at each initialization. Employing hourly cycles, a positive impact is observed when assimilating, for each radar, only the closest volume to analysis time. For the first time, an estimation of the spatial variability of the reflectivity observation error is provided in this study. However, despite estimated values are in accordance with expectations, their use in the assimilation procedure does not improve QPF accuracy compared to the use of a unique value for all reflectivities. Finally, regarding the comparison between the assimilation of reflectivity volumes and the assimilation of estimated precipitation, the former clearly outperforms the latter in particular in terms of QPF accuracy. Results of this comparison, which is the most extended ever performed in terms of number of forecasts involved and in the number of verification scores employed, suggest that time is ripe to directly assimilate reflectivity volumes in an operational framework using an ensemble Kalman filter (EnKF) scheme.

# Contents

# Chapter 1

# Introduction

Numerical weather prediction (NWP) models are widely employed in meteorological centres to produce forecasts of the state of the atmosphere. In particular, they play a key role in the forecast of precipitation (Cuo et al., 2011), which arouses a great interest due to the many applications in which it is involved, from the issue of severe weather warnings to decision making in several branches of agriculture, industry and transportation. Therefore, an accurate quantitative precipitation forecast (QPF) is of great value both for society and for economic activities.

In this light, the operational use of limited area NWP models which explicitly resolve convection has determined a step-change in capabilities for forecasting rainfall (Clark et al., 2016). Nevertheless, QPF is still a challenge since it is affected by uncertainties in timing, location and intensity (Cuo et al., 2011; Röpnack et al., 2013). These errors arise partly from the chaotic behaviour of the atmosphere and from shortcomings in the model physics (Berner et al., 2015), but the main factor which affects the quality of QPF, especially in the short range (3-12 hours), is the accuracy of initial conditions (Dixon et al., 2009; Clark et al., 2016).

In current operational NWP models, the initial condition, also referred to as the analysis state or, simply, the analysis, is produced by a data assimilation procedure. Data assimilation is the technique whereby observations are combined with an a-priori knowledge of the state of the atmosphere (background state or first guess), provided by the model, in order to produce the best possible estimate of the actual state of the atmosphere at a given time. In the last decades, different

assimilation schemes have been proposed and implemented operationally in meteorological centres around the world (Bannister, 2016; Gustafsson et al., 2018). The most employed schemes can be divided into two main families: those based on a variational approach, like three-dimensional variational data assimilation (3D-Var: Courtier et al., 1998) and four-dimensional variational data assimilation (4D-Var: Buehner et al., 2010b) and those based on the ensemble Kalman filter (EnKF: Evensen, 1994; Houtekamer and Mitchell, 1998). More recently, methods which combine the variational and the EnKF approaches have been proposed (EnVar schemes) in the hope of maximizing the benefits and eliminating the inadequacies of the separate methods (Bannister, 2016). Until now, EnVar schemes have been mostly applied to global-scale NWP but there are some attempts to employ them for operational convective-scale models, like Wu et al. (2017) in which, however, a global-scale ensemble is exploited to reduce computational costs. Furthermore, to overcome the hypotheses of linearity and the assumption of the Gaussian distribution of errors made in both variational and EnKF methods, fully nonlinear and non-Gaussian techniques, like the particle filter (PF; reviewed in Van Leeuwen, 2009), have been developed, but their operational implementation is still at a preliminary stage (Gustafsson et al., 2018).

Focusing on convective scale data assimilation in an operational framework, EnKF methods seem to be preferable to variational techniques (Schraff et al., 2016) since they determine explicitly the background error covariance which is highly flow-dependent. Furthermore, in a variational scheme it is not straightforward to update any variable of an NWP model since an explicit linear and adjoint relation to the control vector of prognostic variables is needed. In the last decades, several variants of EnKF have been suggested (for a survey refer to Meng and Zhang, 2011) and one of the most popular is the local ensemble transform Kalman filter (LETKF), proposed by Hunt et al. (2007). It is used operationally in several meteorological centres like at COMET (Bonavita et al., 2010) and at Deutscher Wetterdienst (DWD) and MeteoSwiss employing the version of the scheme (Schraff et al., 2016) developed for the COnsortium for Small-scale MOdelling (COSMO). Moreover, the LETKF scheme is used for research purposes at both the Japan Meteorological Agency (JMA; Miyoshi et al., 2010) and at the European Centre of Medium-Range Weather Forecasts (ECMWF; Hamrud et al., 2015).

Regardless the data assimilation algorithm employed, analysis accuracy is strictly dependent on the quality and amount of observations that can be assimilated. In particular, for convective-scale data assimilation the high resolution of the model demands dense observations at a suitable temporal and spatial resolution (Gustafsson et al., 2018). In this light, radar observations can be of great value. A radar instrument, by transmitting electromagnetic waves and measuring the returned echo, allows to derive some features about a target. In particular, weather radars can be used to measure the radial velocity and the reflectivity factor of an atmospheric volume. The latter, often called simply reflectivity, is a quantity determined by the drop-size distribution of precipitations. Since weather radars generally works in a volume scanning mode, that is they acquire at each azimuthal angle and at different elevation angles, they collect a large amount of observations which are highly dense in space (both horizontally and vertically) and in time.

Focusing on reflectivity observations, several attempts have been made to assimilate them both in idealized and operational set-ups. Regarding operational implementations, most of the works has concerned reflectivity-derived products. In particular, estimated precipitation has been assimilated by using empirical approaches, like latent heat nudging (LHN; Jones and Macpherson, 1997; Leuenberger and Rossa, 2007; Stephan et al., 2008) or humidity nudging (Sokol, 2009; Davolio et al., 2017), which can be coupled to both the variational and the EnKF techniques (e.g. Schraff et al., 2016). In other cases, reflectivity-derived latent heat tendencies (Benjamin et al., 2016) or relative humidity profiles (Wattrelot et al., 2014) have been employed. However, no operational applications of the direct assimilation of radar reflectivity volumes has been performed yet.

Regarding EnKF methods, the direct assimilation of reflectivity volumes arises a number of problems. Most of them are general issues of EnKF schemes but they become more crucial when employing radar data. One of this is the length of the assimilation window, that is the time interval in which observations are collected to be assimilated. In EnKF methods, a short window would be desirable to avoid that dynamical features leave the area where computed localized increments are significant (Buehner et al., 2010a). On the other hand, a too short window would lead to an increase of imbalances in the analysis, since the model has no the time to filter spurious gravity waves which are introduced at each initialization. When

reflectivity volumes are assimilated, the window length becomes even more crucial since these observations allow to catch small scale features of the atmosphere (Houtekamer and Zhang, 2016). In order to exploit the high temporal frequency of these data, which is essential to properly characterize fast developing and moving precipitation systems, it seems reasonable to employ short windows to assimilate, in each cycle, only observations collected very close to the analysis time. Conversely, the big amount of radar observations enhances the imbalance issue and this could lead to a severe degradation of analysis quality.

Another important aspect which needs to be considered is the observation error. As for any observation, it is determined by the sum of the measurement error and the representation error (Janjić et al., 2017). Since both of them are not known, the proper setting of its value is not straightforward and it can be estimated only in a statistical sense. Considering the amount of reflectivity data, a correct estimation of the observation error is crucial, since even a small departure from the actual value can have a large impact on the quality of the analyses. Moreover, a further challenge when dealing with dense measurements, as radar ones, is to estimate and take into account error covariances between pairs of observations. In fact, most operational assimilation schemes assumes that observations are independent among each other but this hypothesis is likely to be violated if dense data are employed. Finally, a specific task for the assimilation of reflectivity volumes is the accurate simulation of equivalent reflectivities from prognostic model variables in order to properly compare observations to the background state.

Despite the several open issues associated to the direct assimilation of reflectivity volumes, some studies have treated this topic employing an EnKF scheme. Studies in an idealized set-up, like Tong and Xue (2005), Xue et al. (2006), Sobash and Stensrud (2013) and Lange and Craig (2014), have shown a beneficial impact in assimilating reflectivities. Regarding real-data cases, some works have focused on the positive influence of reflectivity observations on the analysis quality, as Dowell et al. (2004), Dowell et al. (2011) and Jung et al. (2012). The impact on QPF accuracy has been investigated in few works, like Aksoy et al. (2010), Dong and Xue (2013) and Snook et al. (2015), showing an improvement up to lead time +3h. However, all of these have considered only a few case studies. A slight longer evaluation (one week with 29 deterministic forecasts) has been carried out in Bick

et al. (2016), confirming a positive impact in the very first few hours of forecast. Nevertheless, a long term assessment of the assimilation of reflectivity volumes, which is mandatory to evaluate whether its operational implementation is worthwhile, has not yet been carried out. Due to the increase in available computational resources, the time is ripe to assess which impact may have the assimilation of these observations in operation convection-permitting NWP models.

## Objective and plan of the thesis

The aim of the thesis can be summarized as follows:

*to investigate the critical aspects of assimilating in a local meteorological model radar reflectivity volumes using an ensemble Kalman filter scheme and to identify a suitable configuration which can be employed in an operational framework.*

This will be achieved by addressing more specific objectives:

1. to evaluate the impact of employing different assimilation window lengths or subsets of observations and to investigate the consequent arise of imbalances;

2. to estimate the reflectivity observation error and its impact on the data assimilation system;

3. to investigate how different configurations of the radar operator affect the simulation of equivalent reflectivities and their consequent impact on the assimilation procedure;

4. to evaluate if the assimilation of reflectivity volumes can improve forecast accuracy compared to the current widespread assimilation of estimated precipitation.

This thesis treats the topic using the convection permitting COSMO-2I model which is described in Chapter 2. The model, is employed operationally at the Regional Agency for Prevention, Environment and Energy of Emilia-Romagna region (ARPAE) to provide high resolution forecasts (with a 2.2 km horizontal resolution) over Italy. Observations are assimilated through a LETKF scheme implemented for

the COSMO model by the kilometric-scale ensemble data assimilation (KENDA) system (Schraff et al., 2016). Both the LETKF scheme and the KENDA system are described in Chapter 3, where an overview of data assimilation and in particular of EnKF methods is also provided. The process of radar measurement and its limitations are discussed in Chapter 4. In this chapter, also the simulation of equivalent reflectivities from COSMO-2I prognostic variables, which is carried out with the efficient modular volume scanning radar operator (EMVORADO; Zeng, 2013, Zeng et al., 2016), is described. Moreover, different ways in which radar data can be assimilated are presented, as well as the Italian radar network which is exploited in this study.

The first objective of the thesis is addressed in Chapter 5 considering assimilation cycles of 15, 30 and 60 minutes and two configurations in which only a subset of observations is assimilated through hourly cycles. The amount of generated imbalances is evaluated in terms of the domain average of the surface pressure tendency. Chapter 6 focuses on the second objective of this work. After a sensitivity assessment of the impact of the reflectivity observation error on the assimilation procedure, this error is estimated through the Desroziers et al. (2005) diagnostics as a function of the radar station and of the distance of observations from the station. Then, the estimated values are employed to assimilate reflectivities and results are compared to those obtained employing a unique value for all radar observations. Furthermore, spatial correlations between pairs of reflectivity observations are estimated. The third objective is considered in Chapter 7 in which some configurations of the EMVORADO operator are tested, varying the scattering theory and taking into account or not attenuation. Finally, the last objective is addressed in Chapter 8. Here the optimal set-up for the direct assimilation of reflectivity volumes, defined by exploiting the results of the previous chapters, is compared to the operational set-up in which radar-estimated precipitation is assimilated through LHN.

# Chapter 2

# The COSMO model

The COSMO model (Baldauf et al., 2011) is a non-hydrostatic limited-area model developed and maintained by the national and regional weather services of the COnsortium for Small-scale MOdelling (COSMO). Applicable on the meso-$\beta$ and meso-$\gamma$ scales, it is based on the primitive thermo-hydrodynamic equations describing compressible flows in a moist atmosphere. The equations are formulated in rotated geographical coordinates with terrain-following hybrid layers and they include various parametrization schemes to characterize physical processes which are not explicitly resolved.

The model is run by the members of the consortium for operational weather forecasting and by several other institutions for research applications. The COSMO-2I configuration, employed operationally at ARPAE to provide high resolution forecasts and used for all the experiments in the present study, has a horizontal resolution of 2.2 km which allows to resolve deep convention explicitly. The model domain, consisting of $576 \times 701$ horizontal grid points, covers Italy and part of the neighbouring countries, as shown in Figure 2.1. COSMO-2I employs 65 vertical layers and the model top is at a height of 22 km.

In this chapter, the main features of the COSMO model are briefly described: the governing equations with their corresponding approximations in Section 2.1, the numerical implementation in Section 2.2 and the parametrizations employed in this study in Section 2.3. A more detailed characterization of the model can be found in Doms and Baldauf (2018).

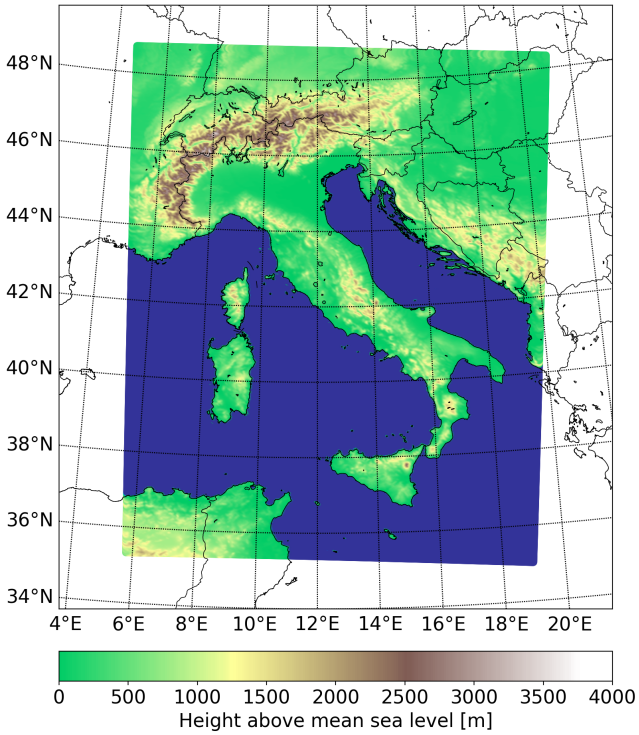


**Figure 2.1.** Domain of COSMO-2I with model orography.

## 2.1 The governing equations

The atmosphere can be considered as a multicomponent continuum which is constituted by dry air, water vapour and water in its liquid and solid state. In turns, the latter two may be further divided into various subcategories such as cloud droplets, raindrops, ice crystals, graupel or hail. Being subject to gravity and Coriolis forces, to heat, mass and momentum transfer and to phase changes of water, the general hydro-thermodynamic equations for compressible non-hydrostatic flows in a moist atmosphere without any scale approximations can be expressed

as:

$$\rho\frac{d\mathbf{v}}{dt} = -\nabla p + \rho\mathbf{g} - 2\boldsymbol{\Omega}\times(\rho\mathbf{v}) - \nabla\cdot\underline{\mathbf{t}} \tag{2.1}$$

$$\frac{dp}{dt} = -\frac{c_p}{c_v}p\nabla\cdot\mathbf{v} + \Big(\frac{c_p}{c_v} - 1\Big)Q_h + \frac{c_p}{c_v}Q_m \tag{2.2}$$

$$\rho c_p\frac{dT}{dt} = \frac{dp}{dt} + Q_h \tag{2.3}$$

$$\rho\frac{dq^x}{dt} = -\nabla\mathbf{J}^x + I^x \tag{2.4}$$

$$\rho = p[R_d(1-\alpha)T]^{-1} \tag{2.5}$$

Bold symbols are used to indicate vectors while bold underlined symbols represent second order tensors. The operator $\frac{d}{dt}$ is the total (Lagrangian) time derivative. The index $x$ refers to a specific constituent of the mixture, with

| | |
|---|---|
| $x = d$ | for dry air |
| $x = v$ | for water vapour |
| $x = l$ | for liquid water |
| $x = f$ | for water in solid state |

The list of symbols employed in Equations (2.1) - (2.5) is provided in Table 2.1.

Several modifications are necessary to make the equations for compressible non-hydrostatic flows solvable in practical cases. First of all, due to the presence of differential operators, these equations are valid for time and space increments approaching zero but, at the same time, the volume elements have to be large enough to allow statistical thermodynamics to be applied. These conditions restrict the direct application of Eqs. (2.1) - (2.5) to spatial scales of $\mathcal{O}(1\text{ cm})$ and to temporal scales of $\mathcal{O}(1\text{ s})$. Since grid spacings and time steps of these orders are computationally not feasible, basic equations are averaged over specified spatial and temporal scales. Accordingly, each meteorological variable is split up into a mean value, that is the grid scale value, and its deviation, often referred as the subgrid scale value. Furthermore, some assumptions are made to simplify the equations (Doms and Baldauf, 2018):

- molecular fluxes are neglected except for the diffusion fluxes of the liquid and solid forms of water;

**Table 2.1.** List of symbols employed in the general equations (2.1) - (2.5) and in the final set of model equations (2.8) - (2.13).

| Variable | Description |
|---|---|
| $c_p$, $c_v$ | specific heat of moist air at constant pressure/volume |
| $c_{pd}$, $c_{vd}$ | specific heat of dry air at constant pressure/volume |
| $D$ | divergence of $\mathbf{v}$ |
| $E_h = \sqrt{u^2 + v^2}$ | kinetic energy of horizontal motion |
| $\mathbf{g}$ | apparent acceleration of gravity |
| $\sqrt{\gamma}$ | variation of reference pressure with $\zeta$ |
| $I^x$ | sources or sinks of constituent $x$ |
| $\mathbf{J}^x$ | diffusion flux of constituent $x$ |
| $M_\psi$ | contribution from subgrid scale processes to prognostic variable $\psi$ |
| $\Omega$ | constant angular velocity of Earth rotation |
| $p$ | pressure |
| $P_{l,f}$ | precipitation fluxes |
| $q^x = \rho^x/\rho$ | mass fraction of constituent $x$ |
| $Q_h$ | diabatic heating/cooling rate |
| $Q_m$ | impact on pressure tendency of changes in humidity |
| $Q_T$ | diabatic heating due to subgrid scale processes |
| $R_d$ | gas constant for dry air |
| $\rho$ | density |
| $\rho^x$ | partial density of mixture constituent $x$ |
| $S^{l,f}$ | cloud microphysical sources and sinks due to phase changes |
| $t$ | time |
| $T$ | temperature |
| $T_v$ | virtual temperature |
| $\underline{\mathbf{t}}$ | stress tensor due to viscosity |
| $\mathbf{v} = (u, v, w)$ | wind velocity |
| $V_a$ | vertical component of the absolute vorticity |

- specific heat of moist air is approximated by the specific heat of dry air;
- the diabatic terms $Q_h$ and $Q_m$ are neglected;
- temperature changes due to buoyancy heat and moisture fluxes as well as the mean dissipation rate due to viscous stresses are neglected.

A further crucial aspect related to the set of equations (2.1) - (2.5) is the choice of the coordinate system. Due to the approximately spherical shape of the Earth, a suitable choice is to employ spherical coordinates. To avoid problems which arise

from the convergence of the meridians at poles, the coordinate system is rotated, meaning that the pole is tilted and positioned such that the equator runs through the centre of the model domain. Therefore, the thermo-hydrodynamic equations are transformed from the original Cartesian system ($x$, $y$, $z$) to the new rotated spherical coordinates ($\lambda$, $\phi$ $z$), where $\lambda$ is the geographical rotated longitude, $\phi$ is the geographical rotated latitude and $z$ is the geographical height above mean sea level.

The choice of the geographical height above mean sea level as vertical coordinate leads to a complex and costly definition of lower boundary conditions when surface terrain is considered. To overcome this issue, the model equations are formulated using a generalized terrain-following vertical coordinate $\zeta$. Then, this generalized coordinate is mapped to a user-specified coordinate $\tilde{\zeta}$ by a monotonic function $m$, that is $\tilde{\zeta} = m(\zeta)$. Three different options are available for the coordinate $\tilde{\zeta}$: a reference-pressure based coordinate, a Gal-Chen height-based coordinate (Gal-Chen and Somerville, 1975) and a height-based SLEVE (smooth level vertical) coordinate according to Schär et al., 2002. More precisely, the former two are formulated to define a hybrid system with terrain-following coordinate lines between the surface terrain height and a height $z = z_F$, above which the coordinate lines become flat horizontal lines. In COSMO-2I the hybrid Gal-Chen based vertical coordinate is employed; an example for a bell-shaped mountain is shown in Figure 2.2.

The calculation of the pressure gradient force in case of sloping surfaces, due to the use of a terrain-following vertical coordinate, may lead to large computational errors. To mitigate this problem, the thermodynamic variables are defined as the sums of base-state variables (which define the reference state and will be indicated with the subscript 0) and deviation from the base state (indicated with a prime). The reference state is assumed to be horizontally homogeneous, time invariant, hydrostatically balanced, dry and at rest. This means that variables $u$, $v$, $w$ and $q^x$ coincide with the deviation from the base state, while $T$, $p$ and $\rho$ are in the

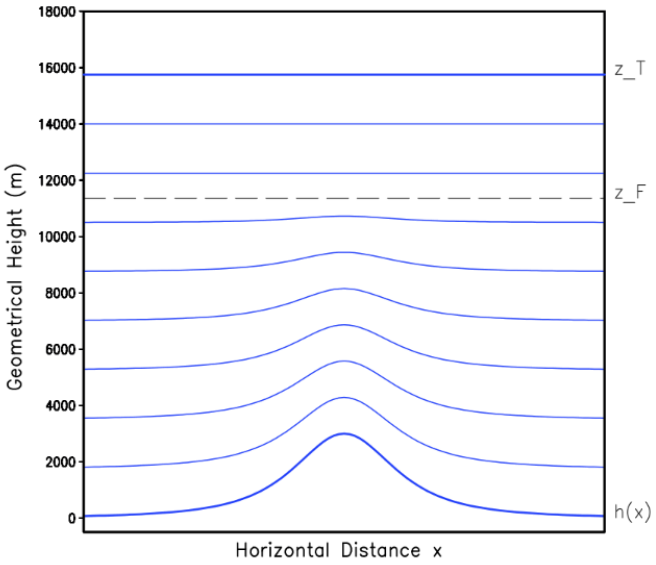


**Figure 2.2.** Sketch of terrain-following Gal-Chen height-based coordinate levels for a bell-shaped mountain with 3000 m height. Ten levels are depicted from the surface $h(x)$ to the the top $z_T = 15750m$. Above $z = z_F$ levels become flat horizontal (Doms and Baldauf, 2018).

form:

$$T = T_0(z) + T'(\lambda, \phi, z, t)$$
$$p = p_0(z) + p'(\lambda, \phi, z, t)$$
$$\rho = \rho_0(z) + \rho'(\lambda, \phi, z, t)$$

By employing this reference state, horizontal base state pressure gradient terms in the equation of motion are removed, reducing the computational error.

Introducing all the modifications and approximations described above into Eqs. (2.1) - (2.5), we obtain the final version of model equations, listed below.

- Horizontal wind velocity

$$\frac{\partial u}{\partial t} = -\left\{\frac{1}{a\cos\phi}\frac{\partial E_h}{\partial \lambda} - vV_a\right\} - \dot{\zeta}\frac{\partial u}{\partial \zeta} - \frac{1}{\rho a\cos\phi}\left(\frac{\partial p'}{\partial \lambda} - \frac{1}{\sqrt{\gamma}}\frac{\partial p_0}{\partial \lambda}\frac{\partial p'}{\partial \zeta}\right) + M_u \quad (2.6)$$

$$\frac{\partial v}{\partial t} = -\left\{\frac{1}{a}\frac{\partial E_h}{\partial \phi} + uV_a\right\} - \dot{\zeta}\frac{\partial v}{\partial \zeta} - \frac{1}{\rho a}\left(\frac{\partial p'}{\partial \phi} - \frac{1}{\sqrt{\gamma}}\frac{\partial p_0}{\partial \phi}\frac{\partial p'}{\partial \zeta}\right) + M_v \quad (2.7)$$

- Vertical wind velocity

$$\frac{\partial w}{\partial t} = -\left\{\frac{1}{a\cos\phi}\left(u\frac{\partial w}{\partial \lambda} + v\cos\phi\frac{\partial w}{\partial \phi}\right)\right\} - \dot{\zeta}\frac{\partial w}{\partial \zeta} + \frac{g}{\sqrt{\gamma}}\frac{\rho_0}{\rho}\frac{\partial p'}{\partial \zeta} + M_w + \\ + g\frac{\rho_0}{\rho}\left\{\frac{T - T_0}{T} - \frac{T_0 p'}{T p_0} + \left(\frac{R_v}{R_d} - 1\right)q^v - q^l - q^f\right\} \tag{2.8}$$

- Perturbation pressure

$$\frac{\partial p'}{\partial t} = -\left\{\frac{1}{a\cos\phi}\left(u\frac{\partial p'}{\partial \lambda} + v\cos\phi\frac{\partial p'}{\partial \phi}\right)\right\} - \dot{\zeta}\frac{\partial p'}{\partial \zeta} + g\rho_0 w - \frac{c_{pd}}{c_{vd}}pD \tag{2.9}$$

- Temperature

$$\frac{\partial T}{\partial t} = -\left\{\frac{1}{a\cos\phi}\left(u\frac{\partial T}{\partial \lambda} + v\cos\phi\frac{\partial T}{\partial \phi}\right)\right\} - \dot{\zeta}\frac{\partial T}{\partial \zeta} - \frac{1}{\rho c_{vd}}pD + Q_T \tag{2.10}$$

- Water vapour

$$\frac{\partial q^v}{\partial t} = -\left\{\frac{1}{a\cos\phi}\left(u\frac{\partial q^v}{\partial \lambda} + v\cos\phi\frac{\partial q^v}{\partial \phi}\right)\right\} - \dot{\zeta}\frac{\partial q^v}{\partial \zeta} - (S^l + S^f) + M_{q^v} \tag{2.11}$$

- Liquid and solid forms of water

$$\frac{\partial q^{l,f}}{\partial t} = -\left\{\frac{1}{a\cos\phi}\left(u\frac{\partial q^{l,f}}{\partial \lambda} + v\cos\phi\frac{\partial q^{l,f}}{\partial \phi}\right)\right\} - \dot{\zeta}\frac{\partial q^{l,f}}{\partial \zeta} - \frac{g}{\sqrt{\gamma}}\frac{\rho_0}{\rho}\frac{\partial P_{l,f}}{\partial \zeta} + S^{l,f} + M_{q^{l,f}} \tag{2.12}$$

- Total density of air

$$\rho = p\left\{R_d T\left[1 + \left(\frac{R_v}{R_d} - 1\right)q^v - q^l - q^f\right]\right\}^{-1} \tag{2.13}$$

The list of symbols employed in Eqs (2.8) - (2.13) is provided in Table 2.1. The calculation of all terms related to subgrid-scale processes $M_\psi$ (for each prognostic variable $\psi$), microphysical source and sink terms $S^{l,f}$, precipitation fluxes $P^{l,f}$ and radiative heating term $Q_T$ is done by physical parametrization schemes.

## 2.2 Numerical implementation

The set of model equations (2.8) - (2.13) is solved numerically using the finite difference method. For the spatial discretization of the equations, the terrain-following coordinate system in physical space is mapped to a regular rectangular grid. Therefore, the $(\lambda, \phi, \zeta)$-space is represented by a finite number of grid points with integer values $(i, j, k)$, where $i$ corresponds to the $\lambda$-direction, $j$ to the $\phi$-direction and $k$ to the $\zeta$-direction. Every grid point $(i, j, k)$ represents the centre of an elementary rectangular grid volume. Since an Arakawa-C/Lorenz staggered grid is employed, scalar variables are defined at the centre of a grid box while $u$, $v$ and $w$ components of wind velocity are defined on the corresponding box faces, as shown in Figure 2.3. Regarding the time discretization, the time-splitting third order Runge-Kutta approach of Wicker and Skamarock (2002) is adopted. By the time-splitting technique, the prognostic equations are separated in terms of fast processes related to acoustic wave modes and in terms of slow processes related to meteorological wave modes. Consequently, a small time step is used to update acoustically active terms while all other terms are computed only at larger time step, resulting in a more efficient time integration scheme.

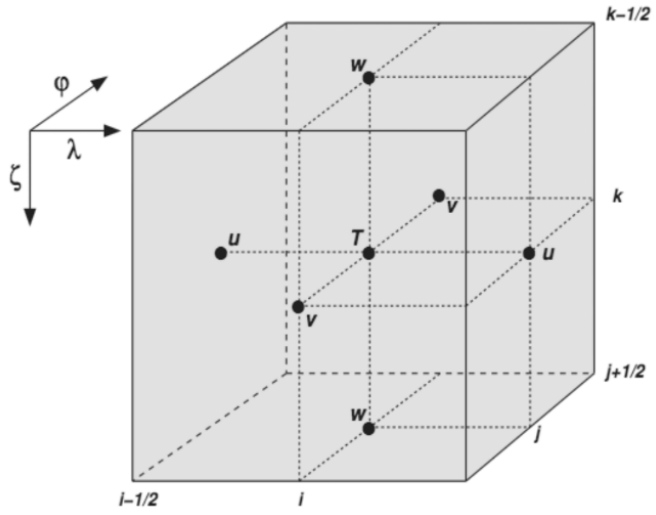


**Figure 2.3.** A grid box volume showing the Arakawa-C/Lorenz staggering of the dependent model variables (Doms and Baldauf, 2018).

In order to solve the set of differential equations, initial and boundary condi-

tions have to be specified. Initial condition, also called analysis, can be obtained by interpolating a coarser model analysis or forecast to the desired resolution or by employing a data assimilation scheme designed for the COSMO model, as the KENDA system described in Section 3.3. Regarding boundary conditions, in a limited area model as COSMO, only the lower boundary, represented by the Earth's surface, is physical while top and lateral boundaries are artificial and have to be specified. For operational applications, information on the variables at the lateral boundaries and their time evolution is obtained by interpolation from models with a larger domain. This procedure of nesting an high resolution limited area model in a low resolution driving model causes numerical problems, since the time evolution of the model variables is based on a set of equations differing from those of the driving model. To avoid this issue, a relaxation zone close to the boundaries is employed, following Davies (1976). In this zone, the variables of the high resolution model are gradually modified to blend them with the driving model variables. Finally, regarding top and bottom boundaries, the highest model level is treated as a rigid lid while the lower boundary condition at the ground is provided by the multi-layer soil model TERRA (Doms et al., 2011).

## 2.3 Physical parametrizations

The limited spatial and temporal resolution of operational NWP models do not allow to describe all atmospheric processes which span horizontal scales from molecular to planetary and temporal scales from fractions of second to years. For this reason, several simplifications are made to the general hydro-thermodynamic equations, as described in Section 2.1 for the COSMO model. Accordingly, an important part of physical processes in not explicitly revolved and need to be parametrized.

In the COSMO-2I configuration, the subgrid-scale turbulence parametrization is based on a prognostic equation for turbulent kinetic energy with a closure at level 2.5 (Raschendorfer, 2001). Radiative effects are described by the $\delta$-two-stream radiation scheme of Ritter and Geleyn (1992) for short-wave and long-wave fluxes. Due to the high resolution, in COSMO-2I only the shallow convection is parametrized, following the non-precipitating part of Tiedtke scheme

(Tiedtke, 1989), while deep convection is resolved explicitly. The microphysical parametrization is based on the Lin-type one moment scheme which includes all prognostic microphysical species (cloud water, cloud ice, rain, snow and graupel). The term "one moment" means that only the mass densities of the hydrometeors are predicted at each grid point, assuming a constant number concentration and a prescribed size distribution of the particles. Regarding snow and graupel, an exponential drop size distribution is assumed (Baldauf et al., 2011), while a two-parameter Gamma distribution is employed for rain drops. Cloud water and ice are supposed to be monodisperse.

# Chapter 3

# Data assimilation and the KENDA system

Numerical weather prediction is an initial value problem: the model simulates the atmospheric evolution given an estimate of the state of the atmosphere at a specific time and appropriate boundary conditions. Consequently, forecast accuracy is strongly dependent on the accuracy of initial conditions, also referred to as the analysis state. In this regards, data assimilation, which is the technique whereby observations are combined with an a-priori information of the state of the atmosphere to determine as accurately as possible the analysis state (Talagrand, 1997), plays a crucial role in NWP.

In this chapter, an overview of the fundamental concepts of data assimilation is provided in Section 3.1 and the way the problem can be handled with the Kalman filter and its variants is described in Section 3.2. One of these variants, the local ensemble transform Kalman filter (LETKF), is implemented for the COSMO model through the kilometre-scale ensemble data assimilation (KENDA) system, which main features are illustrated in Section 3.3. Finally, a description of the the operational data assimilation performed at ARPAE for the COSMO-2I model is provided in Section 3.4.

## 3.1 Overview

### Notation

In this chapter, boldface characters denote vectors (lower case) or matrices (upper case), while the use of the italicised font denotes a scalar. An apex and a subscript are associated to each vector and matrix. The apex indicates which field the variable belongs to (e.g. analysis, background etc.) while the subscript is a time index labelled with $k$. Unless otherwise stated, when the subscript is not indicated the time of validity of the variable is not relevant. Finally, calligraphic font (e.g. $\mathcal{M}$) denotes a nonlinear operator, while its linearised form is indicated with a bold capital letter.

### Full atmospheric state and model state

Numerical weather models are employed to estimate the (full) atmospheric state $\mathbf{w}^f$, which varies continuously in space and time. However, since numerical models handle only discrete representations of the atmospheric field, it is uniquely possible to estimate a projection of $\mathbf{w}^f$ in the discrete model space at specific times (Blayo et al., 2011). We refer to this projected (true) model state evaluated at time $t_k$ as $\mathbf{x}_k^t \in \mathbb{R}^n$. As any generic model state $\mathbf{x} \in \mathbb{R}^n$, it consists of all prognostic variables on each grid point, so the dimension $n$ is the product of the number of grid points times the number of variables (order $\mathcal{O}(10^8)$ in operational NWP). Another aspect to be considered is that the model can only approximately describe all atmospheric processes, mainly due to the simplifications introduced into the hydro-dynamic equations to make the problem solvable in practical cases. Therefore, an error $\boldsymbol{\eta} \in \mathbb{R}^n$ is introduced when propagating the true state $\mathbf{x}_k^t$, if available, from time $t_k$ to $t_{k+1}$ by applying the model $\mathcal{M} : \mathbb{R}^n \to \mathbb{R}^n$. In other words, the true state at time $t_{k+1}$ can be expressed as

$$\mathbf{x}_{k+1}^t = \mathcal{M}(\mathbf{x}_k^t) + \boldsymbol{\eta}_k \tag{3.1}$$

The error $\boldsymbol{\eta}$ is called the model error and its covariance is defined as $\mathbf{Q}_k = E[\boldsymbol{\eta}_k \boldsymbol{\eta}_k^T]$, where $E[\,\cdot\,]$ is the statistical expected value. In analogous fashion to Janjić et al. (2017), we can refer to the discrete realization of the full atmospheric state in

which only processes resolved by the model are taken into account as the true resolved model state $\mathbf{x}^r \in \mathbb{R}^n$.

### Observations

The full atmospheric field $\mathbf{w}^f$ can be observed by means of measuring instruments. The set of $p$ observations $\mathbf{y}_k^o \in \mathbb{R}^p$ available at time $t_k$ can be related to the true resolved model state (Janjić et al., 2017) by

$$\mathbf{y}_k^o = \mathcal{H}(\mathbf{x}_k^r) + \boldsymbol{\epsilon}_k^o \tag{3.2}$$

where $\mathcal{H} : \mathbb{R}^n \to \mathbb{R}^p$ is the observation operator and $\boldsymbol{\epsilon}_k^o \in \mathbb{R}^p$ is the observation error. The observation operator maps the model state into the observation space, allowing to compute the model equivalent of each observation. In case the observations are prognostic variables of the model, like temperature from a radiosonde or wind from a surface station, the operator $\mathcal{H}$ just interpolates model grid point values to the location of observations. Otherwise, for observations such as satellite radiance or radar reflectivity, it also includes physical laws and additional complex transformations to simulate what the specific instrument would measure if the state of the atmosphere was the one defined by $\mathbf{x}_k^r$.

The observation error consists of a measurement error $\boldsymbol{\epsilon}^m$ and a representation error $\boldsymbol{\epsilon}^r$ (Janjić et al., 2017), that is:

$$\boldsymbol{\epsilon}^o = \boldsymbol{\epsilon}^m + \boldsymbol{\epsilon}^r \tag{3.3}$$

The measurement error is due to errors introduced by the measuring instrument. The representation error takes into account three terms:

- error due to unresolved scales and processes in $\mathbf{x}^r$, that is the difference between a perfect (noise-free) observation and a perfect observation of the true resolved signal that we would like to have;
- error due to the operator caused by an approximation of the real measuring instrument with the observation operator $\mathcal{H}$;
- error due to pre-processing or quality control procedures associated to the

data assimilation system, that is associated to the model or to the assimilation algorithm.

Commonly, it is assumed that the observation error is unbiased, that is $E[\boldsymbol{\epsilon}^o] = 0$, and that its covariance $\mathbf{R} = E[\boldsymbol{\epsilon}^o(\boldsymbol{\epsilon}^o)^T]$ is known.

### Background state

In the data assimilation procedure, observations are combined to an a-priori knowledge of the state $\mathbf{x}^t$. In current operational NWP, this is provided by a previous short-range forecast of the model which defines a background state $\mathbf{x}^b \in \mathbb{R}^n$. To the background state is associated a background error $\boldsymbol{\epsilon}^b \in \mathbb{R}^n$ defined as

$$\epsilon^b = \mathbf{x}^b - \mathbf{x}^t \tag{3.4}$$

which, as well as the observation error, is generally assumed to be unbiased, i.e. $E[\boldsymbol{\epsilon}^b] = 0$, and its covariance $\mathbf{P}^b = E[\boldsymbol{\epsilon}^b(\boldsymbol{\epsilon}^b)^T]$ is assumed to be known.

### Analysis state

The result of the assimilation process is the analysis state, denoted $\mathbf{x}^a \in \mathbb{R}^n$. Again, the analysis error $\boldsymbol{\epsilon}^a \in \mathbb{R}^n$ is defined as

$$\epsilon^a = \mathbf{x}^a - \mathbf{x}^t \tag{3.5}$$

and the covariance matrix as $\mathbf{P}^a = E[\boldsymbol{\epsilon}^a(\boldsymbol{\epsilon}^a)^T]$.

The analysis state is obtained by combining observations with the background state at the corresponding time. Following a Bayesian approach (Hamill, 2006), finding the analysis at time $t_k$ consists in estimating the probability density function (pdf) of the true model state at the corresponding time $\mathbf{x}_k^t$, given the current and past observations. Denoting with $P(\,\cdot\,)$ the pdf and with $\boldsymbol{\psi}_k^o$ the vector which includes observations at most recent time $t_k$ as well as observations at all previous times, i.e. $\boldsymbol{\psi}_k^o = \{\mathbf{y}_k^o, \mathbf{y}_{k-1}^o, ..., \mathbf{y}_0^o\}$, this estimate is given by

$$P(\mathbf{x}_k^t|\boldsymbol{\psi}_k^o) \propto P(\mathbf{y}_k^o|\mathbf{x}_k^t)P(\mathbf{x}_k^t|\boldsymbol{\psi}_{k-1}^o) \tag{3.6}$$

Equation (3.6) expresses a recursive relationship: the posterior pdf for the true model state $\mathbf{x}_k^t$, given all the observations, is the product of the probability distribution for the observations $P(\mathbf{y}_k^o|\mathbf{x}_k^t)$ at time $t_k$ and the prior pdf $P(\mathbf{x}_k^t|\boldsymbol{\psi}_{k-1}^o)$. The latter is the pdf of the background state $\mathbf{x}_k^b$ and represents the pdf of the true model state at time $t_k$ given all the past observations up to time $t_{k-1}$.

The Bayesian approach to data assimilation is conceptually simple but it can not be applied to operational NWP. In fact, modelling pdf in an high dimensional space of $\mathcal{O}(10^8)$ can be very complex and the computational cost of multiplying two pdfs is unaffordable. Moreover, the analysis pdf, once derived via Eq. (3.6), has to be propagated in time to obtain the background estimate at the next analysis time when new observations are available. The evolution in time of the pdf can be computed using the model $\mathcal{M}$ via the Fokker-Planck equation (e.g. Gardiner, 1985) but, again, this is impossible in real case applications with current computational resources. Consequently, some assumptions and simplifications are made to make the data assimilation procedure applicable in real contexts. In the following, algorithms based on the Kalman filter are described.

## 3.2 Kalman filter

The Kalman filter (Kalman, 1960) is a recursive algorithm that determines the state variables of a noisy dynamical system given a set of noisy measurements observed over time. It has been widely employed in many contexts other than in meteorology, such as navigation, finance, fault detection and many others industrial applications (see Auger et al. (2013) for a review).

In the original formulation of the Kalman filter, it is assumed that both observation and background errors are unbiased and normally distributed and that they are not correlated with each other, that is

$$E[\boldsymbol{\epsilon}^o(\boldsymbol{\epsilon}^b)^T] = 0 \tag{3.7}$$

Furthermore, it is assumed that the model and the observation operators are linear; hereafter they will be denoted by $\mathbf{M}$ and $\mathbf{H}$, respectively. Under these assumptions, at each time $t_k$ the Kalman filter uses the available measurements $\mathbf{y}_k^o$ to find the

optimal estimate $\mathbf{x}_k^a$ of the state $\mathbf{x}_k^t$, i.e. the estimate for which the trace of the analysis error covariance matrix is minimum. This corresponds (Nichols, 2010) in finding, for each time $t_k$, the state which minimizes the cost function

$$\begin{aligned} J(\mathbf{x}_k) =& \frac{1}{2}[\mathbf{x}_k - \mathbf{x}_k^b]^T (\mathbf{P}_k^b)^{-1} [\mathbf{x}_k - \mathbf{x}_k^b] + \\ &+ \frac{1}{2}[\mathbf{y}_k^o - \mathbf{H}(\mathbf{x}_k)]^T \mathbf{R}_k^{-1} [\mathbf{y}_k^o - \mathbf{H}(\mathbf{x}_k)] + \frac{1}{2}\eta_k^T \mathbf{Q}_k^{-1} \eta_k \end{aligned} \tag{3.8}$$

If the model error is included in the background error, finding the optimal analysis is also equivalent (Nichols, 2010) to maximise the posteriori Bayesian pdf defined in Eq. (3.6), considering Gaussian distributions $\mathcal{N}(\mathbf{0}, \mathbf{R})$ for $P(\mathbf{y}_k^o | \mathbf{x}_k^t)$ and $\mathcal{N}(\mathbf{0}, \mathbf{P}^b)$ for $P(\mathbf{x}_k^t | \boldsymbol{\psi}_{k-1}^o)$.

The Kalman filter achieves this with a two steps process. In the forecast step, the analysis state $\mathbf{x}_{k-1}^a$ available at time $t_{k-1}$ and the estimate of its uncertainty $\mathbf{P}_{k-1}^a$ are propagated forward to time $t_k$ when a set of observations is available:

$$\mathbf{x}_k^b = \mathbf{M}\mathbf{x}_{k-1}^a \tag{3.9}$$

$$\mathbf{P}_k^b = \mathbf{M}\mathbf{P}_{k-1}^a \mathbf{M}^T + \mathbf{Q}_k \tag{3.10}$$

In the analysis step, the state estimate at time $t_k$, i.e. the background state $\mathbf{x}_k^b$, and the estimate of its uncertainty $\mathbf{P}_k^b$ are adjusted to the available observations $\mathbf{y}_k^o$, that is:

$$\mathbf{K}_k = \mathbf{P}_k^b \mathbf{H}^T \big(\mathbf{H}\mathbf{P}_k^b \mathbf{H}^T + \mathbf{R}_k\big)^{-1} \tag{3.11}$$

$$\mathbf{P}_k^a = \big(\mathbf{I} - \mathbf{K}_k \mathbf{H}\big)\mathbf{P}_k^b \tag{3.12}$$

$$\mathbf{x}_k^a = \mathbf{x}_k^b + \mathbf{K}_k \big(\mathbf{y}_k^o - \mathbf{H}\mathbf{x}_k^b\big) \tag{3.13}$$

where $\mathbf{K}_k$ is the optimal weight matrix at time $t_k$, also referred to as the Kalman gain. This two steps process is repeated cyclically each time new observations become available.

The effect of the Kalman gain is to apply observation innovations $\mathbf{y}_k^o - \mathbf{H}\mathbf{x}_k^b$ to correct the background state at relevant surrounding grid points. If the magnitude of $\mathbf{R}_k$ is small compared to that of $\mathbf{H}\mathbf{P}_k^b\mathbf{H}^T$, meaning that the observations are

more accurate than the a-priori information on the state of the atmosphere, the analysis estimate depends mostly on the observations. In other words, the analysis increment $\mathbf{K}_k\left(\mathbf{y}_k^o - \mathbf{H}\mathbf{x}_k^b\right)$ is large. On the contrary, if the magnitude of $\mathbf{R}_k$ is larger than that of $\mathbf{H}\mathbf{P}_k^b\mathbf{H}^T$, the background information is "trusted" more than the observations and the analysis increment is small.

The Kalman filter equations (3.9) - (3.13) can be written in many different but equivalent ways (Snyder, 2015). In particular, following Ghil and Malanotte-Rizzoli (1991) and Hunt et al. (2007), the analysis error covariance and the Kalman gain can be expressed as:

$$\mathbf{P}_k^a = \left[(\mathbf{P}_k^b)^{-1} + \mathbf{H}^T\mathbf{R}_k^{-1}\mathbf{H}\right]^{-1} \tag{3.14}$$

$$\mathbf{K}_k = \mathbf{P}_k^a\mathbf{H}^T\mathbf{R}_k^{-1} \tag{3.15}$$

Consequently, the analysis state can be rewritten in the form:

$$\mathbf{x}_k^a = \mathbf{x}_k^b + \mathbf{P}_k^a\mathbf{H}^T\mathbf{R}_k^{-1}\left(\mathbf{y}_k^o - \mathbf{H}\mathbf{x}_k^b\right) \tag{3.16}$$

This alternative formulation will be employed in Section 3.2.4 to derive the local ensemble transform Kalman filter (LETKF) equations.

### 3.2.1 Extended Kalman filter

In most practical cases, like when dealing with the atmosphere, both the model and the observation operator are nonlinear. The extended Kalman filter (EKF; Jazwinski, 1970) is one of the most widely used modification of the original Kalman filter to account for nonlinearity, In this formulation, the nonlinear model $\mathcal{M}$ is employed to propagate the analysis state in Eq. (3.9) and the nonlinear operator $\mathcal{H}$ is employed to compute the innovations in Eq. (3.13). In the other equations, the tangent linear operator (Jacobian) of $\mathcal{M}$ in the proximity of $\mathbf{x}_{k-1}^a$ and the tangent linear operator of $\mathcal{H}$ in the proximity of $\mathbf{x}_k^b$ are employed. Then, the operators $\mathbf{M}$

and $\mathbf{H}$ used in Eqs. (3.9) - (3.13) can be redefined as follows:

$$\mathbf{M} = \left.\frac{\partial \mathcal{M}}{\partial \mathbf{x}}\right|_{\mathbf{x}=\mathbf{x}_{k-1}^{a}} \tag{3.17}$$

$$\mathbf{H} = \left.\frac{\partial \mathcal{H}}{\partial \mathbf{x}}\right|_{\mathbf{x}=\mathbf{x}_{k}^{b}} \tag{3.18}$$

Bearing in mind this modification, the original set of Kalman filter equations (3.9) - (3.13) becomes:

$$\mathbf{x}_k^b = \mathcal{M}\mathbf{x}_{k-1}^a \tag{3.19}$$

$$\mathbf{P}_k^b = \mathbf{M}\mathbf{P}_{k-1}^a\mathbf{M}^T + \mathbf{Q}_k \tag{3.20}$$

$$\mathbf{K}_k = \mathbf{P}_k^b\mathbf{H}^T\big(\mathbf{H}\mathbf{P}_k^b\mathbf{H}^T + \mathbf{R}_k\big)^{-1} \tag{3.21}$$

$$\mathbf{P}_k^a = \big(\mathbf{I} - \mathbf{K}_k\mathbf{H}\big)\mathbf{P}_k^b \tag{3.22}$$

$$\mathbf{x}_k^a = \mathbf{x}_k^b + \mathbf{K}_k\big(\mathbf{y}_k^o - \mathcal{H}\mathbf{x}_k^b\big) \tag{3.23}$$

The EKF partly addresses the nonlinearity issue, but does not overcome all the limitations of the Kalman filter. First of all, errors are supposed to grow linearly in time and to be normally distributed. Both assumptions may be inappropriate for atmospheric data assimilation of quantities which are very sensitive to motions at small scales, such as moisture, cloud cover or reflectivity. In fact, in this case the time-scale of predictability is small and errors grow and saturate rapidly (Hamill, 2006). Similarly, if observations are not regularly available, error covariances estimated with tangent linear dynamics may grow rapidly without bound (Evensen, 1992). Another aspect to be considered is that the error statistics must be carefully estimated and monitored since they play a crucial role in defining the analysis. In particular, it can be very complicated to estimate model error covariance $\mathbf{Q}_k$ (Cohn and Parrish, 1991). Finally, the computational cost of EKF, despite much lower than that of the Bayesian approach, is still unaffordable in real case atmospheric data assimilation. mainly because of the linearisation of $\mathcal{M}$ and $\mathcal{H}$ and the computation of the adjoint model operator $\mathbf{M}^T$.

### 3.2.2 Ensemble Kalman filter

The Monte Carlo technique has been coupled to the Kalman filter to overcome most of the problems encountered with EKF. By this approach, called ensemble Kalman filter (EnKF; Evensen, 1994), an ensemble of model state vectors is employed to estimate the background error covariance. In combination to localization (see Section 3.2.3) it provides an approximation to the Kalman filter which is feasible for operational atmospheric data assimilation (Houtekamer et al., 2005). Moreover, since EnKF allows to account for the nonlinear growth of the background error, it may be able to provide more accurate analyses than the EKF in situations where nonlinearity is pronounced (Hamill, 2006).

Several variants of the EnKF have been proposed after its first introduction by Evensen (1994). The forecast step is the same for each of the various EnKF formulations while differences concern the analysis step. Regarding the former, an ensemble of $N_{ens}$ analyses states $\mathbf{x}_{k-1}^{a(i)}$ available at time $t_{k-1}$, where $i$ is the index of the ensemble member ranging from 1 to $N_{ens}$, is propagated to the next analysis time $t_k$ by using the nonlinear model $\mathcal{M}$:

$$\mathbf{x}_k^{b(i)} = \mathcal{M}\big(\mathbf{x}_{k-1}^{a(i)}\big), \qquad i = i, ..., N_{ens} \tag{3.24}$$

The ensemble of background states generated with Eq. (3.24) is then employed to estimate the background error covariance $\mathbf{P}_k^b$. Defining the background ensemble mean as its sample mean

$$\bar{\mathbf{x}}_k^b = \frac{1}{N_{ens}} \sum_{i=1}^{N_{ens}} \mathbf{x}_k^{b(i)}, \tag{3.25}$$

the background covariance is estimated with the sample covariance of the ensemble, that is:

$$\mathbf{P}_k^b = \frac{1}{N_{ens} - 1} \mathbf{X}_k^b (\mathbf{X}_k^b)^T \tag{3.26}$$

where $\mathbf{X}_k^b$ is the matrix which $i$-th column is the perturbation from the mean for the $i$-th member, i.e. $\mathbf{x}_k^{b(i)} - \bar{\mathbf{x}}_k^b$. Compared to the background error covariance of the EKF in Eq. (3.20), the estimation of $\mathbf{P}_k^b$ in the EnKF assumes a much easier and less costly form since it is not necessary to linearise the model and to compute its adjoint. However, the model error is not taken into account. Covariance inflation

can be employed to deal with it, as described in Section 3.2.3.

Regarding the analysis step, it can be formulated following two approaches which define two different types of EnKF schemes: stochastic filters and deterministic filters. For the rest of the chapter, only quantities at analysis time $t_k$ will be considered and so the subscript $k$ is dropped hereafter.

### Stochastic update algorithms

The main feature of these algorithms is that each member of the ensemble is updated to a different set of observations perturbed with random noise. Accordingly, the analysis state for the $i$-th member is given by

$$\mathbf{x}^{a(i)} = \mathbf{x}^{b(i)} + \mathbf{K}\big(\mathbf{y}^{o(i)} - \mathcal{H}\mathbf{x}^{b(i)}\big) \tag{3.27}$$

where $\mathbf{y}^{o(i)} = \mathbf{y}^{o} + \mathbf{y}^{'(i)}$ is the vector of perturbed observations, defined such that $\mathbf{y}^{'(i)} \sim \mathcal{N}(\mathbf{0}, \mathbf{R})$ and

$$\frac{1}{N_{ens}} \sum_{i=1}^{N_{ens}} \mathbf{y}^{'(i)} = 0 \tag{3.28}$$

The Kalman gain $\mathbf{K}$ has the same form of that defined in Eq. (3.21) for the EKF, but in this case $\mathbf{P}^b$ is estimated from the background ensemble via Eq. (3.26). Finally, the analysis error covariance is given by the sample covariance of the analysis ensemble

$$\mathbf{P}^a = \frac{1}{N_{ens} - 1} \mathbf{X}^a (\mathbf{X}^a)^T \tag{3.29}$$

where $\mathbf{X}^a$, in the same fashion as $\mathbf{X}^b$, is the matrix which $i$-th column is the perturbation from the mean for the $i$-th member of the ensemble, i.e. $\mathbf{x}^{a(i)} - \bar{\mathbf{x}}^a$.

Without modifications to the algorithm, the use of perturbed observations is necessary. In fact, due to the limited size of real case ensembles, the use of unperturbed observations would determine an underestimation of $\mathbf{P}^a$ which, in turns, would lead to a severe filter divergence (Burgers et al., 1998), as described in Section 3.2.3. In other words, the use of perturbed observations ensures that the analysis error covariance is the same, or at least close, to that defined by Eq. (3.12). However, spurious correlations between the background ensemble and perturbed observations may arise, leading to a degradation of analysis quality (Houtekamer

and Zhang, 2016).

#### Deterministic update algorithms

Algorithms in which random noise is not added to observations are referred to as deterministic, so named because if the background ensemble and the associated error statistics are known, the ensemble of analysis states will be completely known as well. In fact, according to Hamill (2006), they update in a way that generates the same analysis error covariance that would be obtained from the Kalman filter, i.e. by Eq. (3.12), assuming that the background error covariance $\mathbf{P}^b$ is modelled from the background ensemble via Eq. (3.26). Depending on how the analysis ensemble is constructed, several implementations of deterministic EnKF filters have been proposed, such as the ensemble transform Kalman filter (ETKF; Bishop et al., 2001), the ensemble square root filter (EnSRF; Whitaker and Hamill, 2002) and the ensemble adjustment Kalman filter (EAKF; Anderson, 2001). A general review is provided in Tippett et al. (2003) while a detailed description of the deterministic filter named local ensemble transform Kalman filter (LETKF; Hunt et al., 2007) is provided in Section 3.2.4.

Since spurious correlations between observations and background ensemble are avoided, deterministic filters are more accurate than stochastic filters (Whitaker and Hamill, 2002). However, they are more vulnerable to errors in the estimation of $\mathbf{P}^b$ due to the direct relationship, via Eq. (3.12), between background and analysis error covariances (Houtekamer and Zhang, 2016).

### 3.2.3 Issues related to the misrepresentation of $\mathbf{P}^b$

The accuracy of a Kalman filter algorithm is strictly dependent on the accuracy of observation and background error statistics. since they play a crucial role in defining the analysis and its error covariance. Considering the background error covariance, the use of an EnKF method appears advantageous compared to other Kalman filters, since the evolution of $\mathbf{P}^b$ is performed with the nonlinear model. However, two main issues can severely degrade the accuracy of the estimation of $\mathbf{P}^b$.

First of all, as observed in Section 3.2.2, differently to EKF the model error

is not taken into account when computing the background error covariance. This leads to an underestimation of $\mathbf{P}^b$ and, consequently, an underestimation of $\mathbf{P}^a$, which is then propagated forward in time. Hence, if the analysis errors are underestimated in one cycle, the background errors may be underestimated in the following cycle, under-weighting the new observations. The process can feed back on itself, determining eventually that new observations are no more able to correct the background state, which will diverge from the real state. This phenomenon is known as filter divergence (Houtekamer and Mitchell, 1998).

The second issue is that $\mathbf{P}^b$ can be affected by sampling errors due to the limited size of the ensemble. In fact, the size $N_{ens}$ determines the number of directions that the ensemble can span in the phase space, which is equal to $N_{ens}-1$. In an operational framework, $N_{ens}$ is limited by the computational costs and, currently, ensemble consisting of only some tens or a few hundreds of members can be employed. This is much smaller than both the number of model variables $N_m$, which is of order $\mathcal{O}(10^8)$, and than the number of observations $N_{obs}$, which can range from $\mathcal{O}(10^4)$ to $\mathcal{O}(10^6)$. The fact that $N_{ens} \ll N_m$ and $N_{ens} \ll N_{obs}$ is generally referred to as the rank problem (Houtekamer and Zhang, 2016). It leads to large sampling errors in estimating the background error covariances which can result, again, in filter divergence and in spurious correlations between very distant model grid points.

Localization is adopted to address the rank problem and its negative consequences on the effectiveness of EnKF algorithms, while covariance inflation is employed to deal with model error and other system errors which can lead to filter divergence.

### Localization

Localization consists in splitting the data assimilation problem into a number of quasi-independent local problems. For each of the local problems, the ensemble can span $N_{ens} - 1$ local directions of the phase space which guarantees a substantial increase of the effective dimensionality of the ensemble, leading to a much more accurate estimate of $\mathbf{P}^b$ (Houtekamer and Mitchell, 2005). Two approaches can be followed in implementing localization. One is the covariance localization

(Houtekamer and Mitchell, 2001) in which the background error covariance $\mathbf{P}^b$ is multiplied by a smooth correlation function which depends on the distance between two grid points; in this way correlations in $\mathbf{P}^b$ at a distance longer than a specified length are cut off. In the other, the observation localization (Ott et al., 2004), a function of the distance multiplies the inverse of the observation error covariance $\mathbf{R}^{-1}$ in order to assign a larger error to observations according to their distance from the considered grid point; in this way only nearby observations are employed to compute the local analysis.

For both covariance and observation localization, a common choice for the localization function is the correlation function introduced by Gaspari and Cohn (1999). It is a polynomial approximation of the Gaussian

$$G_0(d, l) = \exp\left(\frac{-d^2}{2l^2}\right) \tag{3.30}$$

where $d$ is the distance between two points (two grid points in case of covariance localization, an observation and a grid point in case of observation localization) and $l$ is a length scale or Gaussian half-width. Defining the parameter

$$c = \sqrt{\frac{10}{3}}l \tag{3.31}$$

the Gaspari-Cohn function approximates $G_0$ with a fifth order piecewise polynomial function for $d < 2c$, while for $d \geq 2c$ it is equal to 0

An example of how localization works is provided in Figure 3.1, taken from Hamill (2006). A global data assimilation system based on an EnKF scheme is considered. In Figure 3.1a the correlation of sea level pressure between a grid point in Western Pacific (black dot) and other grid points in the Northern Hemisphere is shown. This is obtained when a 25-member ensemble is employed and it clearly shows the presence of spurious correlations in several regions (especially Eastern Pacific and Northern Africa) since they do not appear when a 200-member ensemble is employed (Figure 3.1b). Therefore, these spurious correlations are a consequence of the limited size of the ensemble. When the covariance localisation function (Figure 3.1c) is applied to the 25-member ensemble, the resulting correlation (Figure 3.1d) more closely resembles that from the larger ensemble.

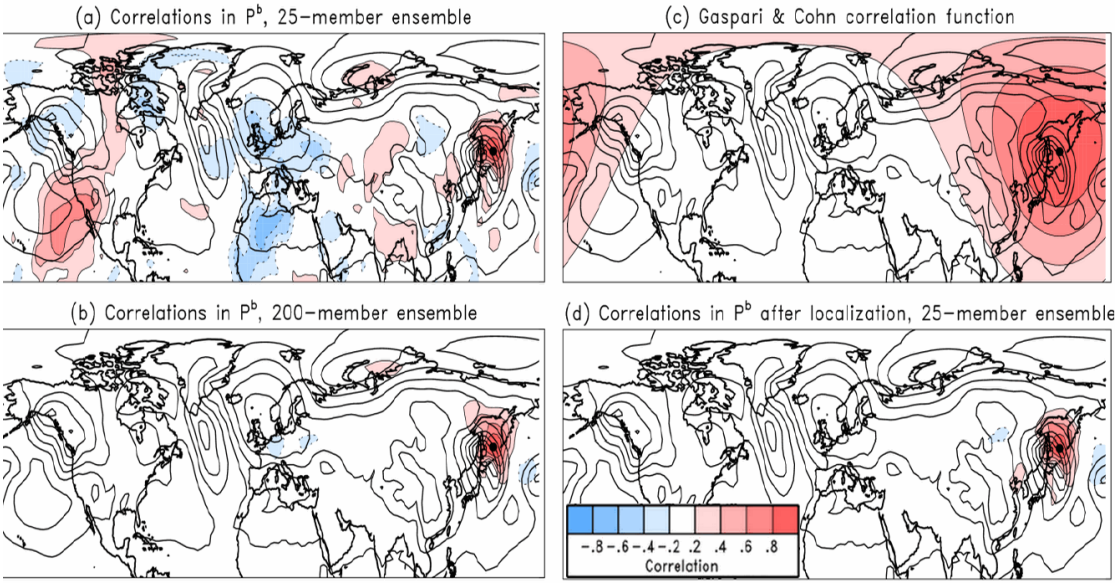


**Figure 3.1.** Illustration of covariance localisation taken from Hamill (2006). In panel (a), considering a 25-member ensemble, the correlation between a grid point in Western Pacific (black dot) and other grid points in the Northern Hemisphere is shown. Solid lines denote ensemble mean background sea-level pressure contoured every 8 hPa. In panel (b) the same correlation is shown when using a 200 member ensemble. In panel (c) the Gaspari-Cohn localization function is depicted. This is employed to perform covariance localization on the 25 members ensemble which determines the correlation shown in panel (d).

#### Covariance inflation

The term "covariance inflation" refers to several methods employed to increase the ensemble spread to take into account error sources which are not accurately described by the error statistics estimation of the algorithm. These error sources include the model error but also "data assimilation errors", like systematic sampling error, imbalances due to covariance localization, assumptions about observation error, spin-up issues and observation bias (Houtekamer and Zhang, 2016). In Section 3.3 the covariance inflation methods employed in this study are described.

### 3.2.4 Local ensemble transform Kalman filter

Hunt et al. (2007) proposed a deterministic EnKF algorithm named local ensemble transform Kalman filter (LETKF) which has become very popular in recent years due to its computational efficiency on parallel computing (Houtekamer and

Zhang, 2016). It is employed operationally in several meteorological centres like at COMET (Bonavita et al., 2010), at MeteoSwiss and Deutscher Wetterdienst (DWD; Schraff et al., 2016). Furthermore, it is used for research purposes at both the Japan Meteorological Agency (JMA; Miyoshi et al., 2010) and at the European Centre of Medium-Range Weather Forecasts (ECMWF; Hamrud et al., 2015). In this section, this algorithm is briefly described, following the original formulation provided by Hunt et al. (2007).

The forecast step of LETKF is the same of any EnKF algorithm and defined by Eqs. (3.24) and (3.26) which are reported here for convenience:

$$\mathbf{x}_k^{b(i)} = \mathcal{M}\big(\mathbf{x}_{k-1}^{a(i)}\big) \tag{3.32}$$

$$\mathbf{P}_k^b = \frac{1}{N_{ens}-1}\mathbf{X}_k^b(\mathbf{X}_k^b)^T \tag{3.33}$$

A key feature of the LETKF is the observation localization, as described in Section 3.2.3. In order to find the local analysis for each model grid point, we assume that localization has already been performed to select relevant observations and we consider $\mathbf{y}^o$, $\mathcal{H}$ and $\mathbf{R}$ to be truncated to these observations (the subscript $k$ has been dropped again since all variables that will be consider are defined at time $t_k$). Moreover, the LETKF assumes that the model is perfect (i.e. $\mathbf{Q} = \mathbf{0}$) and that a nonlinear operator $\mathcal{H}$ is employed. Bearing these assumptions in mind, this EnKF deterministic algorithm finds, for each model grid point, the analysis ensemble mean $\bar{\mathbf{x}}^a$ by minimizing the cost function for the Kalman filter defined in Eq. 3.8, modified to consider a perfect model and a nonlinear operator, that is

$$J(\mathbf{x}) = \frac{1}{2}[\mathbf{x}-\bar{\mathbf{x}}^b]^T(\mathbf{P}^b)^{-1}[\mathbf{x}-\bar{\mathbf{x}}^b] + \frac{1}{2}[\mathbf{y}^o-\mathcal{H}(\mathbf{x})]^T\mathbf{R}^{-1}[\mathbf{y}^o-\mathcal{H}(\mathbf{x})] \tag{3.34}$$

Once derived $\bar{\mathbf{x}}^a$ and the associated analysis error covariance $\mathbf{P}^a$, then the analysis ensemble with sample mean $\bar{\mathbf{x}}^a$ and sample covariance $\mathbf{P}^a$ is generated.

Regarding the minimization of the cost function in Eq. (3.34), it can be noticed that the maximum rank of $\mathbf{X}^b$ and $\mathbf{P}^b$ is $N_{ens}-1$, since the columns of $\mathbf{X}^b$ sum up to zero. Therefore, $\mathbf{P}^b$ is not invertible in the model space. However, in the space $S$ spanned by its columns, which is the space spanned by the ensemble perturbations (columns of $\mathbf{X}^b$), $\mathbf{P}^b$ is invertible. Hence, the cost function can be

minimized in $S$. To do this, an appropriate coordinate system has to be chosen. Clearly, the columns of $\mathbf{X}^b$ can not be used as a basis since they are not linear independent. However, $\mathbf{X}^b$ may be seen as a linear transformation from an $N_{ens}$ dimensional space $\widetilde{S}$ into the $N_{ens}-1$ dimensional space $S$. Accordingly, a vector $\mathbf{w}$ in $\widetilde{S}$ corresponds to the vector $\mathbf{X}^b\mathbf{w}$ in $S$ and to $\mathbf{x} = \bar{\mathbf{x}}^b + \mathbf{X}^b\mathbf{w}$ in the model space. Thus, in this perspective, $\mathbf{w}$ can be considered as a vector of weighting coefficients for $\mathbf{X}^b$.

Assuming that $\mathbf{w}$ is a Gaussian random vector with mean $\mathbf{0}$ and covariance $\widetilde{\mathbf{P}}^b = (N_{ens}-1)^{-1}\mathbf{I}$, then the corresponding model state $\mathbf{x} = \bar{\mathbf{x}}^b + \mathbf{X}^b\mathbf{w}$ is Gaussian with mean $\bar{\mathbf{x}}^b$ and covariance $\mathbf{P}^b$ as defined in Eq. (3.33). Therefore, the equivalent in space $\widetilde{S}$ of the cost function provided in Eq. (3.34) is:

$$\widetilde{J}(\mathbf{w}) = \frac{N_{ens}-1}{2}\mathbf{w}^T\mathbf{w} + \frac{1}{2}[\mathbf{y}^o - \mathcal{H}(\bar{\mathbf{x}}^b + \mathbf{X}^b\mathbf{w})]^T\mathbf{R}^{-1}[\mathbf{y}^o - \mathcal{H}(\bar{\mathbf{x}}^b + \mathbf{X}^b\mathbf{w})] \quad (3.35)$$

An important propriety is that if a vector $\bar{\mathbf{w}}^a$ minimizes the cost function $\widetilde{J}$, then $\bar{\mathbf{x}}^a = \bar{\mathbf{x}}^b + \mathbf{X}^b\bar{\mathbf{w}}^a$ minimizes $J$. Accordingly, if the analysis $\bar{\mathbf{w}}^a$ in space $\widetilde{S}$ is found, then the analysis $\bar{\mathbf{x}}^a$ for the ensemble mean in model space can be easily derived.

In order to find the analysis $\bar{\mathbf{w}}^a$ in space $\widetilde{S}$, the nonlinear operator $\mathcal{H}$ is first linearised about the background ensemble mean $\bar{\mathbf{x}}^b$ by applying it to the ensemble members $\mathbf{x}^{b(i)}$ and then interpolate. Accordingly, defining an ensemble of background observation vectors as

$$\mathbf{y}^{b(i)} = \mathcal{H}(\mathbf{x}^{b(i)}), \quad (3.36)$$

the linear approximation

$$\mathcal{H}(\bar{\mathbf{x}}^b + \mathbf{X}^b\mathbf{w}) \approx \bar{\mathbf{y}}^b + \mathbf{Y}^b\mathbf{w} \quad (3.37)$$

can be made, where $\bar{\mathbf{y}}^b$ is the mean of the background observation vectors and $\mathbf{Y}^b$ is the matrix whose $i$-th column is $\mathbf{y}^{b(i)} - \bar{\mathbf{y}}^b$. Thus, Eq. (3.35) can be approximated by

$$\widetilde{J}(\mathbf{w}) \approx \frac{N_{ens}-1}{2}\mathbf{w}^T\mathbf{w} + \frac{1}{2}[\mathbf{y}^o - \bar{\mathbf{y}}^b - \mathbf{Y}^b\mathbf{w}]^T\mathbf{R}^{-1}[\mathbf{y}^o - \bar{\mathbf{y}}^b - \mathbf{Y}^b\mathbf{w}] \quad (3.38)$$

This cost function is in the same form of the cost function for the Kalman filter in Eq. (3.8), with the background mean $\bar{\mathbf{w}}^b = 0$, background covariance $\widetilde{\mathbf{P}}^b = (N_{ens} - 1)^{-1}\mathbf{I}$ and $\mathbf{Y}^b$ playing the role of the observation operator. Therefore, the analysis state $\bar{\mathbf{w}}^a$ and error covariance $\widetilde{\mathbf{P}}^a$ in ensemble space are analogous to that defined for the Kalman filter by Eqs. (3.16) and (3.14) respectively, that is:

$$\bar{\mathbf{w}}^a = \widetilde{\mathbf{P}}^a (\mathbf{Y}^b)^T \mathbf{R}^{-1} \left(\mathbf{y}^o - \bar{\mathbf{y}}^b\right) \tag{3.39}$$

$$\widetilde{\mathbf{P}}^a = \left[(N_{ens} - 1)\mathbf{I} + (\mathbf{Y}^b)^T \mathbf{R}^{-1} \mathbf{Y}^b\right]^{-1} \tag{3.40}$$

By applying the linear transformation $\mathbf{X}^b$, the analysis ensemble mean and error covariance in model space are obtained:

$$\bar{\mathbf{x}}^a = \bar{\mathbf{x}}^b + \mathbf{X}^b \bar{\mathbf{w}}^a \tag{3.41}$$

$$\mathbf{P}^a = \mathbf{X}^b \widetilde{\mathbf{P}}^a (\mathbf{X}^b)^T \tag{3.42}$$

Note that all calculations have been done in the ensemble space, which is of much smaller dimension than both the model space and the observation space and this leads to a significant reduction in computational costs.

Once derived the analysis ensemble mean and error covariance, the analysis ensemble has to be generated, provided that its sample mean and covariance are equal to those defined by Eq. (3.41) and (3.42) respectively. The choice made by Hunt et al. (2007) is to generate the analysis ensemble perturbation by

$$\mathbf{X}^a = \mathbf{X}^b \mathbf{W}^a \tag{3.43}$$

where

$$\mathbf{W}^a = \left[(N_{ens} - 1)\widetilde{\mathbf{P}}^a\right]^{1/2} \tag{3.44}$$

This choice ensures that the sample covariance of the analysis ensemble is equal to Eq. (3.42) and that the sum of the columns of $\mathbf{X}^a$ is zero, meaning that the ensemble has sample mean $\bar{\mathbf{x}}^a$ defined via Eq. (3.41). Moreover, it guarantees that $\mathbf{W}^a$ depends continuously on $\widetilde{\mathbf{P}}^a$, ensuring that analysis ensembles in neighbouring grid points which have similar $\widetilde{\mathbf{P}}^a$ will not differ significantly. Due to this formulation, also the analysis ensemble can be constructed directly in space $\widetilde{S}$ by

adding $\bar{\mathbf{w}}^a$ to each column of $\mathbf{W}^a$. Therefore, denoting with $\mathbf{w}^{a(i)}$ the $i$-th column of the resulting matrix, the analysis ensemble in model space is given by

$$\mathbf{x}^{a(i)} = \bar{\mathbf{x}}^b + \mathbf{X}^b \mathbf{w}^{a(i)} \tag{3.45}$$

The vector $\mathbf{w}^{a(i)}$ can be regarded as the vector of weights which defines the linear combination of the background ensemble perturbations to add to the background mean to obtain the analysis for the $i$-th member of the ensemble in model space.

**Four-dimensional formulation of the LETKF**

The analysis step can be performed whenever a new set of observations is available. This can be a reasonable approach when observations are made at regular times and not too frequently, but it does not apply in meteorological applications, since observations can be very irregular in time (e.g. measurements from aircraft) and very frequent (e.g. radar or satellite). To overcome this issue, Hunt et al. (2007) extended the LETKF to a four-dimensional version named 4D-LETKF which allows to assimilate observations collected at different times.

As seen before, in the LETKF scheme the analysis is obtained as a linear combination of background ensemble states at analysis time and these model states are compared to observations collected at the same time. In the 4D formulation of LETKF, the analysis is generated by a linear combination of the background ensemble trajectories over a time interval and these trajectories are compared to observations taken over the same time interval. A sketch of this concept is shown in Figure 3.2. To be more concrete, assume that observations $\mathbf{y}^o_{\tau_j}$ are collected at times $\tau_j$ since the last analysis and that their observation error covariances are $\mathbf{R}_{\tau_j}$. At each time $\tau_j$ the observation operator $\mathcal{H}_{\tau_j}$ is applied to the background ensemble, obtaining the mean $\bar{\mathbf{y}}^b_{\tau_j}$ and the differences from the mean $\mathbf{Y}^b_{\tau_j}$. Then, the components of $\mathbf{y}^o_{\tau_j}$, $\bar{\mathbf{y}}^b_{\tau_j}$ and $\mathbf{Y}^b_{\tau_j}$ for each time step $\tau_j$ are simply concatenated to obtain the observations $\mathbf{y}^o$, the background mean $\bar{\mathbf{y}}^b$ and the differences from the mean $\mathbf{Y}^b$. Similarly, the corresponding observation error covariance $\mathbf{R}$ is formed as a block diagonal matrix with blocks $\mathbf{R}_{\tau_j}$. Given this notation, Eqs. (3.39) - (3.45) can be employed to derive the analysis.

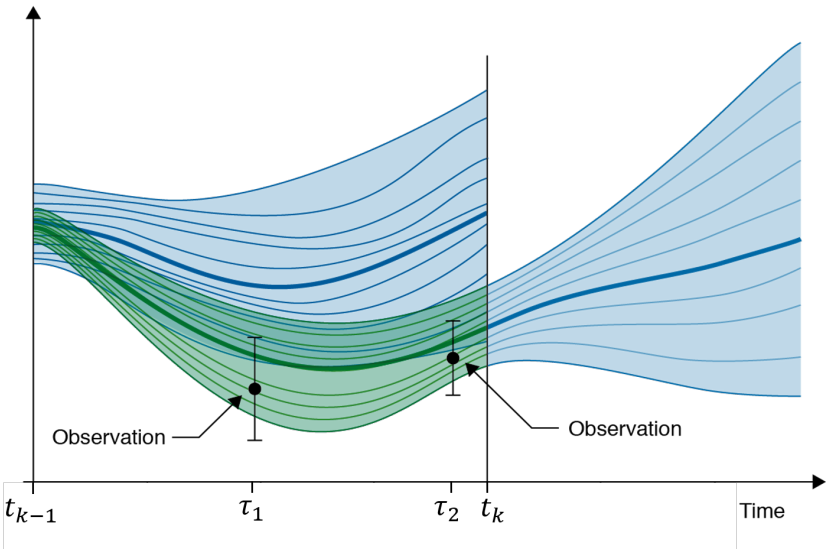


**Figure 3.2.** Schematic representation of a 4D formulation for an EnKF scheme. Thin blue lines are background ensemble trajectories and the thick blue line is the background ensemble mean. The EnKF scheme, using observations (depicted as black dots with an error bar), determines the linear combination of background trajectories which defines the analysis ensemble (thin green lines) and its mean (thick green line).

## 3.3 The KENDA system

The kilometre-scale ensemble data assimilation (KENDA) system (Schraff et al., 2016) implements for the COSMO model the LETKF scheme in its four dimensional formulation, as described in Section 3.2.4. During the COSMO model forward integration, observation operators are applied whenever observations are available in order to compute the model equivalent for each observation between two analysis times. Some relevant features are implemented with the KENDA system which are summarized in the following.

### Deterministic run

The analysis ensemble mean can be employed as initial condition for a deterministic forecast. However, this would lead to some inaccuracies because, if the distribution of ensemble members is non-Gaussian, the ensemble mean is generally not in balance (Schraff et al., 2016). Moreover, some variables with high variability in the small scales (e.g. cloud variables) often have smoothed fields in the ensemble

mean. To overcome these issues, a deterministic analysis is derived in KENDA by applying the Kalman gain matrix for the ensemble mean to the innovations of the deterministic run itself. In other words, in each assimilation cycle the deterministic analysis in ensemble space $\mathbf{w}^{a(det)}$ is obtained as:

$$\mathbf{w}^{a(det)} = \widetilde{\mathbf{P}}^{a}(\mathbf{Y}^{b})^{T}\mathbf{R}^{-1}\left(\mathbf{y}^{o} - \mathbf{y}^{b(det)}\right) \tag{3.46}$$

where $\mathbf{y}^{b(det)} = \mathcal{H}(\mathbf{x}^{b(det)})$ and $\mathbf{x}^{b(det)}$ is the background state for the deterministic run. Consequently, the analysis in model space is given by

$$\mathbf{x}^{a(det)} = \mathbf{x}^{b(det)} + \mathbf{X}^{b}\mathbf{w}^{a(det)} \tag{3.47}$$

### Observation weighting

Observation localization is a key factor of the LETKF scheme, as described in Section 3.2.4. The Gaspari-Cohn function is employed in KENDA to select relevant observations for each analysis grid point and to weight their impact on determining the analysis according to their distance from the grid point (see Section 3.2.3). An horizontal and a vertical length scale ($l$ in Eq. 3.31) can be specified for each observation type. In the present work, for conventional observations, i.e. AIREP, SYNOP and TEMP, the horizontal length scale is set equal to 80 km while the vertical one increases with height linearly in terms of the logarithmic of pressure from 0.075 to 0.5. Regarding radar reflectivity observations, the horizontal length scale is set to 16 km since they are much denser than conventional observations, while the vertical length scale is fix to 0.3. Some tests on the sensitivity of analysis quality on these length scale values have been performed but the results are not provided here since they are not relevant. However, the same values have been employed by Bick et al. (2016).

### Covariance inflation

In order to account for underestimation of the background error covariance, as discussed in Section 3.2.3, several techniques of covariance inflation are implemented in the KENDA system. Among them, two methods are employed in this work and in the operational set-up adopted at ARPAE.

One is the multiplicative inflation (Anderson and Anderson, 1999) which consists in inflating the analysis error covariance by a factor $\rho$ greater than 1. In KENDA, this is achieved in ensemble space by multiplying the analysis perturbation matrix $\mathbf{W}^a$, defined in Eq. (3.44), by $\sqrt{\rho}$, which is determined adaptively following Houtekamer et al. (2005). This operation is performed at each grid point separately, meaning that the value of $\rho$ varies both in space and in time.

The other technique to increase the ensemble spread is the relaxation to prior perturbation (RTPP; Zhang et al., 2004). In RTTP the analysis ensemble perturbations $\mathbf{x}^{a(i)} - \bar{\mathbf{x}}^a$ are relaxed towards the background ensemble perturbations $\mathbf{x}^{b(i)} - \bar{\mathbf{x}}^b$. In the KENDA framework, this is achieved by replacing, at each analysis grid point, $\mathbf{W}^a$ with

$$(1 - \alpha)\mathbf{W}^a + \alpha\mathbf{I} \tag{3.48}$$

where $\alpha = 0.75$ (see also Harnisch and Keil, 2015).

#### Coarse analysis grid

The KENDA suite allows to compute the analysis weights, i.e. the analysis on ensemble space, on a coarsened grid (Yang et al., 2009). After being computed on the coarsened grid, weights are interpolated to the original high-resolution grid and then used to compute analysis increments in model space. In this way, the computational cost is decreased without significantly affecting the accuracy of analysis since the spatial variability of the weights is relatively small (Yang et al., 2009). Furthermore, the use of a coarse analysis grid may be more robust against imbalances which could lead to unwanted gravity waves. In the present study, a coarsening factor equal to 3 is employed.

## 3.4 Operational data assimilation for COSMO-2I

The KENDA system is implemented operationally at ARPAE using an ensemble of 20 members plus a deterministic run. Each of the 21 members of the ensemble adopts the COSMO-2I model configuration described in Chapter 2. The ensemble

members use lateral boundary conditions provided every 3 hours at a 7 km horizontal resolution by the ensemble of the data assimilation system of the Centro Operativo per la Meteorologia (COMet), based on a LETKF scheme (Bonavita et al., 2010). The deterministic run employs hourly boundary conditions provided by COSMO-5M, a 5 km version of COSMO run at ARPAE which domain covers a large part of the Mediterranean basin and surrounding countries.

At present, only conventional observations (SYNOP, AIREP and TEMP) are assimilated in the operational set-up, through cycles of 3 hours. Moreover, latent heat nudging (LHN), an empiric assimilation scheme which allows to assimilate precipitation rates by modifying temperature and humidity profiles (see Section 4.3.1), is performed during each forecast step of the assimilation procedure. The analyses obtained for the deterministic member of the ensemble are used as initial conditions for a 48 hours COSMO-2I forecast, initialized twice a day at 00:00 and 12:00 UTC. Analyses from the other members of the KENDA ensemble are employed to initialize COSMO-2I EPS, an ensemble consisting of 20 COSMO-2I members which is run every day at 00:00 UTC for a 48 hours forecast range.

# Chapter 4

# Radar measurement, simulation and assimilation

Radar (RAdio Detection And Ranging) is an electronic system which transmits electromagnetic waves and, by receiving back an echo from a target, it allows to determine some features about the target. Since the Second World War, it has been employed by the military and by civilians for a variety of purposes, like for detecting aircraft and ships, for measuring the velocity of vehicles and for altimeter and geological observations. Furthermore, weather radars are used to measure precipitation and wind velocity and, for this reason, they have become an essential instrument to observe the atmosphere.

In this chapter, a brief description of weather radars is provided in Section 4.1, mainly following Rinehart (1990), Raghavan (2003) and Zeng (2013). Then, in Section 4.2, it is described how radar measurements are simulated by the radar operator developed for the COSMO model. In Section 4.3, the assimilation of radar observations and of derived measurements is illustrated. Finally, a description of the Italian radar network, which is exploited for this study, is provided in Section 4.4.

## 4.1 Weather radar measurements

Most part of weather radars are monostatic pulse radars. A monostatic radar is one in which the transmitter and the receiver are at the same site and usually share a common antenna. The term pulse refers to the fact that the radar transmits a short pulse of electromagnetic radiation at specific time intervals. During the time between two transmitted pulses, the radar receives possible echoes from targets. These echoes arise when a part of radiation emitted is reflected back by a target, which can be rain or cloud droplets, snow flacks, hail but also non-meteorological elements like birds, insects and dust. From the time of travel of the radiation and the direction from which it is received, the position of the object is found. Furthermore, some characteristics of the target can be determined by analysing a few features of the received radiation.

Each pulse of radiation has a duration $\tau$ which is generally between tens of nanoseconds to tens of microseconds and corresponds to a pulse width $h$ being the distance travelled during one pulse duration. Approximating the velocity of an electromagnetic wave in the air to be the same as in vacuum, called $c$, the pulse width is given by $h = c\tau$. To describe how the emitted pulse radiation "illuminates" volumes of atmosphere, it is convenient to define two coordinate systems. One is the "radar system" in which the position of a generic point is defined by $(r, \alpha, \epsilon)$, where $r$ is the radial range from the antenna, $\alpha$ is the azimuth of the antenna and $\epsilon$ its elevation. The other is the "beam system" $(r, \phi, \theta)$, where $\phi$ and $\theta$ are horizontal and vertical angles relative to the ray in the beam center, respectively. An illustration of these two coordinate systems is provided in Figure 4.1.

According to the above definitions, a radar resolution volume centered at $\mathbf{r}_0 = (r_0, \alpha_0, \epsilon_0)$ is illuminated by a pulse with the following illumination function expressed in the beam system:

$$I(\mathbf{r}) = C_r \frac{f^2(\phi, \theta)}{r^2} [W(r_0 - r)]^2 \tag{4.1}$$

where $I$ is the local power density within the volume and $r$ is the radial distance from antenna of an arbitrary position $\mathbf{r} = (r, \phi, \theta)$ within the pulse volume. The

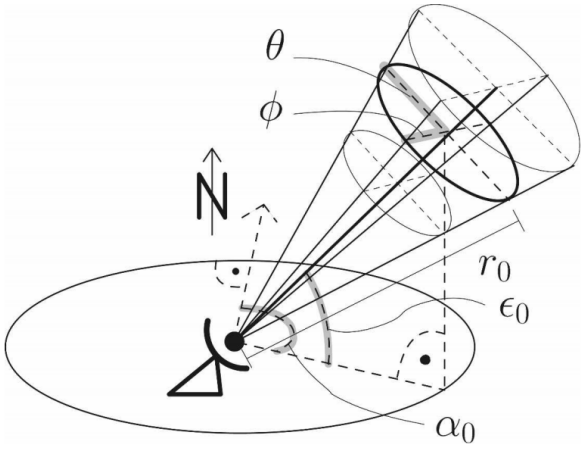


**Figure 4.1.** Sketch of a pulse volume from a single radar beam represented by thin ellipses. Its center $\mathbf{r}_0$ is at the intersection of dashed lines inside the thick ellipse. The coordinates of the center in radar system $(r_0, \alpha_0, \epsilon_0)$ are shown, as well as the coordinate directions $\theta$ and $\phi$ relative to the beam system at the center of a pulse volume (taken from Blahak, 2008).

parameter $C_r$ is the so-called radar constant and depends on specifics of the radar system including power transmitted, antenna gain and radar wavelength. The function $W$ is the range weighting function which can be assumed to be a step function, that is:

$$\begin{cases} 1 & \text{if } r \in [r_0 - \Delta r/2,\ r_0 + \Delta r/2] \\ 0 & \text{otherwise} \end{cases} \tag{4.2}$$

where $\Delta r$ is the range resolution of the radar which primarily depends on the pulse width. Finally, $f^2(\phi, \theta)$ is the beam weighting function which describes the amount of power transmitted by the radar antenna in a given direction $(\phi, \theta)$.

Regarding the beam weighting function, an antenna would be expected to direct all of the radar energy into a single direction. However, this is impossible in practical cases and, therefore, a real radar antenna exhibits a large lobe (main lobe or main beam) corresponding to the greatest field strength and, at the same time, it transmits (and receives) energy off to the side of the main lobe in what are called side lobes. Side lobes are present in all directions away from the main lobe and have different forms in each direction. When they are in directions nearly opposite to the main lobe, they are named back lobes. A sketch of this configuration, also called antenna pattern, is shown in Figure 4.2. The angular width of the main

lobe, defined as the angle between the two directions where the power density is one-half (or 3 dB) less than its maximum value, is referred to as beamwidth. It varies directly with wavelength and inversely with antenna size.

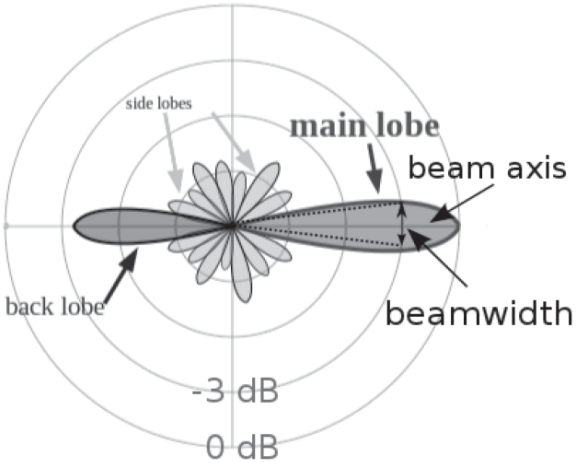


**Figure 4.2.** Antenna radiation pattern: the radial distance from the center represents signal strength (taken from Zeng, 2013).

Operational weather radars generally works in the so called volume scanning mode, meaning that the antenna moves in the azimuthal direction at a fixed elevation angle and, when a full rotation is completed, it tilts up to the next elevation and does the same sweep again. This procedure is repeated until it has scanned at all elevations. For each azimuthal and elevation angle, many consecutive pulses are transmitted to achieve statistical signal stability of the measure and, then, values for each radar resolution volume are averaged.

Most ground-based weather radars employs microwaves, in particular at wavelengths between 3 and 10 cm. At longer wavelengths the echo power is much lower and a larger antenna is necessary to get a specified beamwidth, increasing costs. At shorter wavelengths, attenuation of radiation increases (see Section 4.1.2), making quantitative measurements difficult. In Table 4.1 a list of frequencies of interest for various meteorological radar applications is provided.

The large majority of currently operational radar systems have "Doppler capabilities", that is they measure the frequency shift between transmitted and backscattered power, allowing an estimate of target velocity along the radial beam.

**Table 4.1.** Radar band designation according to frequency and corresponding main applications in meteorology.

| Band | Frequency | Wavelength | Main applications |
|---|---|---|---|
| L | 1-2 GHz | 30-15 cm | Clear air and precipitation phenomena |
| S | 2-4 GHz | 15-8 cm | Precipitation measurement |
| C | 4-8 GHz | 8-4 cm | Precipitation measurement |
| X | 8-12 GHz | 4-2.5 cm | Thunderstorm and gust front detection |
| $K_u$ | 12-18 GHz | 2.5-1.7 cm | Tornado observation |

However, in the following, only the reflectivity product of the radar will be considered, since radial velocities, i.e. radial winds, are not employed in this study.

### 4.1.1 Reflectivity

When a target is illuminated by the radar, the incident radiation is in part absorbed and in part scattered in all directions. The radiation backscattered in the direction of the radar is measured by the receiver, which detects and amplifies the signals received by the antenna. The fraction of energy backscattered by the target depends on its backscattering cross section $\sigma_b$. For spherical targets, Mie (1908) derived a complete scattering and absorption theory in terms of an infinite series of electric and magnetic multipoles. In particular, the backscattering cross-section can be expressed as

$$\sigma_b = \frac{\lambda^2}{4\pi}\left|\sum_{n=1}^{\infty}(-1)^n(2n+1)(a_n+b_n)\right|^2 \tag{4.3}$$

where $\lambda$ is the wavelength and $a_n$ and $b_n$ are the Bessel functions, which represent the magnetic and electric multipoles of order $n$ induced by the incident radiation. These are functions of the third and higher powers of $\pi D/\lambda$, being $D$ the diameter of the spherical target.

For spherical targets which are much smaller than the wavelength, i.e $D/\lambda < 0.1$, Eq (4.3) can be approximated by

$$\sigma_b = \frac{\pi^5|K|^2D^6}{\lambda^4} \tag{4.4}$$

where $K$ is the dielectric factor of the particle and it is related to its complex refractive index. This is the so-called Rayleigh scattering theory which can be a good approximation in several cases. For example, it holds for raindrops when using a C-band radar, since raindrop diameters are usually smaller than 6 mm. However, it does not usually hold for hailstones or snowflakes. Moreover, it is important to note that the spherical assumption for hydrometeors is good only for small raindrops and hailstones. Both large raindrops and most of solid precipitation particles can be far from spheric and, in that case, both Rayleigh and Mie scattering theories are no longer valid.

In an illuminated radar resolution volume, there are usually much more than one single target. Accordingly, assuming that the scattering is incoherent, the total backscattering cross section per unit volume, referred to as radar reflectivity $\eta$, can be defined as the sum of the individual cross sections:

$$\eta = \sum_{k \in S} \sum_{j \in N_k} \sigma_{b_{kj}} \tag{4.5}$$

where $S$ contains all hydrometeor types in the volume and $N_k$ is the number of hydrometeors of type $k$. It can be also expressed in continuous form via

$$\eta = \sum_{k \in S} \int_0^\infty \sigma_{b_k}(D) \mathcal{N}_k(D) \mathrm{d}D \tag{4.6}$$

where $\mathcal{N}_k$ is the particle size distribution of hydrometeor type $k$.

Under Rayleigh scattering approximation, radar reflectivity is given by:

$$\eta = \sum_{k \in S} \frac{\pi^5 |K_i|^2}{\lambda^4} \underbrace{\int_0^\infty \mathcal{N}_k(D) D^6 \mathrm{d}D}_{:= z_k} = \sum_{k \in S} \frac{\pi^5 |K_i|^2}{\lambda^4} z_k \tag{4.7}$$

where $z_k$ is the radar reflectivity factor for the hydrometeor type $k$; this quantity is generally indicated with $Z_k$, but here the capital letter is reserved for values in logarithmic units (see below) as done in Zeng (2013). Unlike $\eta$, the reflectivity factor is exclusively a property of the volume target, since it depends only on the number of scattering elements and their sizes.

As mentioned before, Rayleigh approximation does not hold in general, espe-

cially for weather radars employing a short wavelength. Moreover, the composition of hydrometeors inside a scanned volume is generally not known. Therefore, it is convenient to define the reflectivity factor as if the illuminated radar resolution volume only contains water drops small compared to radar wavelength. Accordingly, the (water-)equivalent reflectivity factor $z_e$ is the reflectivity factor that must have this water drop filled volume in order to produce the same radar reflectivity $\eta$ of the original volume with unknown properties. Mathematically:

$$z_e = \frac{\lambda^4}{\pi^5 |K_w|^2} \eta \tag{4.8}$$

where $|K_w|^2$ is the dielectric factor for water.

The quantity $z_e$ has conventional units of $[\mathrm{mm}^6/\mathrm{m}^3]$ and it can span several orders of magnitude. Therefore, it is generally expressed in logarithmic units via

$$Z_e = 10 \log_{10} \left( \frac{z_e}{1\,\mathrm{mm}^6/\mathrm{m}^3} \right) \tag{4.9}$$

Variable $Z_e$ is generally called simply reflectivity and it is measured in units of dBZ.

### 4.1.2 Attenuation

The electromagnetic radiation transmitted by the radar and backscattered by targets in the illuminated volume is attenuated due to absorption and scattering by atmospheric gases and by other targets which may be present between the radar and the scanned volume. The amount by which the signal is reduced depends on the amount of each interacting substance and on the wavelength of the radiation. In general, attenuation is stronger as the wavelength decreases. For most operational weather radars, the attenuation due to atmospheric gases is small and can be corrected for. Attenuation by aerosols or dust is negligible. The attenuation by liquid or solid precipitation is much stronger, especially for radar in X-band and at even smaller wavelengths.

When attenuation is taken into account, the equivalent reflectivity factor $z_e$

under Rayleigh scattering approximation (Eq. 4.8) becomes

$$z_e = \frac{\lambda^4}{\pi^5 |K_w|^2} \frac{\eta}{\ell(r)^2} \tag{4.10}$$

where $\ell(r)$ is the one-way loss factor due to attenuation along the radar beam at range $r$, which is given by

$$\ell(r) = \exp\left( \int_0^r \alpha(r') \mathrm{d}r' \right) \tag{4.11}$$

being $\alpha(r')$ the attenuation factor defined as

$$\alpha(r') = \sum_{k \in S} \int_0^\infty \sigma_{att,k}(D) \mathcal{N}_k(D, r') \mathrm{d}D \tag{4.12}$$

In the attenuation factor definition, $\sigma_{att,k}$ is the attenuation (or extinction) cross section for hydrometeor type $k$ and $\mathcal{N}_k(D, r')$ is the corresponding particle size distribution at range $r'$. Note that squaring $\ell(r)$ in Eq. (4.10) accounts for two-way attenuation, that is for both transmitted and received signals.

### 4.1.3 Radar equation

The radar equation relates the received power to the characteristics of the target located at $\mathbf{r}_0 = (r_0, \alpha_0, \epsilon_0)$, as a function of radar specifics and of conditions on the propagation path. Assuming that the particles fill homogeneously the scanned volume, that the main lobe of the antenna pattern is Gaussian and that the range weighting function $W$ is described by Eq. (4.2), the radar equation can be written as (Zeng, 2013)

$$P_r(\mathbf{r}_0) = C_r \frac{\pi^5 |K_w|^2}{\lambda^4} \int_{r_0 - \frac{\Delta r}{2}}^{r_0 + \frac{\Delta r}{2}} \int_{-\pi}^{\pi} \int_{-\frac{\pi}{2}}^{\frac{\pi}{2}} z_e(r, \phi, \theta) \ell^{-2}(r, \phi, \theta) \frac{f^4(\theta, \phi)}{r^2} \cos\theta \, \mathrm{d}\theta \, \mathrm{d}\phi \, \mathrm{d}r \tag{4.13}$$

where $P_r$ is the received power. By inverting the radar equation, the equivalent reflectivity factor of the scanned volume can be derived.

Actually, the equivalent reflectivity factor derived by the radar processor is a volumetric quantity and is an average over numerous consecutive pulses to ensure

a statistically stable measurement. Denoting it with $\overline{z_e^r}$ (where "r" stands for received and the bar represents the sample mean value) and letting $z_e$ be the "true" equivalent radar reflectivity factor, we can express $\overline{z_e^r}$ in the radar system as (Zeng et al., 2016):

$$\overline{z_e^r}(\mathbf{r}_0) = C_r \frac{\int_{r_0-\frac{\Delta r}{2}}^{r_0+\frac{\Delta r}{2}} \int_{\alpha_0-\pi}^{\alpha_0+\pi} \int_{\epsilon_0-\frac{\pi}{2}}^{\epsilon_0+\frac{\pi}{2}} \frac{z_e(r,\alpha,\epsilon)}{\ell^2(r,\alpha,\epsilon)} \cdot \frac{f_e^4(\alpha,\epsilon)}{r^2} \cos\epsilon \, \mathrm{d}\epsilon \, \mathrm{d}\alpha \, \mathrm{d}r}{\int_{r_0-\frac{\Delta r}{2}}^{r_0+\frac{\Delta r}{2}} \int_{\alpha_0-\pi}^{\alpha_0+\pi} \int_{\epsilon_0-\frac{\pi}{2}}^{\epsilon_0+\frac{\pi}{2}} \frac{f_e^4(\alpha,\epsilon)}{r^2} \cos\epsilon \, \mathrm{d}\epsilon \, \mathrm{d}\alpha \, \mathrm{d}r} \tag{4.14}$$

Note that here the effective beam weighting function $f_e$ replaces $f$ to take into account a "broadening" into beam weighting function due to antenna rotation during averaging (see Blahak, 2008).

### 4.1.4 Beam propagation

The path of a radar beam, as for any electromagnetic wave, is determined by the Fermat's principle which states that the path taken between two points is the one that can be traversed in the least time. Travel time depends on the propagation speed which, in turns, is a function of the real part of the refractive index of the propagation medium. For the atmosphere, refractivity depends mainly on pressure, temperature and vapour pressure which, in normal conditions, vary mainly with altitude. Since refractivity generally decreases with height, the radar beam bends towards the Earth's surface. Following Battan (1973), the radius of curvature of radar beam $R_b$ due to both Earth curvature and atmospheric refraction is given by

$$\frac{1}{R_b} = \frac{1}{R_e} + \frac{\delta \, \mathrm{Re}(n)}{\delta H} \tag{4.15}$$

where $R_e = 6374$ km is the Earth's radius and $\delta \, \mathrm{Re}(n)/\delta H$ is the gradient of the real part of the refractive index with height. In standard conditions, this gradient

is approximately equal to $-39 \cdot 10^{-6}$ km$^{-1}$ and therefore

$$R_b \approx 8483 \text{ km} \approx \frac{4}{3} R_e \tag{4.16}$$

This is the so-called "4/3 Earth radius model" which predicts that the radar beam propagates along a circle with diameter of 4/3 times the Earth's radius. In case the atmosphere is far from standard condition, this model is not applicable and more sophisticated methods should be employed (see for e.g. Zeng, 2013).

### 4.1.5 Sources of errors

The accuracy of radar measurements varies considerably with radar specifics, location, range and with meteorological conditions. Several sources of errors have been discussed by many authors (e.g Zawadzki, 1973; Wilson and Brandes, 1979; Michelson et al., 2005) and they can be summarized as follows:

- non-meteorological echoes (clutter);
- side lobe echoes;
- multiple scattering;
- second trip echo which occurs when an echo is received after the subsequent pulse is transmitted, resulting in misplacement of the target;
- beam shielding by obstacles (e.g. mountains);
- deviation of atmospheric conditions from assumption of 4/3 Earth radius model;
- non-uniform beam filling;
- strong attenuation in presence of heavy rainfall, hail or melting hydrometeors;
- instrumental noise and miscalibration.

In order to eliminate or al least reduce part of these errors, a quality control procedure is employed to reject or to correct observations. A detailed description of the most used techniques which are employed in operational cases can be found for e.g. in Szturc et al. (2012).

## 4.2 Radar operator

In order to assimilate reflectivity measurements, a radar operator is necessary to compute the model equivalent observations. In this regards, the efficient modular volume scanning radar operator (EMVORADO; Zeng, 2013, Zeng et al., 2016) has been developed for the COSMO model.

The EMVORADO operator simulates model equivalent reflectivities separately for each radar through a two steps process. In the first step, the equivalent radar reflectivity factor $z_e$ and the attenuation factor $\alpha$ are computed from the microphysical quantities at the model grid points. In the second step, values of $z_e$ and $\alpha$ are interpolated to the radar rays and then the process of radar sampling to arrive at $\overline{z_e^r}$ is simulated. For the sake of computational efficiency, it is assumed that the beam broadening effect is negligible and, therefore, the pulse volume averaging can be switched off. Accordingly, the reflectivity is evaluated at the centre of each beam and Eq. (4.14) can be simplified as follows

$$\overline{z_e^r}(\mathbf{r}_0) = \frac{z_e(r_0)}{\ell^2(r_0)} \tag{4.17}$$

The computation of $z_e$ is based on all hydrometeor types. In case the COSMO model runs with a one moment microphysical scheme, as in this work (see Section 2.3), the prognostic microphysical variables are the mass densities of cloud water $q^c$, cloud ice $q^i$, rain $q^r$, snow $q^s$ and graupel $q^g$.

The user can choose between the Rayleigh and the Mie scattering theories. The latter provides more accurate results than the former but it is more expensive from a computational point of view because an analytical solution does not exist. However, a look-up table which relates $z_e$ and $\alpha$ to prognostic model variable can be created for each microphysical species. This results in a considerable improvement of computational efficiency which make the computational cost of using Mie scattering comparable to that of Rayleigh scattering. Moreover, with the Rayleigh scattering it is not possible to compute $\alpha$ since there is no a consistent approximation for precipitation-sized particles at typical radar wavelengths.

All hydrometeors are supposed to be spherical. In case the Mie scattering is employed, the refractive index of the particles is temperature dependent, otherwise

a simpler formulation based on Oguchi (1983) is used. For Mie scattering, cloud water and rain drops are assumed to be composed only by water, while all solid hydrometeors are supposed to be a mixture of ice and air or a mixture of ice, air and water to take into account the presence of partially melted particles. The technique employed to deal with these mixtures is the effective medium approximation (EMA), meaning that the mixture is considered as an homogeneous medium with an effective refractivity index, which reproduces approximately some scattering proprieties of the real particle. Normally, for large particles (except rain) the Mie scattering scheme results in lower reflectivities than the Rayleigh approximation, but for melting particles, the Mie solution usually produces higher reflectivities. Regarding the drop size distributions, they are chosen in a model-consistent way, that is as close as possible as those indicated in Section 2.3.

The EMVORADO operator runs efficiently on parallel-computers and its modularity makes possible to choose between different configurations. In the present study, the impact on data assimilation of the scattering theory and of attenuation are evaluated. Finally, even if the operator provides several options to model the beam bending (see Zeng, 2013), here the 4/3 Earth radius approximation is employed in all experiments since some preliminary tests did not reveal a significant sensitivity to this parameter.

## 4.3 Assimilation of radar data

The radar data are highly dense in space (both horizontally and vertically) and in time and this allows to collect a lot of information on the state of the atmosphere. For this reason, in addition to being fundamental for the real-time weather observation, they can be assimilated to improve the quality of the analyses of a NWP model. Regarding reflectivity, two main approaches can be followed: an empirical one and a statistically-based one. The former involves the conversion of reflectivity volumes in surface precipitation rate employing an (empirical) method (see Sauvageot (1994) for a review); then, model humidity and/or temperature profiles are empirically modified to reproduce the same precipitation rate as the observed one. The latter requires to compute the model equivalent reflectivity by applying a radar operator to model fields and, then, to directly assimilate reflectivity volumes

using a statistically-based assimilation scheme, like those which rely on variational methods or on the Kalman Filter. The "empirical" approach is much simpler and less computationally expensive than the "statistically-based" one, since it does not require a radar operator. As a consequence, methods based on this technique, like the latent heat nudging (LHN; Jones and Macpherson, 1997) described in Section 4.3.1 or the humidity nudging (Davolio and Buzzi, 2004; Sokol, 2009; Davolio et al., 2017), have been widely employed in operational NWP. On the contrary, the direct assimilation of reflectivity volumes is still a pioneering method in operational data assimilation systems.

### 4.3.1 Latent heat nudging

Each precipitating hydrometeor is the result of several physical processes which are associated to a release of latent heat. Overall, the precipitation rate $R$ can be assumed to be proportional to a certain amount of latent heat release $\Delta L_H$ which, in turns, is associated to an increase in temperature $\Delta T$. In the hypothesis that we can identify a point $l_0$ in which a precipitation particle forms, we can denote as $l$ the path travelled by the particle from $l_0$ to the ground at $l_g$. Accordingly, the relation between rain rate and latent heat release can be expressed as

$$R(l_g) \propto \int_{l_0}^{l_g} \Delta L_H(l) \mathrm{d}l \tag{4.18}$$

The path $l$ can be very complex and it is associated to a certain travel time $\Delta t$. In this regards, the assumption of LHN is that the whole path is contained within one single model column and that it is travelled in a single model time step. Accordingly, the precipitation rate at the surface grid point is simply proportional to the vertical integral of the latent heat release in the column above the point. Therefore, precipitation can be assimilated through LHN by scaling, at each time step, the latent heat model profile according to the ratio of observed and modelled rain rates, respectively $R_{obs}$ and $R_{mod}$. This corresponds to adding to the thermodynamic equation a temperature increment $\Delta T_{LHN}(l)$ defined by

$$\Delta T_{LHN}(l) = (\alpha - 1)\frac{1}{c_p}\Delta L_H(l) \tag{4.19}$$

where $\alpha$ is given by

$$\alpha = \frac{R_{obs}}{R_{mod}} \tag{4.20}$$

and it is subjected to upper and lower bounds in order to keep the temperature increment in reasonable limits. When the temperature profile is modified, the relative humidity is preserved by altering the specific humidity. In this way, in the grid points where the model underestimates the rain rate, $\Delta T_{LHN}$ is positive and upward motion is forced, leading to an increase of precipitation. Otherwise, $\Delta T_{LHN}$ is negative and precipitation is suppressed.

A more detailed description of the implementation of LHN for the COSMO model can be found in Stephan et al. (2008). In particular, it is worth mentioning that, in the COSMO implementation, the model rain rate $R_{mod}$ is replaced by a reference rain rate $R_{ref}$ to account for the delay of the initiation of precipitation. This reference precipitation is obtained by vertically integrating the hydrometeor fluxes of rain, snow and graupel.

Even if the scheme is empirical, as well as the conversion from $Z$ to $R$, and some assumptions may be violated (Stephan et al., 2008), the LHN has been successfully employed in an operational framework for the COSMO model at DWD (Stephan et al., 2008), at Meteoswiss (Leuenberger and Rossa, 2004; Leuenberger and Rossa, 2007) and at ARPAE (Gastaldo et al., 2018) and in several other weather centres as reviewed by Gustafsson et al. (2018). Regarding the implementation for the COSMO model, LHN can be coupled with KENDA as described by Schraff et al. (2016): during the forward integration from one LETKF analysis step to the next, the LHN is applied to each ensemble member and to the deterministic run. This is the implementation adopted at ARPAE, as described in Section 3.4. The process with which the Italian Civil Protection Department (DPC) converts reflectivity volumes of the national radar composite (see Section 4.4) into surface rainfall intensity (SRI) is illustrated in Vulpiani et al. (2012) and Rinollo et al. (2013). Fields of SRI are gridded fields at a resolution of 1 km but they are interpolated to COSMO-2I horizontal resolution before being assimilated via LHN.

### 4.3.2 Direct assimilation of reflectivity volumes

The radar operator allows to compute the model equivalent observations associated to reflectivity measurements. By comparing model and observations, reflectivity volumes can be assimilated through a statistically-based assimilation scheme, like the LETKF described in Section 3.2.4. In this way, the 3-dimensional information on the state of the atmosphere provided by reflectivity data can be exploited. Moreover, compared to LHN, it avoids to introduce an empirical relationship to convert $Z$ into $R$ which may be affected by large errors. However, some aspects which are described in the following have to be taken into account.

#### Superobbing

The high spatial density of radar observations is precious in data assimilate to improve the estimation of the analysis of a NWP model but it is associated to high computational costs, mainly due to the complexity of the radar operator. In addition, it violates the assumption of non-correlated observation errors made in many data assimilation schemes.

To reduce the total amount of data and to extract essential content of information, the superobbing technique, proposed by Michelson (2003) and implemented in the EMVORADO operator, is adopted in this study. With this method, reflectivities over a defined area are combined through a weighted mean into one single observation (superobservation) representative of the desired greater spatial scale. The superobbing is implemented in a quasi-Cartesian way. A two-dimensional Cartesian grid with a resolution $\Delta L$ is defined and, for each radar elevation, the radar bin centers are projected on this plane. Then, for each Cartesian point, the closest radar point is selected to be the center of the superobservation and it remains in the radar system without being interpolated onto the Cartesian grid. Once the center of the superobservation is chosen, radar bins surrounding the center bin are averaged with an averaging area defined by $\Delta L$ and with a Gaspari-Cohn weighting function which has the maximum at the center of the superobservation. Note that the number of radar bins averaged into one superobservation decreases with range.

An example of the result of a superobbing procedure is provided in Figure 4.3.

On the left the reflectivity acquired by the radar located in Armidda (Sardinia region) at its lowest elevation is shown at its original resolution. On the right the corresponding superobbed field obtained using $\Delta L = 10$ km is depicted. As can be observed, the superobbing procedure allows to preserve the main features of the original reflectivity field but it severely reduces the number of observations. It is worth remembering that the superobbing procedure is applied to both observation and background fields. In this study, the resolution of superobbing is $\Delta L = 10$km, as in Bick et al. (2016).

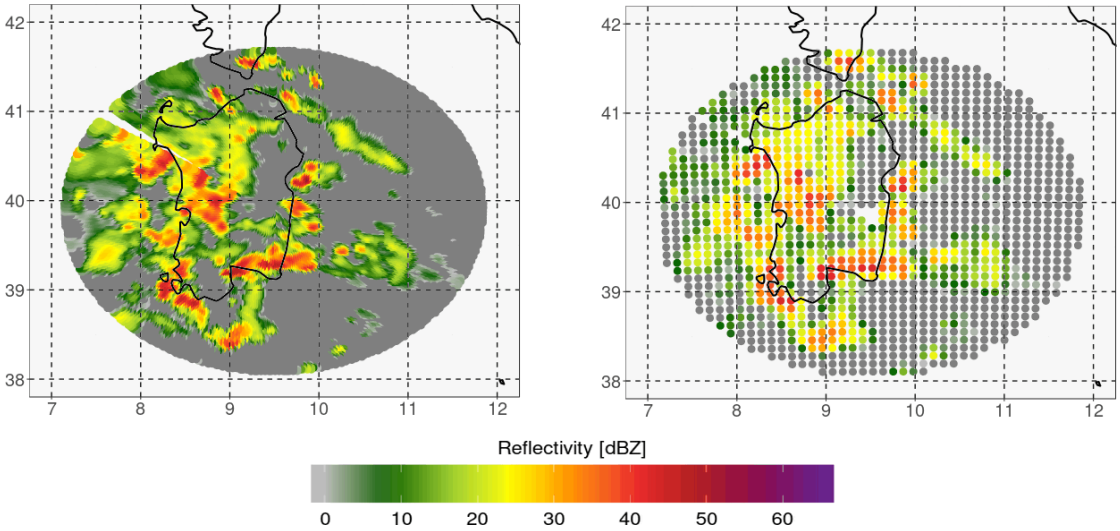


**Figure 4.3.** Original (left) and superobbed (right) reflectivity fields for the lowest elevation of the Armidda radar at 10 UTC on 10 October 2018.

### No precipitation information

Radar reflectivity values usually range from -30 dBZ to 60 dBZ. According to Marshall and Palmer (1948), a rain rate of 0.1 mm/h corresponds to approximately 10 dBZ. Therefore, the limit above which detectable precipitation starts can be considered to be around 5-10 dBZ, meaning that a large part of the reflectivity range of values is not associated to precipitation. As a consequence, in a data assimilation framework large differences between observed and simulated reflectivities may arise without being related to precipitation differences. This leads to possible large analysis increments which are unphysical. To avoid this problem, it

is common practice to set all observation and background reflectivity values below a certain threshold $Z_{thr}$ equal to $Z_{thr}$. In this work, after some preliminary tests, a $Z_{thr}$ of 5 dBZ is employed as done in Aksoy et al. (2009) and Bick et al. (2016). Even if it is recognized that it is not the correct way to proceed, the threshold is applied before superobbing since this in the only way implemented in the EMVORADO operator for computational reasons. The error introduced by applying the threshold before and not after superobbing has to be taken into account as a part of pre-processing error which is one of the sources of the observation error (see Section 3.1).

### 4.3.3 Issues on the assimilation of radar data

Due to the several sources of error associated to radar measurements, the assimilation of radar data is not straightforward. As mentioned in Section 4.1.5, the use of a quality control procedure allows to correct most part of errors or to discard uncorrectable measurements. However, there is not a unique way to deal with radar error sources and not all errors can be detected by an automatic procedure.

Regarding SRI fields employed in this study for LHN, the quality control procedure performed by DPC on raw reflectivity data before converting them on rainfall estimation is discussed in Vulpiani et al. (2012) and Rinollo et al. (2013). Note that for the estimation of precipitation at ground, in addition to the errors reported in Section 4.1.5, also the vertical variability of reflectivity may introduce some errors. For example, the presence of a bright band or the use of radar measurements at high altitude may lead to a rainfall estimation which is not representative for ground level.

For the direct assimilation of reflectivity volumes, the main sources of error can be summarized as follows: clutter, beam blocking, attenuation and distance from the radar. In this study, it is supposed that the quality control procedure, applied to reflectivity measurements before being provided to us, is able to deal with the former three error sources as well as possible. It is interesting to notice that the application of the 5 dBZ threshold on reflectivity values ensures to account, in non-precipitating conditions, for clutter affected measurements not detected by the quality control procedure. In fact, due to this threshold, if the background

equivalent of all members of the ensemble is equal to 5 dBZ, no observation is assimilated. In other words, if a high spurious reflectivity (due to clutter) is measured but precipitation is not forecast by any member of the ensemble, this measure will not be assimilated.

Regarding the distance from radar, this is a source of errors which can be handled in different ways. Far from the radar station, accuracy of measurement decreases due to beam broadening. The observed atmospheric volumes result to be very large and some assumptions, like single scattering or the uniform filling of the volume, are likely to be violated. Accordingly, it is sometime decided to restrict the maximum range distance of measure, generally to 120 km. In this study, however, the whole available volume is assimilated for each radar. This is done for two reasons. First of all, this choice is consistent with what done by DPC to generate SRI fields, ensuring that, for the same radar, SRI data and reflectivity volumes have the same areal coverage. Furthermore, even if a measure far from the radar may be not very accurate, it provides some information on the state of the atmosphere which is useful to be assimilated. The uncertainty on these measures, as well as for any other one, is accounted by correctly specifying the observation error.

## 4.4 Radars employed in this study

The radar stations employed in this study are listed in Table 4.2 and their approximate area coverage is shown in Figure 4.4. All stations are used by DPC to generate the radar-derived surface rainfall intensity composite which is employed in this study for LHN. The quality control procedure which raw radar reflectivity volumes undergoes to eliminate or reduce the errors described in Section 4.1.5 and the method with which they are combined and converted into SRI composite is described in Vulpiani et al. (2012) and Rinollo et al. (2013). On the other hand, only solid line radars in Figure 4.4 were available (at least for one of the case studies discussed in this work) for direct assimilation of reflectivity volumes.

The radar network considered here is rather inhomogeneous due to the complex orography of Italy and to some historical reasons. First of all, radars belong to different institutions. Most of them are owned by DPC but some belong to regional

**Table 4.2.** List of radar stations employed in this study. Each one is used by DPC to generate the SRI composite employed for LHN, but only a part of them were available for reflectivity data assimilation. For the latter, it is indicated if they were available only for the 2018 case studies (*sept2018*, *oct2018* and *nov2018* described in Section 6.2.2) or for all case studies (both 2018 cases and *sept2017* described in Section 5.1) performed in this study.

| Name | Latitude | Longitude | Altitude [m] | Refl. available |
|---|---|---|---|---|
| Zoufplan | 46.56 | 12.97 | 1999 | 2018 cases |
| Macaion | 46.49 | 11.21 | 1866 | No |
| Milano Linate | 45.34 | 9.29 | 108 | No |
| Bric della Croce | 45.03 | 7.73 | 710 | All cases |
| Gattatico | 44.79 | 10.50 | 35 | All cases |
| S. Pietro Capofiume | 44.65 | 11.62 | 11 | All cases |
| Settepani | 44.25 | 8.20 | 1384 | All cases |
| Crocione | 43.96 | 10.61 | 1026 | 2018 cases |
| Serano | 42.87 | 12.80 | 1428 | 2018 cases |
| Monte Mida | 42.05 | 13.18 | 1710 | No |
| Il monte | 41.94 | 14.62 | 692 | 2018 cases |
| Capodichino | 40.88 | 14.27 | 90 | No |
| Capo Caccia | 40.57 | 8.17 | 220 | No |
| Armidda | 39.82 | 9.49 | 1261 | 2018 cases |
| Pettinascura | 39.37 | 16.62 | 1708 | 2018 cases |
| Lauro | 37.11 | 14.84 | 980 | 2018 cases |

authorities or to the Italian company for navigation services (ENAV) or to Italian Air Force. While for deriving surface precipitation the quality control on raw reflectivity is performed by DPC, the reflectivity volumes for direct assimilation experiments were provided to us after undergoing the quality control procedure of the institution to which they belong. Therefore, since radars assimilated directly are owned by 3 different institutions (Gattatico and S. Pietro Capofiume belongs to ARPAE, Bric della Croce and Settepani to ARPA Piemonte and ARPAL and the others to DPC), they are respectively subjected to 3 different quality control procedures.

In addition to the quality control inhomogeneity, some acquisition strategies are different. Since radars are placed at very different altitudes, the beam elevations employed by each instrument vary significantly. Moreover, regarding time resolution of data, observations are acquired every 10 minutes for all stations with

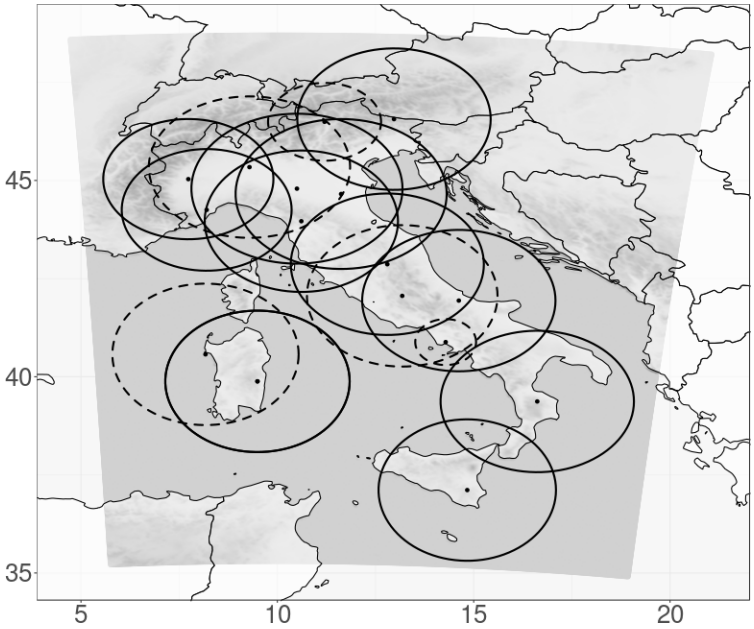


**Figure 4.4.** Italian radar network overlapped to the integration domain of COSMO-2I (grey-scale). For each radar the approximate coverage area is shown with a dashed line if the radar system contributes only to generate the SRI composite employed in LHN and with a solid line if it is used (at least in one of the case studies described in this work) also to directly assimilate reflectivity volumes through KENDA.

the exception of the two radars owned by ARPAE: San Pietro Capofiume radar acquires each 15 minutes while Gattatico radar acquires every 15 minutes starting from minutes 5 and 10 of each hour. Finally, for the purpose of direct reflectivity assimilation, all volumes are provided to us in spherical coordinates with a range resolution of 1 km, but the azimuthal resolution is 1° for radars owned by DPC, ARPA Piemonte and ARPAL while 0.9° for both radars of ARPAE Emilia-Romagna.

# Chapter 5

# The impact of the length of the assimilation window

One of the critical aspects of EnKF methods, which becomes even more crucial when dealing with reflectivity volumes, is the length of the assimilation window, that is the time interval in which observations are collected to be assimilated. Generally, it coincides with the length of the forecast step of the assimilation cycle (for brevity, also referred to as the length of the assimilation cycle or the cycle length), meaning that all observations collected during the forward integration of the model are assimilated. Focusing only on EnKF methods, a short window would be desirable to avoid that dynamical features leave the area where computed localized increments are significant (Buehner et al., 2010a) and to better preserve the Gaussianity of the ensemble which can be compromised by nonlinearities (Ferting et al., 2007). On the other hand, a too short window would lead to an increase of imbalances in the analysis, since the model has no the time to filter spurious gravity waves, introduced at each initialization, through the forecast step of the assimilation cycle.

When reflectivity volumes are assimilated, the window length becomes an even more relevant issue. In fact, to exploit the high temporal frequency of radar data, which is essential to properly characterize fast developing and moving precipitation systems, it seems reasonable to employ short windows to assimilate, in each cycle, only observations collected very close to the analysis time. Furthermore, the choice

of a short window is encouraged by the use of short localization scales, which have to be employed since small scales features are observed (Houtekamer and Zhang, 2016). Conversely, the big amount of radar observations enhances the imbalance issue and, therefore, the imbalances generated in the model by each initialisation should be checked and kept under control.

An alternative way to assimilate only the most relevant observations is to select in each cycle a subset of data including the closest to the analysis time. In other words, it consists in employing an assimilation window which is shorter than the length of the assimilation cycle. This allows to assimilate observations close to the analysis time without worsening the imbalance issue, but it does not improve the preservation of the Gaussianity of the ensemble.

To obtain some insights into this topic, a 4 days case study is considered and some experiments varying the length of the assimilation cycle are performed. Moreover, two experiments in which the window is shorter than the length of the assimilation cycle are presented and discussed. The set-up of all these experiments is described in Section 5.1. The quality of the analyses obtained from each configuration is assessed in terms of quantitative precipitation forecast (QPF) accuracy, employing the verification scores illustrated in Section 5.2. Verification results are reported in Section 5.3.

## 5.1 Experimental design

The experiments discussed in this chapter and in Section 6.1 are carried out over a period of almost 4 days from 3 February at 06 UTC to 7 February at 00 UTC in 2017, which is referred to as *feb2017*. During 3 and 4 February, middle tropospheric circulation over Northern and Central Italy was dominated by southwesterly divergent flows associated with the passage of some precipitating systems. On 5 February a trough moved from France to Italy and this caused the formation of new precipitating systems in Northern Italy. During 6 February the trough moved slowly from Central Italy to the southern part of the country and precipitation systems weaken gradually.

### 5.1.1 Assimilated observations

In the following experiments, both conventional observations and reflectivity volumes are assimilated through KENDA. The former includes aircraft measurement (AIREP) and radiosonde data (TEMP) of temperature, horizontal wind and relative humidity and surface station (SYNOP) of 2-meter temperature, 2-meter relative humidity, 10-meter horizontal wind and surface pressure. The number of observations available to be assimilated each hour for each data type and variable is reported in Table 5.1. Note that this does not coincide with the number of assimilated observations since a quality control procedure can reject a part of them, mainly because they may be affected by manifest errors or they may be too different from the corresponding background equivalents.

**Table 5.1.** Approximate number of conventional observations available each hour to be assimilated through KENDA. Note that the actual number of assimilated measurements depends on how much observations are rejected by the quality control algorithm. For each observation type, the temporal resolution is reported; for TEMP data it depends on the station and can vary from 6 to 24 hours.

| Obs. type | Variable | Temporal resolution | No. of obs. per hour |
|---|---|---|---|
| AIREP | temperature<br>horiz. wind<br>relative humidity | 1 min | 0-600<br>0-600<br>0-80 |
| TEMP | temperature<br>horiz. wind<br>relative humidity | 6-24 h | 0-1000<br>0-1000<br>0-100 |
| SYNOP | 2m temperature<br>10m horiz. wind<br>2m relative humidity<br>surface pressure | 1 h | 800-1100<br>800-1100<br>800-1180<br>800-1180 |

Regarding reflectivity data, only the two radars of ARPA Piemonte and ARPAL and the two of ARPAE Emilia-Romagna (solid circles in Figure 5.1) are assimilated, since they were the only ones available at that time. As discussed in Section 4.4, these radars differ for temporal and azimuthal resolution, as well as for range and elevations. After the superobbing procedure is applied, approximately 23.000 observations are available each hour for Bric della Croce radar (see Table 4.2),

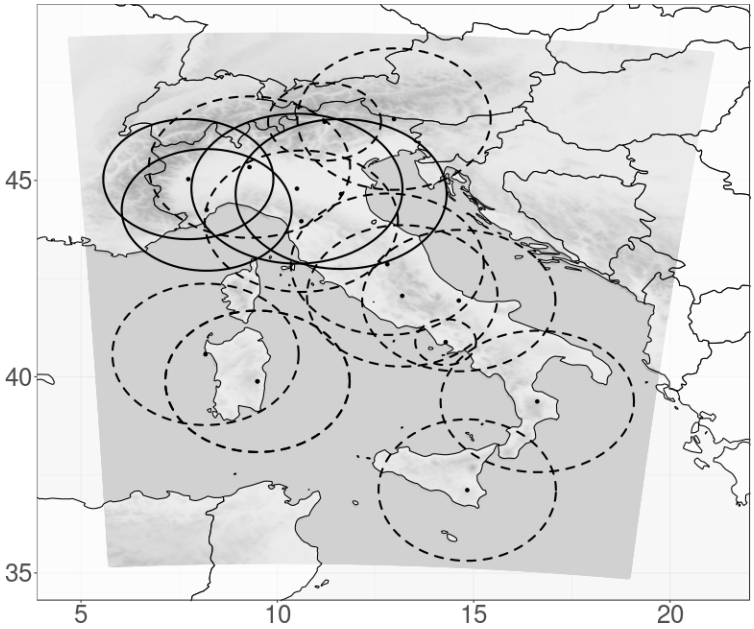


**Figure 5.1.** Radar assimilated in the experiments carried out on the *feb2017* period. For each radar, the approximate coverage area is shown with a dashed line if the radar system contributes only to generate the SRI composite employed in LHN and with a solid line if it is used also to directly assimilate reflectivity volumes through KENDA. The integration domain of COSMO-2I is also shown with a grey-scale.

41.000 for S. Pietro Capofiume radar, 87.000 for Settepani radar and 100.000 for Gattatico radar. Therefore, despite the use of superobbing, the number of reflectivity observations is much grater than that of conventional data.

In combination to reflectivity assimilation, SRI fields obtained from the whole Italian radar network (both solid and dashed circles in Figure 5.1) are assimilated through LHN in all experiments carried out over *feb2017* period. The hypothesis which justified this approach was that, in the KENDA framework, LHN allows one to have the model first guess closer to the observed atmospheric state, improving the analysis quality. Moreover, the larger coverage of SRI data can be exploited, improving analysis quality also in regions where reflectivity volumes are not available. However, in this way, radar data from ARPA Piemonte, ARPAL and ARPAE Emilia-Romagna are assimilated "twice": first the derived SRI product through LHN and, then, reflectivities with KENDA. Even if it is recognized that this may not be a rigorous process, it has to be pointed out that, actually, it is not the same information to be assimilated, mainly because SRI over Northern Italy

**Table 5.2.** List of experiments performed over *feb2017* period described in this chapter. For each experiment, the cycle length and the set of observations assimilated during each cycle are reported.

| Name | Cycle length | Assimilated obs. collected during the cycle |
|---|---|---|
| *rad60* | 60 min. | All |
| *rad30* | 30 min. | All |
| *rad15* | 15 min. | All |
| *rad60_lst15* | 60 min. | Only in the last 15 min. of the cycle |
| *rad60_lst* | 60 min. | All conventional, only the latest volumes |

is influenced also by other radars. In any case, since LHN is applied to all the experiments described in this chapter, this choice does not affect the comparison, especially considering that, as shown in Gastaldo et al. (2018) and in Appendix A, results obtained by assimilating reflectivity volumes in combination with LHN does not differ significantly from those obtained by only assimilating reflectivity observations.

### 5.1.2 Description of the experiments

Experiments discussed in this chapter are listed in Table 5.2 and they differ among each others only for the specifics of the assimilation window. In *rad60* both conventional observations and radar reflectivity volumes are assimilated with KENDA through cycles of 60 minutes. The assimilation window coincides with the length of the assimilation cycle. The observation error for all reflectivity data is set equal to 5 dBZ, as done in Tong and Xue (2005). In combination to KENDA, SRI fields obtained from the whole Italian radar network are assimilated by LHN. The same set-up is employed in experiments *rad30* and *rad15*, but with assimilation cycles (and windows) equal to 30 and 15 minutes respectively.

Regarding the assimilation of a subset of observations close to analysis time, two experiments are performed. In *rad60_lst15* the same configuration of *rad60* is used but only conventional and reflectivity observations collected in the last 15 minutes of each cycle are assimilated. In *rad60_lst* conventional observations are assimilated as in *rad60* while, for each radar station, only the reflectivity volume closest to the analysis time is taken into account. The approach employed in this

last experiment is based on the consideration that conventional data are much less than reflectivity measurements and they have a grater localization length scale. Therefore, the use of a too short assimilation window does not seem particularly advantageous for these observations.

For each experiment, analyses of the deterministic member of KENDA are used to initialize forecasts up to 12 hours every 3 hours from 3 February at 12 UTC to 6 February at 06 UTC with a total of 22 forecasts. These forecasts are employed to assess the analyses quality of the experiments described above.

## 5.2 Verification scores

The experiments described in Section 5.1.2 are compared in terms of QPF accuracy. To overcome the limitations of traditional scores for high-resolution models (Ebert, 2008), like the double-penalty problem (Rossa et al., 2008), two spatial methods are employed: the SAL technique, which is an object-based metrics, and the fractions skill score (FSS), based on a fuzzy approach.

For both methods, observations consist in hourly accumulated precipitation estimated from the Italian radar network and corrected with rain-gauges data. The method employed to perform this correction derives from Koinstinen and Puhakka (1981), but it is adapted for a radar composite. The original method comprises two terms: a range dependency adjustment and a spatial varying adjustment. In our case, only the second term is taken into account due to the fact that, in overlapping areas of the composite, rainfall estimation is obtained combining data from different radars and, therefore, the original information on the range distance from the radar is lost. The correction is based on a weighted mean of the ratio between rain gauges and estimated radar rainfall amount calculated over the station locations. Weights are a function of the distance of the grid point from the station and of a filtering parameter calculated as the mean spacing between 5 observations. Then, a smoothing factor is applied to the correction.

### 5.2.1 SAL

The SAL metrics (Wernli et al., 2008) is an object-based verification score. The detection of individual objects in the accumulated precipitation fields is achieved by considering continuous areas of grid points exceeding a selected threshold. Comparing objects from observed and forecast fields, SAL provides information about the structure $S$, the amplitude $A$ and the location $L$ errors of QPF. A perfect match between forecast and observations would lead to $S = A = L = 0$; the more the values differ from 0, the greater the disagreement between model and observations. More in detail, a too sharp/flat (broad/small) structure of forecast precipitation compared to observations is associated to positive (negative) values of $S$; an overestimation (underestimation) of average rainfall over the domain is associated to positive (negative) values of $A$; a misplacement of precipitating systems leads to positive values of $L$. Note that $L$ can range between 0 and 2, while $S$ and $A$ between -2 and 2.

The verification area is shown in dark gray in Figure 5.2, and the black dots inside it represent the rain-gauges which are employed to correct the rainfall estimation from the radar network. This area is chosen to cover approximately the domain where reflectivity volumes are assimilated. The choice of a larger domain would not be feasible, since in Wernli et al. (2009) it is recommended to use an area not larger than $500 \times 500$ km$^2$ because, otherwise, the domain may include different meteorological systems making the interpretation of results problematic. In fact, if the domain contains strongly differing meteorological systems, then results obtained using the SAL technique may not be representative of the weakest one.

To detect rainfall objects, two thresholds are employed here: 1 and 3 mm. Since general conclusions obtained comparing different experiments does not vary significantly when considering the 1 mm or the 3 mm threshold, only results for the former are shown in this study.

### 5.2.2 FSS

The Fractions Skill Score is a verification method introduced by Roberts and Lean (2008) based on the neighbourhood approach and applied to fractional coverage,

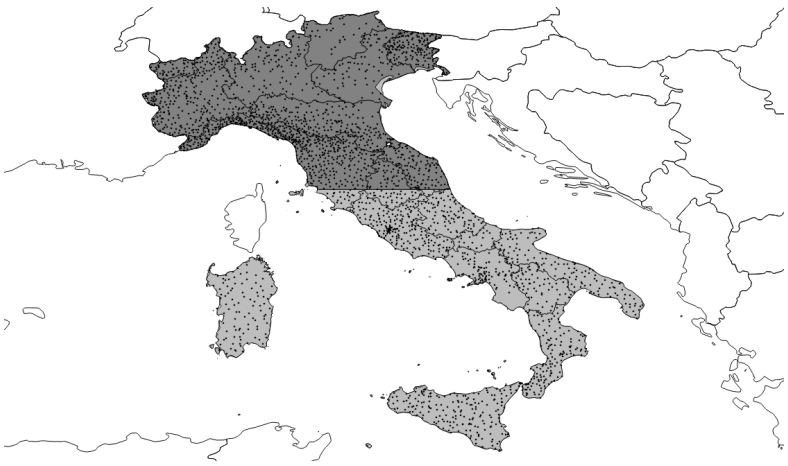

**Figure 5.2.** Verification domains employed to perform SAL (dark grey area) and FSS (union of dark grey and light grey areas) verification. The rain-gauges (black dots) are used to correct precipitation estimated from the Italian radar network; they are approximately 1500 in the dark grey area and 1300 in the light gray one.

that is the fraction of grid points exceeding a threshold. The score consists in comparing forecast and observed fractional coverages over squared boxes (neighbourhoods) and it ranges between 0 (completely wrong forecast) and 1 (perfect forecast). Therefore, a perfect match between model and observations is obtained when the two fields have the same frequency of events in each box. In this way, the method implicitly acknowledges that the actual resolution of a model is larger than the grid resolution and, at the same time, that also observations may contain random errors at the model grid scale. Like SAL, this approach allows to overcome the limitation of traditional grid point based scores. Furthermore, it can be applied over a domain larger than that employed for SAL since it is based on dichotomy events instead of being based on the amount of precipitation. For this reason, in this work FSS is applied over the whole Italian country (union of dark gray and light gray domains in Figure 5.2) considering boxes of 0.2° in both latitude and longitude.

Five thresholds are employed in this study: 0.1, 0.5, 1, 3 and 5 mm. Generally, differences among scores for the experiments performed here do not vary significantly when employing a 0.1, 0.5 or 1 mm threshold. The same holds also comparing results for the 3 mm threshold to those of the 5 mm one. As a consequence, to summarize results, only the 1 mm and 5 mm thresholds are shown here

for FSS verification.

## 5.3 Results

### 5.3.1 Shortening of the length of assimilation cycles

The impact of reducing the length of the assimilation cycle is assessed by comparing experiments *rad15*, *rad30* and *rad60*. The verification in terms of SAL of the 22 forecasts initialized from the analyses of each experiment is provided in Figure 5.3. Results are shown for the 1 mm threshold.

To summarize the results in a single plot, the approach of Gastaldo et al. (2018) is followed, which is adapted from that used in Davolio et al. (2017). In Figure 5.3, the average of the absolute value of each component of SAL is plotted as a function of lead time. The average is computed considering only cases in which at least one between the observed and the forecast rainfall fields consists of at least 1000 grid points, which is approximately equal to an area of $50 \times 50$ km$^2$. Using the absolute value of the components of SAL, only the magnitude of the error is considered, loosing the information on the type of error (e.g., for $A$, an overestimation of forecast precipitation cannot be distinguished from an underestimation). This choice slightly limits the potential of SAL but provides an intuitive picture of the overall performance of each experiment. Although forecasts are up to 12 hours, the verification is shown only for the first 8 hours, since after this lead time scores of the different experiments become very close.

Considering lead time +1h, the shorter the cycle the smaller the error in structure and amplitude but the smallest location error is associated to *rad30* while *rad15* and *rad60* are almost equal. Between +2h and +4h, both *rad15* and *rad30* have always larger errors than *rad60*, with the only exception of $S$ at +4h. In particular, a relevant worsening in the location of rainfall nuclei is observed at +3h and *rad60* is significantly better than both *rad15* and *rad30* in terms of the $A$ component in the whole interval considered. From lead time +5h onwards, differences among the 3 experiments become small and the results are mixed.

In order to strengthen the results obtained using SAL over Northern Italy, the verification of QPF is extended to the whole Italian country employing FSS.

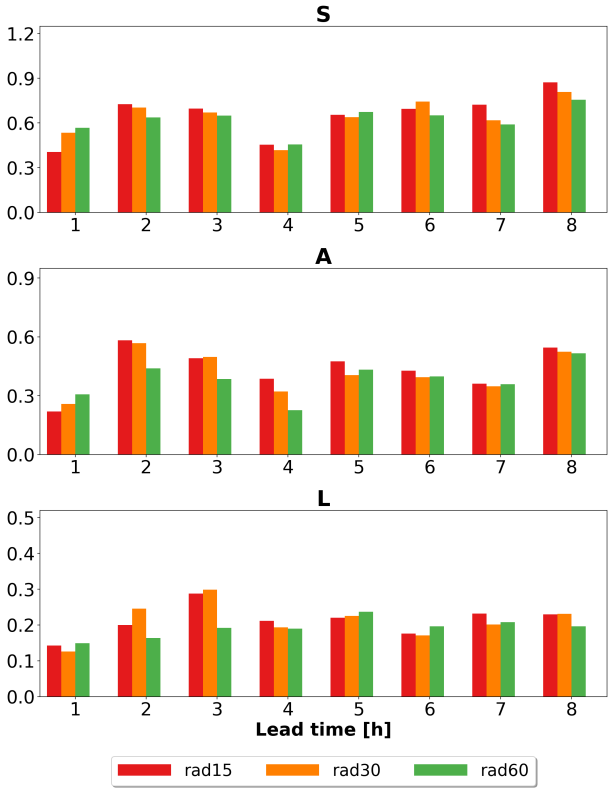


**Figure 5.3.** Average of the absolute value of each component of SAL over the 22 forecasts initialized from *rad15* (red), *rad30* (orange) and *rad60* (green) analyses. Objects are selected using a threshold of 1 mm in hourly accumulated precipitation fields. Cases in which both observed and forecast precipitation fields consist of less than 1000 points are not taken into account in the average.

Results are shown in Figure 5.4 for two thresholds: 1 mm (solid lines) and 5 mm (dashed lines). At lead time +1h no significant differences can be noticed among the 3 experiments for both thresholds. Between +2h and +4h, as observed with SAL verification, the shortening of the assimilation cycle leads to a worsening of the QPF accuracy, in particular at +2h and +3h. The differences between *rad60* and both *rad30* and *rad15* are larger for the 5 mm than for the 1 mm threshold. From +5h onwards, FSS values of all the experiments are similar even if *rad60* performs slightly worse than the other two experiments at +5h and +6h when considering the 5 mm threshold.

Overall, the use of assimilation cycles shorter than 60 minutes affects negatively the QPF accuracy and, at the same time, it increases computational costs.

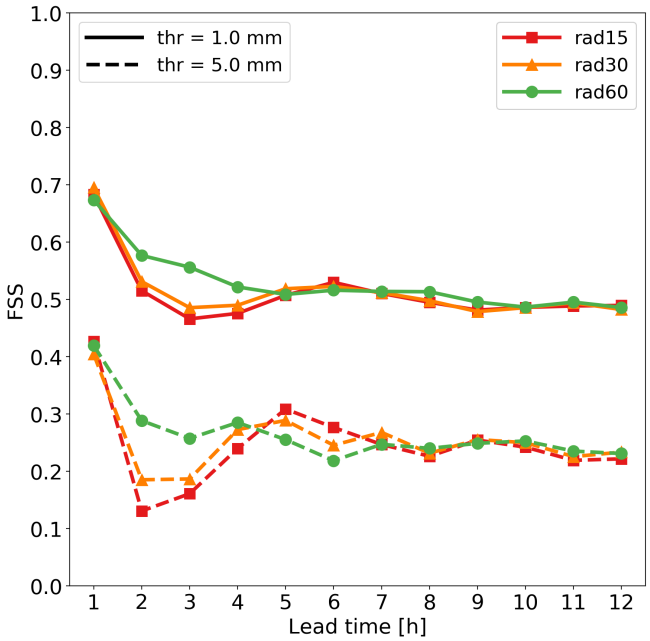


**Figure 5.4.** Fractions skill score as a function of lead time for *rad15* (red), *rad30* (orange) and *rad60* (green) experiments. Verification is performed considering hourly precipitation and 1 mm (solid lines) and 5 mm (dashed lines) thresholds.

Therefore, it is clearly disadvantageous to assimilate reflectivity volumes with sub-hourly cycles. In order to investigate the reason of this result, an assessment of the imbalance issue is performed in the following subsection.

### Quantification of the imbalance issue

The analysis increments derived in the data assimilation procedure may be incompatible with the dynamical balance of the background model state to which they are added. This results in the formation of spurious gravity waves which may affect the quality of the analysis (Stauffer and Seaman, 1990; Mitchell et al., 2002). In particular, if the imbalances introduced are not too severe, the model itself is able to eliminate them in few time steps, otherwise the model state may diverge significantly from the true one.

To quantify the imbalances, a common measure is the first time derivative of surface pressure $p_s$ averaged over the model domain (Stauffer and Seaman, 1990; Chen and Huang, 2006). In Figure 5.5, values of this quantity as a function of

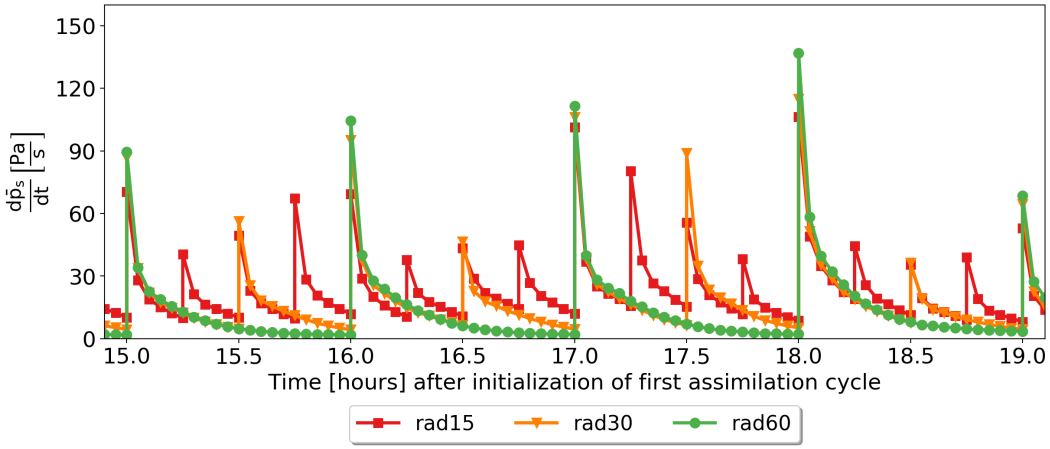


**Figure 5.5.** Domain averaged surface pressure tendency for *rad15* (red), *rad30* (orange) and *rad60* (green) experiments. Values are plot as a function of time starting from the initialization of the first assimilation cycle (3 February at 06 UTC). Only values ranging from the 15th to the 19th hour are shown.

time during assimilation cycles is shown for *rad15*, *rad30* and *rad60* experiments. When a new assimilation cycle is initialized for all the 3 experiments, that is at integer values of time, it can be observed that the imbalances are reduced by shortening the length of assimilation cycles. Therefore, a less frequent analysis update produces higher noise than more frequent updates, likely because the model diverges more from observations. However, only when employing 60 minutes cycles the surface pressure tendency decays almost to zero before the next assimilation cycle starts. In other words, in *rad15* and *rad30* experiments, the model is not able to completely remove spurious gravity waves through the forecast step of each assimilation cycle. These results, similar to those found in Bick et al. (2016), suggest that shortening the length of cycles leads to analyses which are less physically consistent and this leads to a worsening of forecast accuracy.

### 5.3.2 Use of subsets of observations

To evaluate the impact of assimilating only observations close to the analysis time without reducing the length of assimilation cycles, experiments *rad60_lst15* and *rad60_lst* are compared to *rad60*. As done in Section 5.3.1, SAL and FSS verifications are performed and the results are shown in Figure 5.6 and Figure 5.7

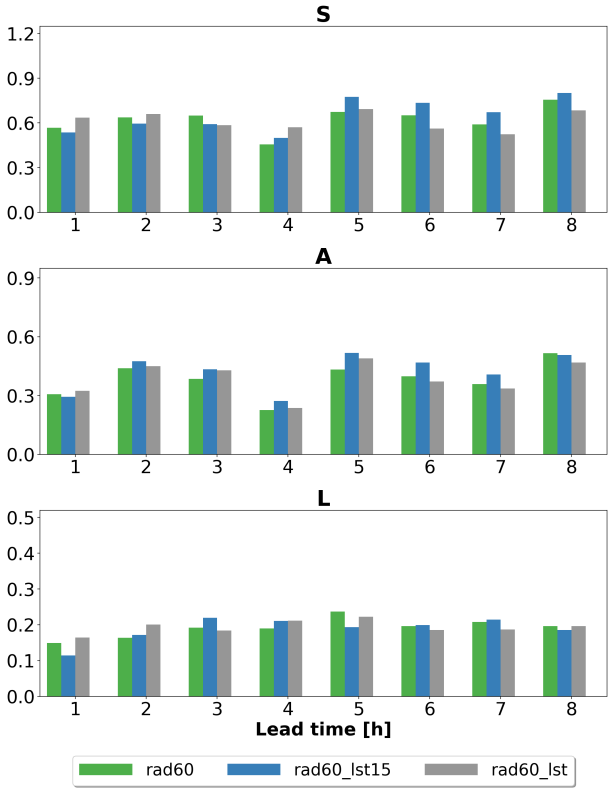


**Figure 5.6.** As in Figure 5.3 but considering experiments *rad60* (green), *rad60_lst15* (blue) and *rad60lst* (grey).

respectively.

Considering *rad60_lst15* experiment, SAL verification shows a slight improvement in all components of the score at lead time +1h compared to *rad60*. From +2h onwards, results are substantially mixed even if, overall, a slight worsening in amplitude can be observed. Extending the verification to the whole country of Italy with FSS, the substantially neutral impact of using *rad60_lst15* instead of *rad60* is confirmed for the 1 mm threshold. However, a slightly positive impact up to +8h can be observed considering the 5 mm threshold. In particular, QPF accuracy is strongly enhanced at lead times +1h, +4h and +5h.

SAL verification for *rad60_lst* experiment shows a slight worsening compared to *rad60* at the first 2 hours of forecast. From +3h to +5 results are mixed but from lead time +6h onwards *rad60_lst* slightly outperforms *rad60*. However, FSS verification with a 1 mm threshold shows a noticeable improvement only from +9h

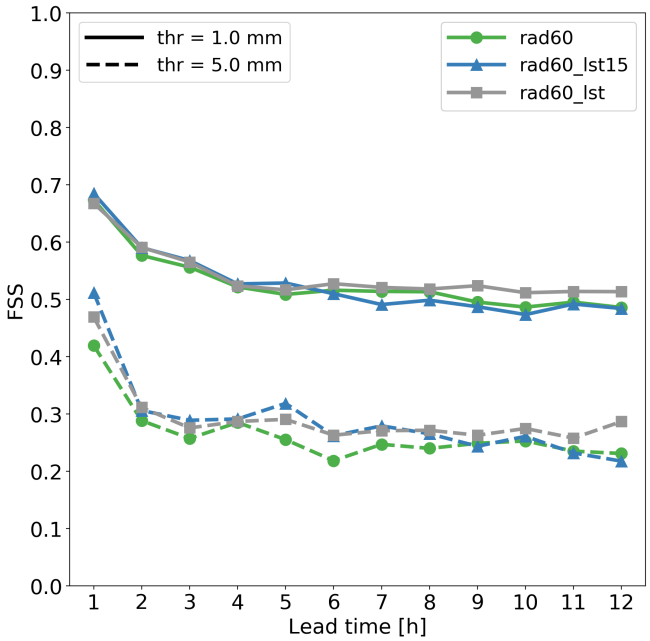


**Figure 5.7.** As in Figure 5.4 but considering experiments *rad60* (green), *rad60_lst15* (blue) and *rad60lst* (grey).

onwards, while at the previous lead times scores are very similar. As observed for *rad60_lst15*, the improvement of using *rad60_lst* instead of *rad60* is enhanced when considering the 5 mm threshold. In this case, the former slightly outperforms the latter over the whole forecast range.

In summary, a slight improvement in QPF accuracy is obtained when only observations close to analysis time are assimilated. The positive impact for both *rad60_lst15* and *rad60_lst* compared to *rad60* is more appreciable when considering precipitation stronger than 5 mm/h. Moreover, this improvement is associated to a reduction of computational costs related to the assimilation of reflectivity volumes, since less data are employed. Overall, except at lead time +1h, the configuration *rad60_lst* provides comparable or better results than *rad60_lst15*. Therefore, *rad60_lst* set-up is employed in all the experiments performed in the following Chapters with the exception of those described in Section 6.1.

# Chapter 6

# The impact of the reflectivity observation error

The observation error $\boldsymbol{\epsilon}^o$ and the background error $\boldsymbol{\epsilon}^b$ play a crucial role in any data assimilation system. In fact, the associated observation error covariance matrix $\mathbf{R} = E[\boldsymbol{\epsilon}^o(\boldsymbol{\epsilon}^o)^T]$ and background error covariance matrix $\mathbf{P}^b = E[\boldsymbol{\epsilon}^b(\boldsymbol{\epsilon}^b)^T]$ weight the impact of, respectively, observations and background state in determining the analysis.

In an EnKF scheme, $\mathbf{P}^b$ is estimated through the ensemble, providing a completely flow-dependent evaluation. On the contrary, the estimation of $\mathbf{R}$ is still an open issue. As described in more detail in Section 3.1, the observation error consists of a measurement error and a representation error (Janjić et al., 2017). Both terms are generally not known as well as the error covariances between pairs of observations and there is not a straightforward technique to estimate them. As a consequence, $\mathbf{R}$ is generally assumed to be diagonal, meaning that observations are treated as independent, and fixed in time. This is the approach employed operationally at ARPAE and in the experiments described in this study.

Due to the large amount of data, a reliable estimation of the error associated to reflectivity observations is crucial. To get some insights on this topic, a first sensitivity test is carried out and results are provided in Section 6.1. Then, an evaluation of reflectivity observation error (hereafter referred to as *roe*) as a function of space and time is discussed in Section 6.2 and the impact of this formulation on

**Table 6.1.** List of experiments performed over *feb2017* period discussed in Section 6.1. For each experiment, the cycle length and the reflectivity observation error employed for all radar data are reported.

| Name | Cycle length [min] | *roe* [dBZ] |
|---|---|---|
| *rad60_roe0.5* | 60 | 0.5 |
| *rad60* | 60 | 5 |
| *rad60_roe10* | 60 | 10 |
| *rad15_roe0.5* | 15 | 0.5 |
| *rad15* | 15 | 5 |
| *rad15_roe10* | 15 | 10 |

the data assimilation procedure is assessed in Section 6.3. Finally, an estimation of spatial correlation between reflectivity errors is provided in Section 6.4.

## 6.1 Sensitivity test

A set of experiments is performed to investigate the impact of the reflectivity observation error in the data assimilation scheme. The same experimental design of Chapter 5 is employed, meaning that the *feb2017* period is considered, the assimilated observations are those described in Section 5.1.1 and the verification is performed as discussed in Sections 5.2 and 5.3. The complete list of experiments discussed in this Section is reported in Table 6.1.

In the experiments described in Chapter 5, *roe* is set equal to 5 dBZ for all reflectivities, based on previous tests and on Tong and Xue (2005). Here, in addition to 5 dBZ, two other values of *roe* are tested: 10 dBZ and 0.5 dBZ. The former is employed by Bick et al. (2016) for the assimilation of reflectivity volumes from the German radar network using KENDA and COSMO and, therefore, should be reasonable also for the present study. The latter is a deliberately extreme value that may be chosen in the unrealistic case of a great confidence in the quality of radar observations and neglecting representation errors. These two different values of *roe* are used in assimilation cycles of 60 minutes (*rad60_roe0.5* and *rad60_roe10*) and 15 minutes (*rad15_roe0.5* and *rad15_roe10*). Therefore, they can be compared with the corresponding experiments with roe = 5 dBZ discussed in Chapter 5, that is *rad60* and *rad15* respectively.

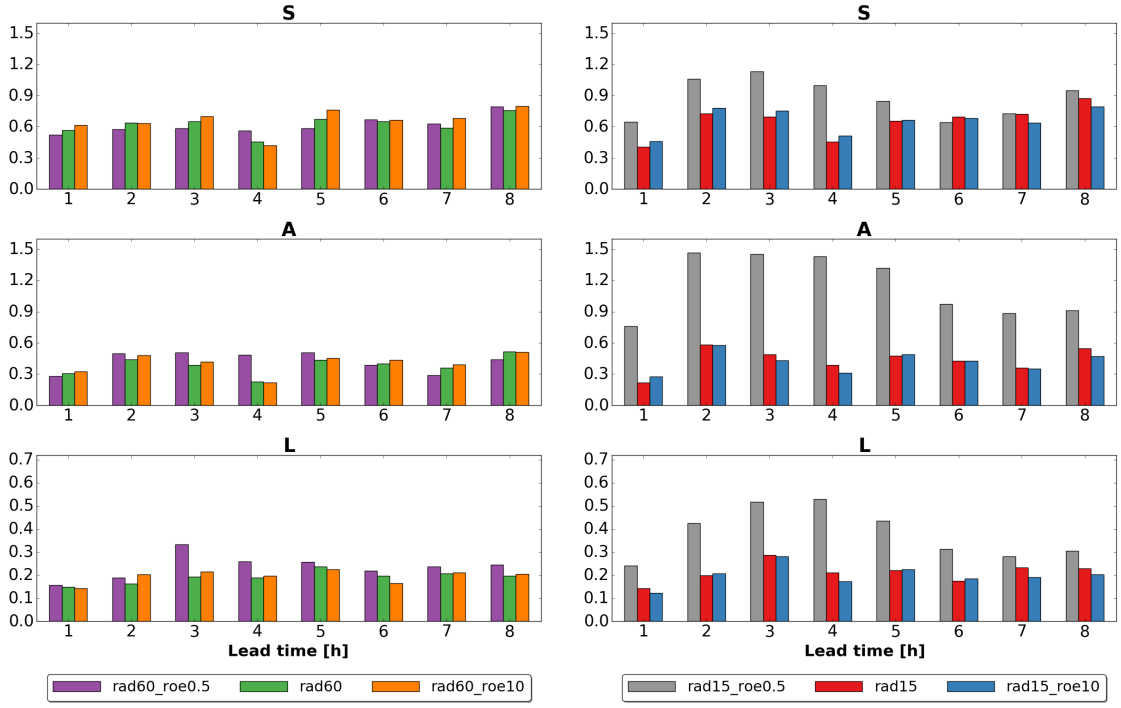


**Figure 6.1.** SAL verification as described in Section 5.2.1 and Section 5.3.1 considering, in the left panel, experiments *rad60_roe0.5* (violet), *rad60* (green) and *rad60_roe10* (orange) while, in the right panel, experiments *rad15_roe0.5* (grey), *rad15* (red) and *rad15_roe0.5* (blue).

Results of QPF verification in terms of SAL and FSS are reported, respectively, in Figure 6.1 and Figure 6.2. Regarding the experiments with a 60 minutes assimilation cycle, SAL verification (left panel in Figure 6.1) reveals that *rad60_roe0.5* slightly reduces structure and amplitude errors on QPF at lead time +1h compared to *rad60*, but the location error is very slightly increased. From +2h to +4h, *rad60_roe0.5* has a larger error in all components, except $S$ at +2h and +3h. In particular, the $A$ component is remarkably worsened at +4h and the $L$ component at +3h. Then, from +5h onwards the results become mixed. When comparing *rad60_roe10* to *rad60*, differences are small and mixed in the whole forecast range. The FSS verification, carried out over the whole Italian country, substantially confirms what observed with SAL. QPF accuracy of *rad60_roe0.5* from +2h to +4h is worse than that of *rad60* and the differences are even enhanced and extended to +1h when the 5 mm threshold is considered. Conversely, the impact of using a value of *roe* equal to 10 dBZ instead of 5 dBZ has an overall neutral impact,

even if a slight improvement can be noticed from +5h to +7h when considering the threshold of 5 mm.

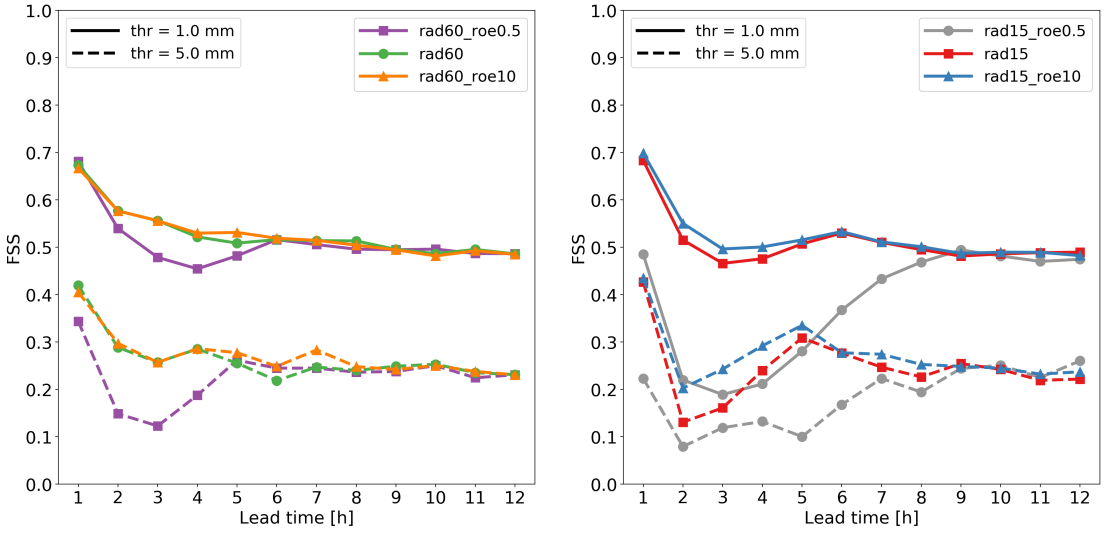


**Figure 6.2.** FSS verification as described in Section 5.2.2 considering, in the left panel, experiments *rad60_roe0.5* (violet), *rad60* (green) and *rad60_roe10* (orange) while, in the right panel, experiments *rad15_roe0.5* (grey), *rad15* (red) and *rad15_roe0.5* (blue).

Considering 15 minutes assimilation cycles, *rad15_roe0.5* dramatically worsens QPF accuracy over Northern Italy in terms of structure (right panel in Figure 6.1) up to +5h and up to +8h in terms of amplitude and location. In this regard, the verification of individual forecasts (not shown here) reveals that the large error in $A$ component is due to a systematic underestimation of the average precipitation over the domain. This marked worsening can be appreciated also with FSS verification (right panel in Figure 6.2), especially for the 1 mm threshold. Analysing the 10 dBZ case, SAL scores for *rad15_roe10* and *rad15* are similar and differences are mixed over the whole forecast range. However, in this case, FSS reveals that the former slightly outperforms the latter between +2h and +4h when the 1 mm threshold is considered and this is enhanced when considering the 5 mm threshold with a small improvement also at +6h and +7h.

In summary, the choice of a value of *roe* equal to 10 dBZ instead of 5 dBZ seems slightly advantageous, especially when using assimilation cycles of 15 minutes. On the contrary, reducing *roe* up to 0.5 dBZ significantly worsen QPF accuracy, in particular for the 15 minutes cycles case since analysis is forced more frequently

to be close to observations.

### 6.1.1 Impact on analysis of a too small observation error

The poor quality of *rad15_roe0.5* forecasts is the direct consequence of the poor quality of the analyses from which they are initialized. As an example, in Figure 6.3 the mean sea level pressure (MSLP; bottom row) and specific humidity at 850 hPa (top row) of *rad15_roe0.5* analysis (right column) on February 5 at 12 UTC are shown. These fields can be compared with the same quantities for the analysis of *rad15* (central column) and of the Integrated Forecasting System (IFS) of ECMWF (left column). Slight variations can be observed between IFS and *rad15* analyses and it seems reasonable that they may simply arise from differences between models and assimilation systems. Conversely, *rad15_roe0.5* analysis exhibits a noticeable increase in MSLP and a decrease in specific humidity over Northern Italy. This is in agreement with the decrease in forecast precipitation previously described.

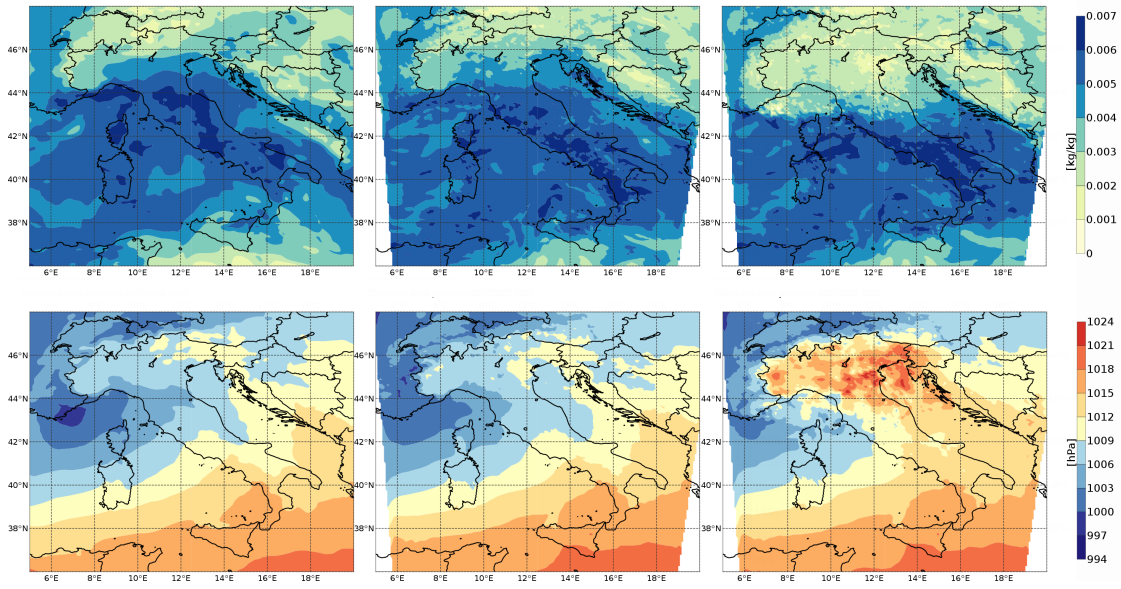


**Figure 6.3.** Analysis of mean sea level pressure (bottom) and specific humidity at 850 hPa (top) on 5 February at 12 UTC for IFS (left), *rad60* (middle) and *rad15_roe0.5* (right).

The remarkable degradation of analysis quality is due to a severe increase of imbalances. As an example, the difference between surface pressure tendency (see Section 5.3.1) for analysis of *rad15_roe0.5* and of *rad15* on 5 February at 12 UTC

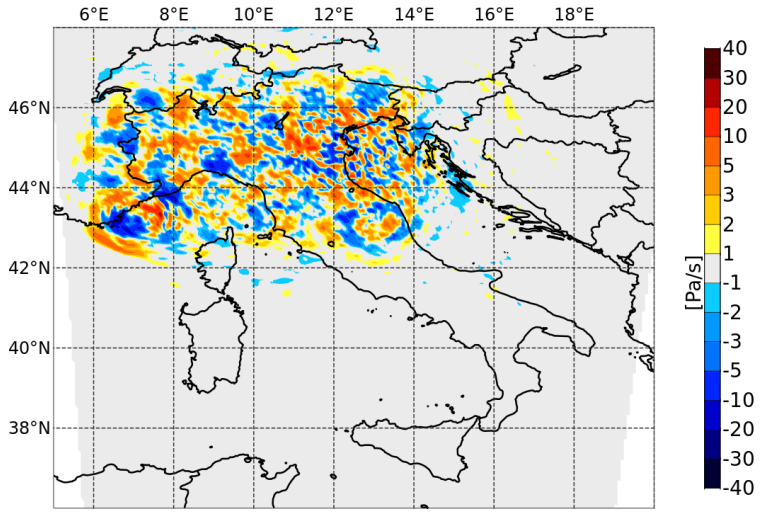


**Figure 6.4.** Difference in terms of surface pressure tendency between analyses of *rad15_roe0.5* and of *rad15* on 5 February at 12 UTC.

is shown in Figure 6.4. The region subjected to a significant increase (in module) of surface pressure tendency is, as expected, that in which reflectivity volumes are assimilated. Note that, in this case, the imbalances arises due to the use of a too small value of *roe* since the length of the assimilation cycles for the two experiments is the same.

To extend the investigation on the imbalance issue associated to values of *roe*, the kinetic energy (KE) spectra of experiments *rad15*, *rad15_roe0.5*, *rad60* and *rad60_roe0.5* are computed following the method described in Errico (1985). By this method, a linear detrending along the rows and columns of the model grid is applied to the velocity components of the model state in order to remove large unresolved scales which may distort the spectra obtained. Then, the two dimensional discrete Fourier transform is performed.

Curves displayed in Figure 6.5 are obtained as an average over the assimilation period (from 3 February at 06 UTC to 7 February at 00 UTC) of KE spectra computed each hour using analysis values of $u$, $v$ and $w$ at each level over the whole model domain. Kinetic energy spectra of *rad15* (red) and *rad60* (green) are almost overlapped, even at very small wavelengths, indicating that shortening the length of cycles from 60 to 15 minutes does not introduce significant imbalances in the analyses (Skamarock, 2004). In fact, as observed in Section 5.3.1, the issue

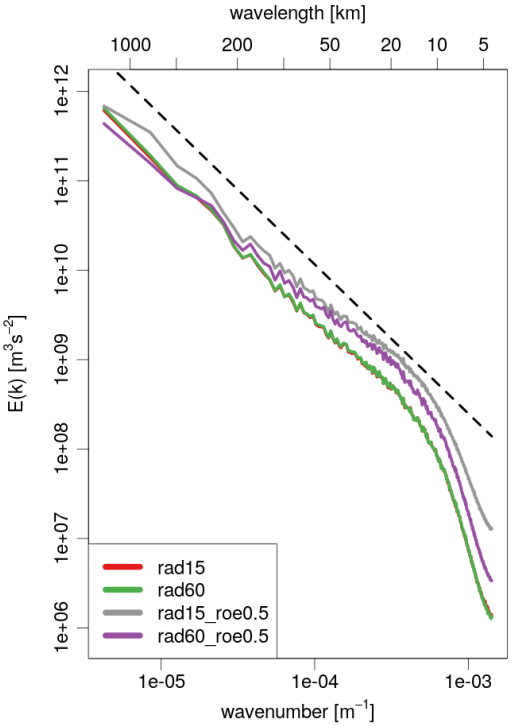


**Figure 6.5.** Kinetic energy spectra computed following the method described by Errico (1985). Each curve is obtained averaging KE spectra with a frequency of one hour during the assimilation procedure and employing analysis values of $u$, $v$ and $w$ over the whole model domain. The spectra are displayed for experiments *rad15* (red), *rad60* (green), *rad15_roe0.5* (grey) and *rad60_roe0.5* (violet). The dashed black line represents a function with a dependence to the wavenumber equal to $-5/3$.

associated to the shortening of cycles is not the increase of imbalances in the analysis (which are actually slightly decreased), but the inability of the model to remove them before the subsequent analysis is computed. Furthermore, both spectra have a $-5/3$ dependence on the wavenumber beyond a wavelength of 15-20 km, in agreement with observed spectra at the mesoscale (Nastrom and Gage, 1985).

Considering the experiments with *roe* equal to 0.5 dBZ, in both cases at the smallest wavelengths the KE is significantly greater that that of *rad15* or *rad60* and this is particularly evident for *rad15_roe0.5*. This behaviour is indicative of the presence of some undesired noise at small scales (Skamarock, 2004). Therefore,

employing a value of *roe* equal to 0.5 dBZ, the assimilation system generates a large amount of imbalances in the analyses, especially when really short cycles are employed. Furthermore, the excess of energy associated to the highest wavenumber modes propagates to the larger scales and the slope of the curves at wavelengths greater than 15 km differs from -5/3. As a result, analyses quality and forecasts accuracy are severely affected.

## 6.2 Estimation of the reflectivity observation error

Several methods have been developed for estimating the observation error covariance $\mathbf{R}$ (see Janjić et al. (2017) for a review) and, consequently, the observation errors, i.e. the square root of the diagonal of $\mathbf{R}$. One of these is the diagnostic proposed in Desroziers et al. (2005) which has become popular in recent years due to its simplicity. This technique is described in Section 6.2.1 and, in this study, it is applied to derive a spatio-temporal estimation of *roe* which is described in Section 6.2.3.

### 6.2.1 The Desroziers diagnostics

In the derivation of the diagnostics, it is assumed that the analysis is obtained by using the best linear unbiased estimator (BLUE), that is employing Eq. (3.11) and Eq. (3.13) which are reported here for convenience:

$$\begin{aligned}\mathbf{x}^a &= \mathbf{x}^b + \mathbf{K}\left(\mathbf{y}^o - \mathbf{H}\mathbf{x}^b\right)\\ \mathbf{K} &= \mathbf{P}^b\mathbf{H}^T\left(\mathbf{H}\mathbf{P}^b\mathbf{H}^T + \mathbf{R}\right)^{-1}\end{aligned}$$

Indicating by $\mathbf{d}_b^o$ the innovation or background residual $\mathbf{y}^o - \mathbf{H}\mathbf{x}^b$, the analysis residual is provided by

$$\mathbf{d}_a^o = \mathbf{y}^o - \mathbf{H}\mathbf{x}^a = \mathbf{y}^o - \mathbf{H}\mathbf{x}^b - \mathbf{H}\mathbf{K}\mathbf{d}_b^o \tag{6.1}$$

It can be demonstrated (see Desroziers et al., 2005) that the statistical expectation of the cross product between $\mathbf{d}_a^o$ and $\mathbf{d}_b^o$ is

$$E[\mathbf{d}_a^o(\mathbf{d}_b^o)^T] = \mathbf{R} \tag{6.2}$$

provided that background and observation errors are uncorrelated, as prescribed by Kalman filter assumptions (see Section 3.2). Equation (6.2) is exact if both $\mathbf{P}^b$ and $\mathbf{R}$ used in assimilation are exact. In practice, the statistics used in the assimilation will not be exact. To account for this issue, the authors of the method suggest applying the diagnostics in successive iterations, until convergence of the estimation of $\mathbf{R}$.

Despite the several assumptions made, the diagnostic has been successfully used in complex operational models to estimate the observation errors and covariances (e.g.Stewart et al., 2014; Weston et al., 2014; Bormann et al., 2016; Waller et al., 2016). However, most of these works have considered variational data assimilation methods. The application to ensemble assimilation algorithms is not straightforward because localization is employed and, therefore, analysis is not retrieved using BLUE. Waller et al. (2017) demonstrated that, in this case, the diagnostic Eq. (6.2) does not hold in general. However, some elements of $\mathbf{R}$ can still be estimated through this equation. For a generic observation $y_i$, we can define its *region of influence* as "the set of analysis states that are updated in the assimilation using the observation $y_i$" and its *domain of dependence* as "the set of elements of the model state that are used to calculate the model equivalent of $y_i$. A sketch of the region of influence and of the domain of dependence is illustrated in Figure 6.6. According to those definitions, Waller et al. (2017) states that the correlation between the errors of observations $y_i$ and $y_j$ can be estimated using the diagnostic provided by Eq. (6.2) only if the domain of dependence for observation $y_i$ lies within the region of influence of observation $y_j$.

Due to the choice of horizontal and vertical localization length scales described in Section 3.3, the region of influence for each reflectivity observation is a cylinder with a radius of approximately 58 km. If attenuation is not taken into account to derive equivalent observations with the radar operator, as for all the experiments discussed in this chapter, only model grid points employed for the calculation of the

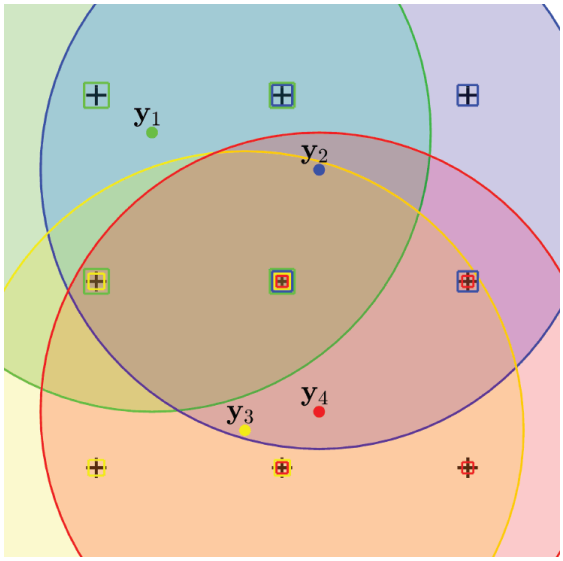


**Figure 6.6.** Schematic taken from Waller et al. (2017) of the regions of influence and domains of dependence for four observations (dots). Observations are coloured with corresponding regions of influence while analysis grid points are represented by pluses. Assuming that the model equivalent observations are calculated using the four nearest model states, the coloured squares around grid points select the points that would be utilized by the observation operator for the observation of the corresponding colour.

superobservation determine the domain of dependence of a reflectivity. Therefore, the domain of dependence of each reflectivity observation is approximately a square with a side of 10 km. As a consequence, the covariance between the errors of observations $y_i$ and $y_j$ can be estimated using Desroziers diagnostics if $y_j$ is inside the cylinder which axis passes through $y_i$ and which radius is approximately 51 km $\left(58 - \frac{10\sqrt{2}}{2}\right)$. In particular, this implies that Desroziers diagnostics defined by Eq. (6.2) can be employed to estimate *roe*.

### 6.2.2 Experiment set-up for case studies in 2018

Three periods, named *set2018*, *oct2018* and *nov2018*, are considered to estimate *roe* and to perform some experiments described in this chapter and in the following ones. The end and start dates of each period are reported in Table 6.2 with the main kind of precipitation occurred.

These three periods have been selected because of the different meteorological weather regimes that occurred. During *sept2018* a weak trough from Northern

**Table 6.2.** For the 3 periods in 2018 considered in this chapter and following ones, the end and start dates are reported together with the main kind of precipitation occurred.

| Name | Start date | End date | Main type of event |
|---|---|---|---|
| *sept2018* | 31/08 at 00 UTC | 09/09 at 00 UTC | Thunderstorms |
| *oct2018* | 30/09 at 15 UTC | 14/10 at 00 UTC | Organized thunderstorms |
| *nov2018* | 26/10 at 12 UTC | 11/11 at 00 UTC | Stratiform precipitation |

Europe approached Italy between 31 August and 1 September which, then, turns in a cut-off centred over Northern Italy until 4 September. Afterwards, a weak cyclonic circulation affects Central and Northern Italy, gradually replaced by a ridge by the end of the period. Therefore, *sept2018* is characterized by non-organized instability with short-living showers and thunderstorms affecting mainly Central and Northern Italy.

At the beginning of the *oct2018* period, a trough crossed Italy from North to South with subsequent formation of a cut-off which stayed over Southern Italy between 3 and 5 October. A new trough approached North-Western Italy in 6 October and then a cut-off was present between Southern France and Eastern Spain until 9 October. Between 10 and 11 October, North-Western Italy and Sardinia region were interested by humid south-westerly flows. Finally, a cut-off between Southern Italy and Greece was present in the last part of the period. Overall, this period is characterized by more organized convective precipitation systems compared to *sept2018* with some long-living stationary thunderstorms which led to two severe flash floods: the 5 October in Calabria region and the 10 October in Sardinia region.

In *nov2018* a deep trough between Western Mediterranean Sea and Western Europe determined warm and humid southerly flows over Italy for several days. In particular, very strong winds and precipitations were reported between 28 and 30 October in different regions of the country. The circulation changed to westerly flows only by the end of the period. In *nov2018* precipitations are then more organised and spatially extended than in the other periods.

Differently from experiments run over the *feb2017* period, here also reflectivity volumes from DPC radars were available to be assimilated. Therefore, all radars

depicted with a solid line in Figure 4.4 are employed in these 3 periods. Moreover, a substantial difference compared to the *feb2017* experiments is that LHN is not applied. In fact, as discussed in Section 5.1.1, the assimilation of both reflectivity volumes through KENDA and SRI by LHN is not a rigorous process since it can be argued that a partly similar information is assimilated twice. This would be more problematic for *sept2018*, *oct2018* and *nov2018* periods because the radars which are employed to derive SRI fields are almost the same for which reflectivities are assimilated. Furthermore, employing also DPC radars, it makes no more sense to use LHN since reflectivity data cover the whole Italian country.

All experiments performed in this study over *sept2018*, *oct2018* and *nov2018* periods have the following common features:

- assimilation cycles are of 60 minutes;
- conventional observations assimilated are the same described in Section 5.1.1;
- all conventional observations collected during each assimilation cycle are assimilated;
- for each radar station (solid lines in Figure 4.4) only the volume closest to the analysis time is assimilated;
- a 12 hours forecast is initialized from the deterministic analyses every 3 hours; accordingly, for each experiment 72 forecasts are performed for *sept2018* period, 107 for *oct2018* and 124 for *nov2018*.

The experiments involving radar reflectivity assimilation performed over at last one of the 3 periods in 2018 differ among each other for the value of *roe* and for the specifics of the radar operator employed. The former are discussed in this chapter while the others in Chapter 7. The complete list of these experiments with specifics for *roe* and radar operator is provided in Table 6.3.

### 6.2.3 A spatio-temporal estimation of reflectivity observation error

To derive a spatial dependence for *roe*, the diagonal of $\mathbf{R}$ is estimated with Desroziers diagnostics applied to residuals from *err_fix* experiment in which the

**Table 6.3.** List of experiments performed on at least one among *set2018*, *oct2018* and *nov2018* periods. For each experiment, the way *roe* is characterized is reported: a numeric value indicates that all reflectivities have the same observation error while for a detailed description of the spatial and/or temporal dependence refers to Section 6.3. Moreover, the specifics of the EMVORADO operator regarding the scattering theory employed and the taking into account of attenuation are reported. Some experiments are referred to with two different names, depending on the chapter in which they are discussed.

| Name | *roe* | Scattering theory | Attenuation |
|---|---|---|---|
| *err_fix/oper_Ray* | 10 dBZ | Rayleigh | No |
| *err_mean* | space dependent | Rayleigh | No |
| *err_period* | time and space dep. | Rayleigh | No |
| *oper_Mie* | 10 dBZ | Mie | No |
| *oper_Mie_att/conv+refl* | 10 dBZ | Mie | Yes |

value of *roe* is set equal to 10 dBZ (according to results of Section 6.1) for all observations. Then, the elements of the diagonal are binned according to the distance of the associated observations from radar station. The binning procedure is performed both in the horizontal and in the vertical with, respectively, a 50 km and a 2 km step. This is schematically shown in Figure 6.7. Finally, an average value of *roe* is computed for each bin considering all azimuth angles. It is important to observe that a bin may include beams at different elevations. For example, for the red contoured bin in Figure 6.7, a value of *roe* is computed taking into account observations which are at an horizontal distance from the radar station between 50 km and 100 km and a vertical distance between 2 km and 4 km. These observations arise from beams at 3 different elevations. Similar process for the green contoured bin but, in this case, observations are between 150 km and 200 km from the radar station in horizontal, between 4 km and 6 km in vertical and they arise from 2 beam elevations. Note that, since a 5 dBZ threshold is applied (see Section 4.3.2), if an observation or its background equivalent is equal to 5 dBZ the corresponding residuals are not taken into account for the computation of *roe*. In fact, these values are ad hoc set to 5 dBZ and, therefore, if they were considered, they would compromise the results of the diagnostics.

The method is applied separately to each radar station and an average over each period in 2018 (*sept2018*, *oct2018* and *nov2018*) is computed. This allows

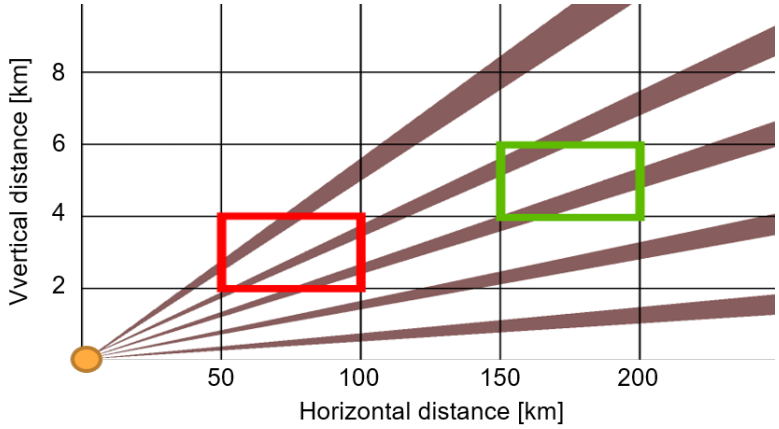


**Figure 6.7.** Sketch of the binning procedure performed to derive a spatial dependence of *roe*. At a specific azimuth, radar beams (grey) at different elevations are generated by the radar station (orange circle). Estimated errors associated to all observations in one bin are averaged to obtain a value of *roe* for each bin; the average is computed over all azimuth angles.

to evaluate the temporal variability of the estimated values of *roe*. As far as the author knows, this kind of spatio-temporal dependence of observation error has never been applied to reflectivity volumes. Regarding spatial dependence, an estimation in terms of range distance has been performed in Waller et al. (2016) for radial winds, but considering each elevation separately. This estimation of error as a function of range and elevation has also been performed in this study for reflectivities, but the results are not shown here since they are less consistent than those obtained as a function of horizontal and vertical distance.

Estimated values averaged over the three periods (*sept2018*, *oct2018* and *nov2018*) and over all radars of the Italian network available for reflectivity assimilation (depicted with solid lines in Figure 4.4) are shown in Figure 6.8. The average, as all averages performed in the following of this chapter, is computed according to sample sizes. Values of *roe* ($y$-axis) are plot as a function of horizontal distance ($x$-axis) and vertical distance (colours) from the radar station. As a general behaviour, *roe* increases with horizontal distance. This result is reasonable since the size of observed atmospheric volumes increases with the distance from the radar station. Accordingly, some assumptions made to compute reflectivity, like the uniform filling of the observed atmospheric volume and the single scattering hypothesis, are far from being realistic. Moreover, errors due to the correction for

attenuation in observations are likely to increase. Regarding vertical distance from the radar station, values of *roe* decrease with height up to the 4-6 km bin and then stabilize. Also this behaviour is reasonable since reflectivity observations close to the ground are more likely affected by non-meteorological signals (i.e. clutter).

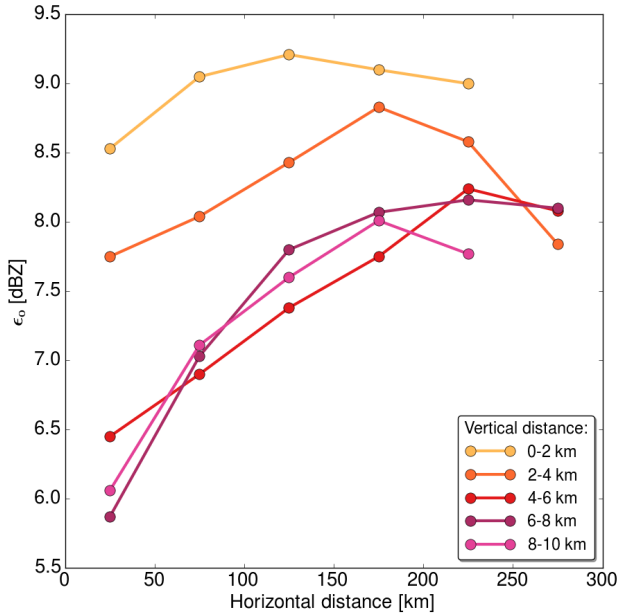


**Figure 6.8.** Estimated values of *roe* as a function of horizontal distance ($x$-axis) and vertical distance (colours) from radar station. Values are obtained by averaging over all periods and over all stations depicted as a solid line in Figure 4.4.

Due to the heterogeneity of our radar network and to the presence of different weather regimes in Italy, when the diagnostics is applied separately to each radar a certain variability can be noticed. As an example, in Figure 6.9 estimated values of *roe* are shown for Serano radar (left panel) in Central Italy and for Zoufplan radar (right) in North-Eastern Italy. Values are averaged over the 3 periods *sept2018*, *oct2018* and *nov2018* and they are plot only if obtained from a sample consisting of at least 1000 pairs of residuals. It can be noticed that the general behaviour described above is conserved but values and slopes of the curves vary quite significantly.

A certain variability can be observed also when considering one radar but restricting the statistics to a single period. This is shown, for example, in Figure

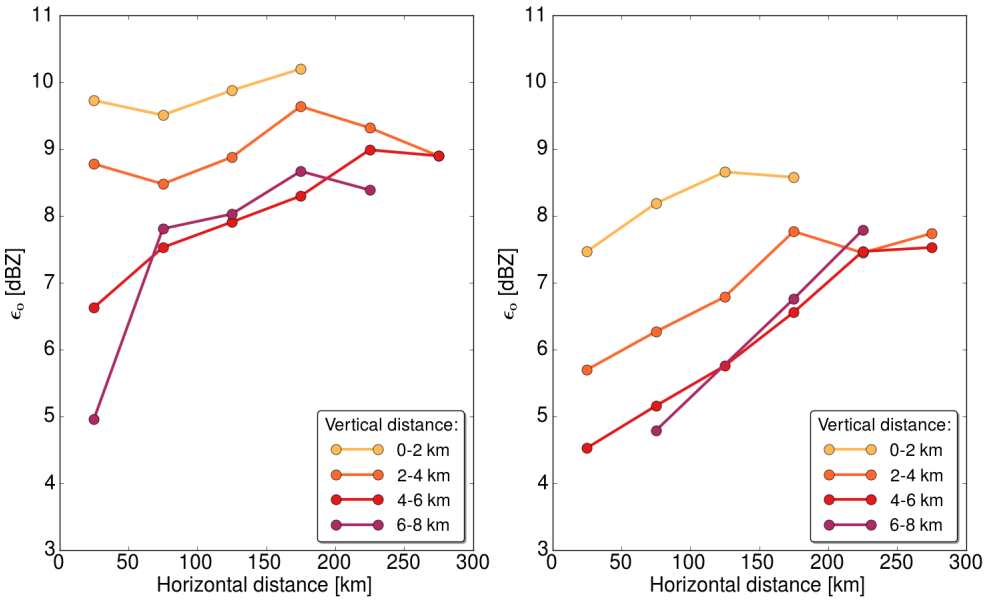


**Figure 6.9.** Same as Figure 6.8 but computing the diagnostics only for Serano radar (left) in Central Italy and Zoufplan radar (right) in North-Eastern Italy. Only values obtained from a sample which size is greater than 1000 are plot.

6.10 for Zoufplan radar applying the Desroziers diagnostics only to *sept2018* period (left panel) and to *nov2018* (right). Again, even if the general behaviour observed in Figure 6.8 is maintained, the different weather regime in the two periods impacts on values of *roe*. This is particularly remarkable for bins which vertical distance from the radar is between 4 and 6 km.

The estimated values of *roe* shown here are obtained from a unique application of the Desroziers diagnostics. As discussed in Section 6.2.1, the results of this first estimation should be employed in the data assimilation procedure and then Desroziers diagnostics would have to be performed again. This process should be iterated until convergence of *roe* values. However, due to the results (see Section 6.3) obtained by assimilating reflectivities using this first estimation of *roe*, which should already be quite accurate (Desroziers et al., 2005; Bathmann, 2018), and considering the high computational costs of run all these experiments, here the Desroziers statistic is not iterated.

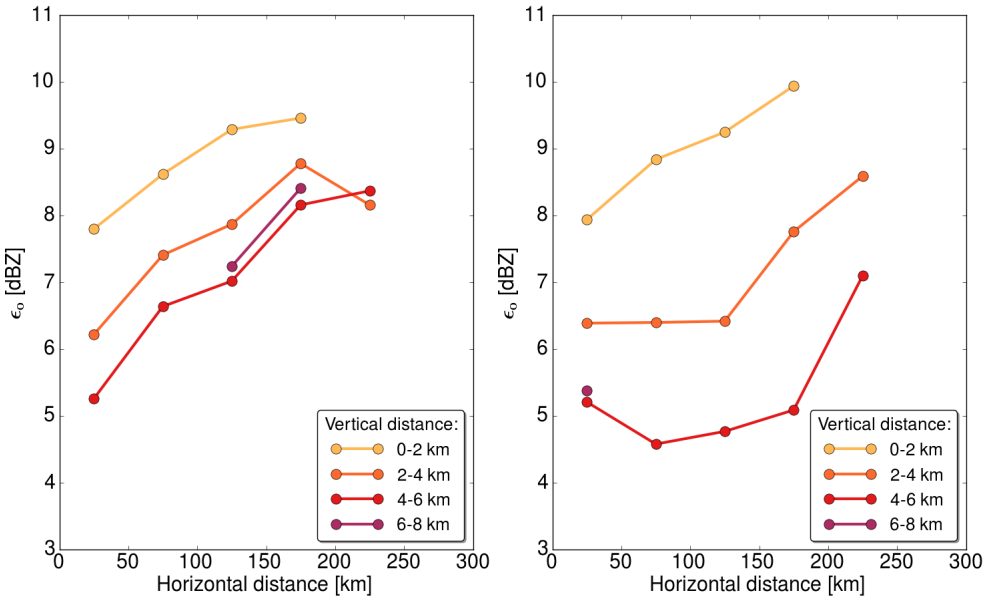


**Figure 6.10.** Same as Figure 6.8 but computing the diagnostics only for Zoufplan radar at two different periods: sept2018 (left) and nov2018 (right).

## 6.3 Impact of using estimated errors on data assimilation

In order to evaluate the impact of using the estimated values of *roe* on the KENDA assimilation system, three experiments are performed. In *err_fix* experiment all reflectivity observations have an error of 10 dBZ, according to the results obtained in Section 6.1. Note that 10 dBZ is a slightly inflated value compared to the one obtained by applying the Desroziers diagnostics to all radar reflectivities (approximately 8.5 dBZ). In *err_mean* experiment, *roe* varies with radar station and with horizontal and vertical distance from station and it is averaged over all periods. Finally, in *err_period* experiment, *roe* varies with radar station, with horizontal and vertical distance from station and with period.

The three experiments are performed over *sept2018* and *oct2018* periods. Forecasts are evaluated with FSS, as described in Section 5.2.2. Note that for the 3 periods considered in 2018, the application of SAL would not be feasible since precipitations involved all of Italy and the choice of the whole country as verification

area would lead to some problems in interpreting the results (see Section 5.2.1).

Results of FSS verification are shown in Figure 6.11. Differences between the three experiments are small for both *sept2018* (left panel) and *oct2018* (right panel) periods. Regarding *sept2018*, FSS values for *err_mean* (red lines) are very close to those of *err_fix* (orange) for both the 1 mm (solid lines) and the 5 mm (dashed lines) thresholds. In contrast, the performance of *err_period* (green) is equal or slightly better than that of the other two experiments, with the only exception for the 5 mm threshold at lead time +6h. Considering the *oct2018* case, scores for *err_mean* experiment are equal or slightly worse than that of *err_fix*, except at +1h and +5h for the 5 mm threshold. Similar results are obtained when comparing *err_period* to *err_fix* but, in this case, a clear worsening can be observed at +2h and +3h for the 5 mm threshold.

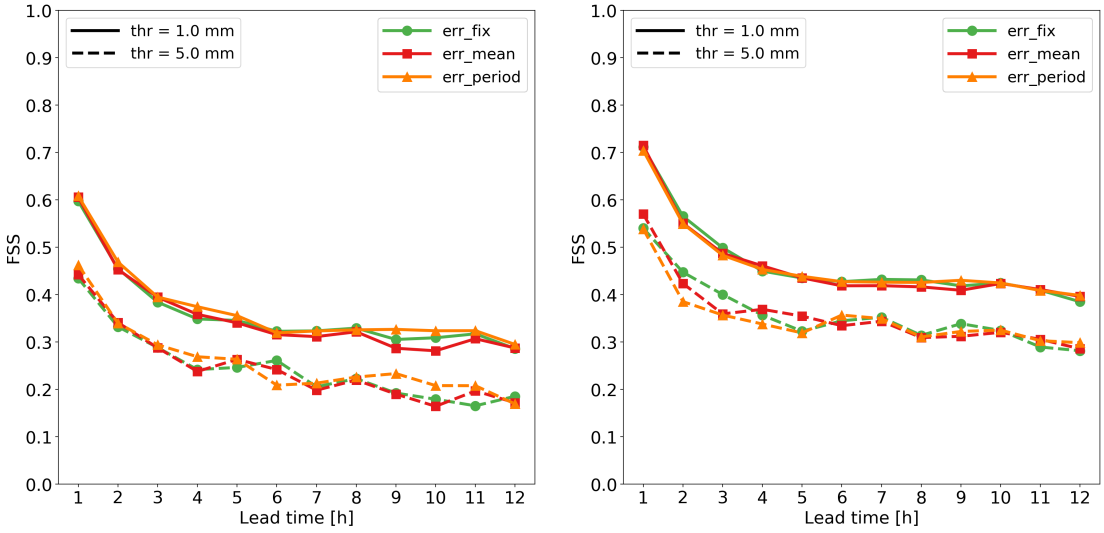


**Figure 6.11.** FSS verification as described in Section 5.2.2 for *err_fix* (green lines), *err_mean* (red) and *err_period* (orange) experiments. The verification is applied to *sept2018* (left panel) and to *oct2018* (right panel) periods.

Overall, even if *roe* varies significantly with radar station, with distance of observations from radar and meteorological conditions (i.e. period considered), employing a more complex characterization of *roe* instead of a unique value for all reflectivities does not improve QPF accuracy. This is likely due to a combination of two reasons:

- the sample employed to derive *roe* vales is too small;

- the estimated values of *roe* have to be used with the correspondent covariances estimated by Desroziers diagnostics.

Regarding the last point, estimated values of error correlations between reflectivity observations is provided in the following section.

## 6.4 Estimation of spatial correlation between reflectivity errors

The Desroziers diagnostics has been employed to estimate spatial error covariances between reflectivity observations. To achieve this, the same procedure used for estimating *roe* described in Section 6.2.3 is employed here but, instead of computing the diagonal of $\mathbf{R}$, the whole matrix is calculated via Eq. (6.2). Moreover, in this case, horizontal and vertical distances considered in the binning procedure are the distances between pairs of observations. Finally, the horizontal step for binning is 10 km and the vertical step is 1 km.

The estimation has been performed only for the *sept2018* period and an average over all radars, weighted with sample size, is computed. Results in terms of correlation (colours) are plot in Figure 6.12 as a function of horizontal ($x$-axis) and vertical ($y$-axis) distances. Note that, according to the discussion in Section 6.2 about the use of Desroziers diagnostic in a local ensemble data assimilation system, the maximum horizontal distance plotted is 50 km. A significant error correlation (greater than 0.2) can be observed between all observations in a vertical column of 10 km of radius and up to approximately 38 km in horizontal.

Accordingly, the use of a diagonal $\mathbf{R}$ matrix, i.e. to consider observations as independent, is not correct for our implementation of the assimilation of reflectivity volumes. The right way to proceed would be to account for covariances in $\mathbf{R}$ but the implementation is not trivial since the matrix has to be inverted. First of all, this means that the estimated matrix has to be symmetric and positive defined (SPD). This is not guaranteed by Desroziers diagnostics and, therefore, a technique to make estimated matrix SPD (e.g. Higham, 2002) has to be applied. Furthermore, the inversion of a very large matrix (in our case it is of $\mathcal{O}(10^6)$) is very costly from a computational point of view. In order to partly reduce

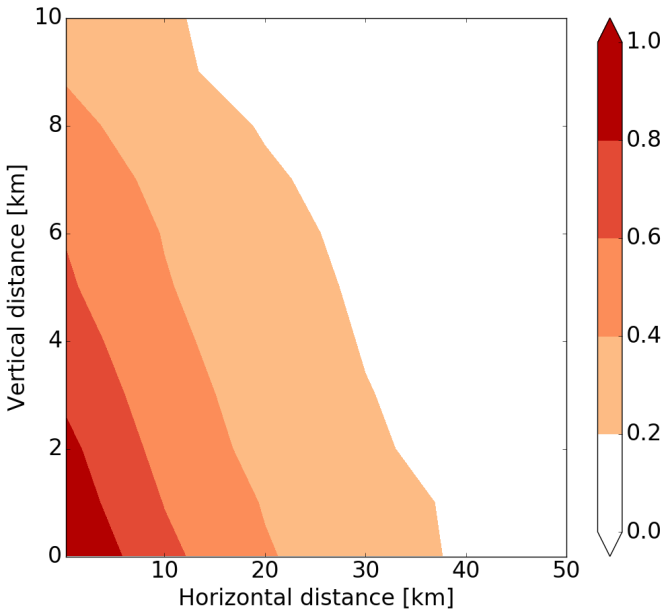


**Figure 6.12.** Spatial correlation between pair of reflectivity observations during *sept2018* period.

costs, $\mathbf{R}$ may be defined as a block diagonal matrix with a diagonal block for conventional observations and a non-diagonal block for each radar station. In this way, neither error covariances between observations from different radars nor error covariances between reflectivities and conventional observations are taken into account but computational costs are significantly reduced since the inversion of $\mathbf{R}$ results in inverting each block separately. However, the computational costs would be probably not feasible for an operational implementation.

A possible different approach to avoid to implement a non-diagonal $\mathbf{R}$ matrix but, at the same time, accounting for the results described in this Section would be to apply thinning to reflectivity observations. In particular, to make observations independent, only one should be present in a vertical column and the horizontal thinning should be applied in order to have observations spaced of approximately 40 km. As a consequence, this would determine a significant reduction of assimilated data and of computational costs but the high spatial density of radar data would not be exploited.

In this work, due to the lack of time, neither the use of a non-diagonal $\mathbf{R}$ matrix

nor the application of the thinning procedure have been tested, but both deserve to be further investigated. In case the former would be implemented, an improvement in describing small scales features in the analysis is expected (Rainwater et al., 2015) which, in turns, would lead to an improvement in forecast accuracy. Such an improvement has been observed when accounting for inter-channel correlations in the assimilation of satellite data (e.g. Weston et al., 2014; Campbell et al., 2017). However, as far as the author knows, there are not studies about the assimilation of radar reflectivity volumes in which spatial correlations between observations are accounted for. Regarding, the application of the thinning procedure to superobservations, only a very slight improvement can be expected, since the reduction of correlations between observations would be partly compensated by the reduction of available information on the state of the atmosphere.

# Chapter 7

# The impact of radar operator specifics

The EMVORADO operator allows to simulate the background equivalent of radar reflectivity observations employing different configurations. In particular, the user can choose the scattering theory (Rayleigh or Mie), the model for beam propagation and if taking into account the attenuation along the beam or not. Increasing the accuracy of simulated reflectivities (e.g. selecting Mie scattering theory instead of Rayleigh one) should improve the quality of analyses produced by the data assimilation procedure, since innovations should be better characterized. However, this is associated to an increase of the complexity of the radar operator and, therefore, to an increase in computational costs. Accordingly, the employment of a more complex configuration of the radar operator has to be justified by an appreciable improvement in analyses and forecasts accuracy.

In this chapter, the impact of the scattering theory and of attenuation in the radar operator are investigated, while for beam propagation the 4/3 Earth radius model is employed in all the experiments since some preliminary tests have shown that the use of more accurate models implemented in EMVORADO has not a significant impact. First, in Section 7.1, reflectivity distributions obtained by applying different EMVORADO configurations to the same model fields are compared. Then, the different configurations of the operator are employed in the data assimilation scheme and the results are discussed in Section 7.2. Finally, an

analysis of computational costs is provided in Section 7.3.

## 7.1 Reflectivity distributions

To evaluate the sensitivity of reflectivity simulation to the specifics of the radar operator, three configurations of EMVORADO have been considered:

- *Ray* in which Rayleigh's scattering theory is employed;
- *Mie* in which Mie's scattering theory is employed;
- *Mie_att* in which Mie's scattering theory is employed and attenuation along the beam is taken into account.

Note that attenuation can not be accounted for when employing the Rayleigh's scattering theory.

To quantify the differences between reflectivities simulated with these three different EMVORADO configurations, an assimilation experiment referred to as *conv* has been performed over the three case studies in 2018, i.e. *sept2018*, *oct2018* and *nov2018* (see Section 6.2.2). In this experiment only conventional observations are assimilated and cycles of 60 minutes are employed. The EMVORADO operator is then applied to the obtained analyses in order to simulate equivalent reflectivity volumes for all radars depicted as a solid line in Figure 4.4. In other words, the operator is applied off-line, that is separately from the assimilation procedure.

The overall reflectivity distributions obtained by applying the three configurations of EMVORADO to all the analyses of the *conv* experiment run over the 3 periods in 2018 are represented with box plots in Figure 7.1. In computing box plots, only reflectivities greater than 0 dBZ are considered. In addition to simulated values, the observed ones are also shown (grey box). This is done to give an idea of the actual distribution of reflectivities, but it has to be bore in mind that simulated values have not to be as the observed ones since the agreement between the two fields depends on the analysis accuracy. Therefore, only differences between *Ray*, *Mie* and *Mie_att* distributions have to be considered.

Considering the different configurations of EMVORADO, the use of *Mie* configuration (orange) produces a distribution with higher reflectivity values than that

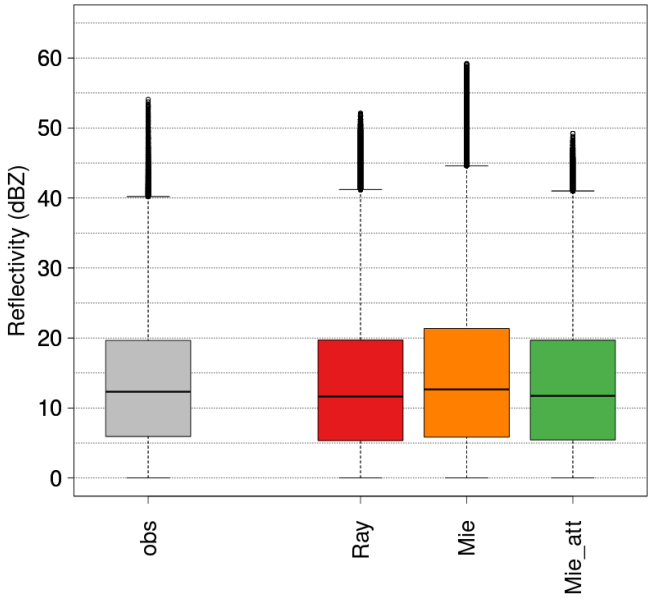


**Figure 7.1.** Reflectivity distributions represented with box plots for observations (grey) and for *Ray* (red), *Mie* (orange) and *Mie_att* (green) configurations of the EMVORADO operator. The distributions are obtained from hourly analyses of *conv* experiment run over *sept2018*, *oct2018* and *nov2018* periods. Each coloured box represents the interquartile range of the reflectivity distribution and the horizontal black line inside the box is the median. The vertical dashed line depicts $5^{th}$ and $95^{th}$ percentile; the former is equal to 0 dBZ for all the experiments by construction (only values greater than 0 dBZ are considered). Black dots represent values above the $95^{th}$ percentile.

of *Ray* (red) for both the interquartile range and maxima. In Section 4.2 it was reported that for large particles (except rain) the Mie scattering scheme results in lower reflectivities than the Rayleigh approximation, but for melting particles the Mie solution usually produces higher reflectivities. Accordingly, the results reported here show that the effect of the melting particles is predominant on that of large particles, at least in the considered case studies. Distributions obtained with *Ray* and *Mie_att* (green) configurations are very close among each others, meaning that the taking into account of attenuation compensates the increase in reflectivity values associated to Mie's scattering. Note that, with the *Mie_att* configuration, maximum values do not exceed 50 dBZ.

An example of how simulated reflectivities vary depending on the EMVORADO configuration is provided in Figure 7.2. For the lowest elevation of the radar located in Armidda (Sardinia region), the observed reflectivity for 9 October 2018

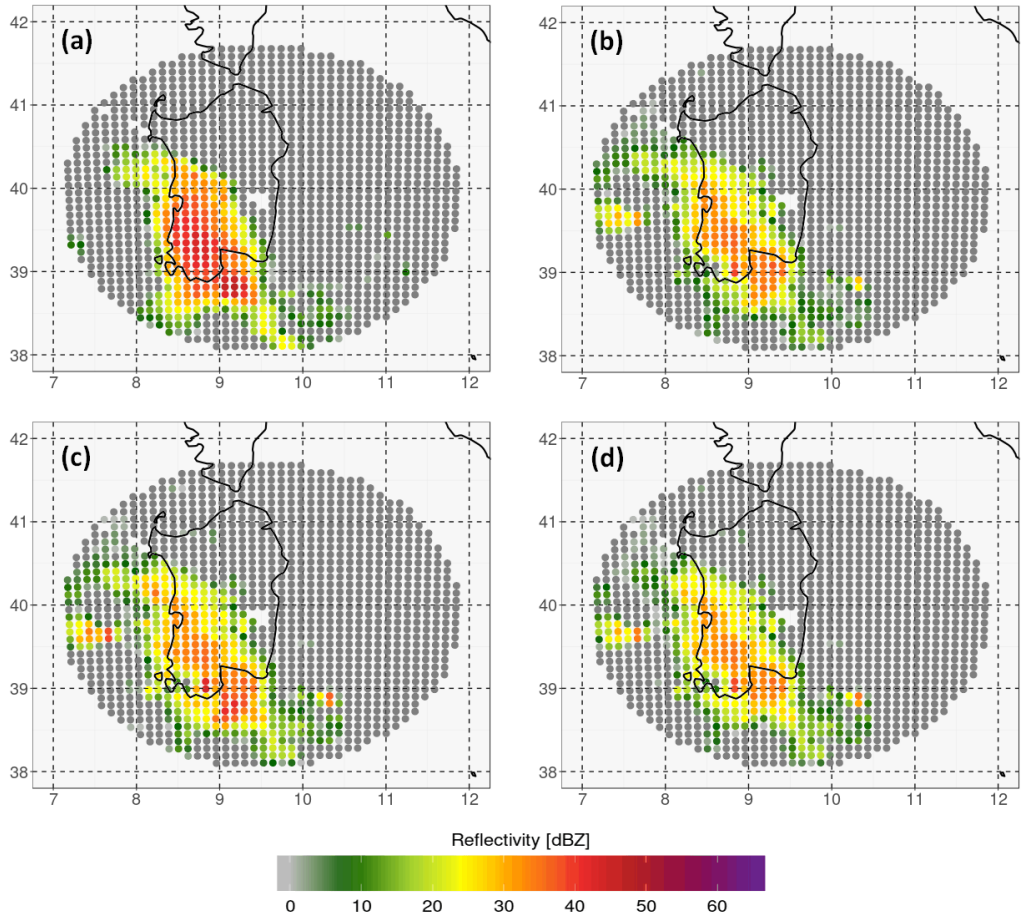


**Figure 7.2.** Observed (a) and simulated reflectivity using *Ray* (b), *Mie* (c) and *Mie_att* (d) configurations for the lowest elevation of the Armidda radar on 9 October at 09 UTC.

at 09 UTC is shown in panel (a) and the simulated reflectivities from the corresponding analysis of *conv* experiment using *Ray*, *Mie* and *Mie_att* configurations are reported, respectively, in panels (b), (c) and (d). Again, the observed field is shown just to give an idea of the actual conditions, but only differences between the three EMVORADO configurations have to be considered. Comparing *Mie* with *Mie_att*, it is possible to evaluate how attenuation modifies the reflectivity field. The reduction on simulated values comparing *Mie_att* to *Mie* is particularly remarkable at approximately 38.7° N 9.2° E and at 40.3° N 7.7° E. Note that, in both cases, strong precipitations are present between the observed reflectivity and the radar station (39.8° N 9.5° E). Similar differences can be observed when comparing *Mie_att* to *Ray*. However, the highest values of *Ray* configuration are

smaller than those of *Mie*.

## 7.2 Assimilation experiments

The three configurations of the EMVORADO operator, i.e. *Ray*, *Mie* and *Mie_att*, are employed in the data assimilation procedure to evaluate their impact on QPF accuracy. The corresponding experiments are referred to as *oper_Ray*, *oper_Mie* and *oper_Mie_att* and they are performed over *sept2018* and *oct2018* periods. The set-up of all these experiments is described in Section 6.2.2; the only difference among them is the configuration of the EMVORADO operator employed to simulate background equivalent reflectivities.

Results of QPF verification in terms of FSS are illustrated in Figure 7.3, taking together *sept2018* and *oct2018* periods. When attenuation is not accounted for, the use of Mie scattering theory worsens QPF accuracy compared to the use of Rayleigh scattering, especially during the first 3 hours of forecast. By taking into account attenuation, FSS scores obtained with Mie scattering are significantly improved in the first 5 hours of forecast. Moreover, *oper_Mie_att* slightly outperforms also *oper_Ray*, in particular at lead times +4h and +5h.

According to the results obtained, attenuation has to be taken into account in the simulation of background equivalents of reflectivity observations. However, this is an unexpected conclusion. In fact, observed reflectivity volumes are already corrected for attenuation and, therefore, this correction should not be employed in the radar operator. Accordingly, *oper_Mie* experiment should provide the best results since it employs the most accurate scattering theory and it does not correct simulated reflectivities for attenuation.

A possible explanation for the unexpected result is that a compensation of errors arises when taking into account attenuation in the radar operator. The error may be associated to the correction for attenuation done in observed reflectivity volumes. In fact, it is important to stress that this is not an easy task and large errors may arise when dealing with high values of reflectivity due to strong precipitations or melting hydrometeors. However, it is not possible to exclude that the compensated errors are linked to other sources of uncertainty in radar measurement or simulation. In this regards, a bias estimation and correction would be

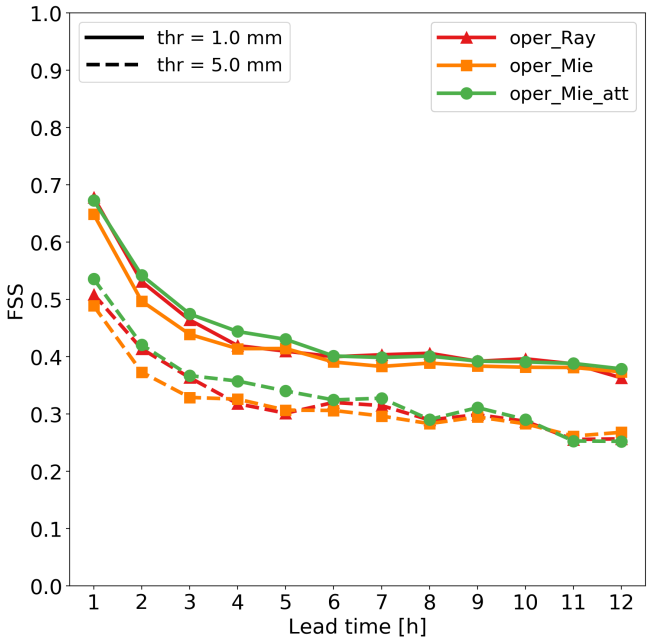


**Figure 7.3.** FSS verification as described in Section 5.2.2 for *oper_Ray* (red lines), *oper_Mie* (orange) and *oper_Mie_att* (green) experiments. The verification is applied to *sept2018* and *oct2018* periods taken together.

desirable but it is very difficult to achieve since biases are likely to be dependent on many factors including weather regimes. It is not by chance that there is no a method in the literature for dealing with it. Anyway, even if this aspect needs a further investigation, simulated reflectivities have to be corrected for attenuation in the set-up employed here since this leads to an improvement in QPF accuracy.

## 7.3 Computational aspects

The use of different EMVORADO configurations impacts on the computational time necessary to run the COSMO model for each member of the KENDA ensemble. In fact, the radar operator (as any other observation operator) is applied during the integration of the model at each time step in which observations are available.

The experiments described in this work are run on Galileo High Performance Cluster of CINECA, the Italian inter-Universities consortium for automatic com-

puting. Regarding COSMO runs, they are performed employing 128 processors over 4 nodes (32 processors per node). For each of the experiments described in this chapter, the approximate computational time to run the COSMO model for one member of the KENDA ensemble is:

- *oper_Ray*: $(7.3 \pm 0.3)$ min;
- *oper_Mie*: $(8.6 \pm 0.5)$ min;
- *oper_Mie_att*: $(8.7 \pm 0.5)$ min;

Therefore, the increase in computational time when employing Mi scattering theory instead of Rayleigh one is about 18 % while the taking into account of attenuation does not affect significantly the computational cost.

In conclusion, the slight increase on computational costs associated to *oper_Mie_att* is affordable for ARPAE computational resources and it is justified by the improvement in QPF accuracy compared to *oper_Ray* experiment. Therefore, *oper_Mie_att* set-up seems to be the best one to assimilate radar reflectivity volumes in the ARPAE framework.

# Chapter 8

# Long term comparison between LHN and assimilation of reflectivity volumes

According to the results obtained in the previous chapters, the best set-up found in this study to assimilate reflectivity volumes is that defined by *oper_Mie_att* experiment. Hereafter, this set-up will be denoted as *conv+refl* and its main features are the following:

- assimilation cycles are of 60 minutes;
- all conventional observations (described in Section 5.1.1) collected during each assimilation cycle are assimilated;
- for each radar station (solid circles in Figure 4.4 which is reported here for convenience and referred to as Figure 8.1), only the volume closest to the analysis time is assimilated, based on the conclusions of the investigation performed in Chapter 5;
- the observation error is equal to 10 dBZ for all reflectivities, based on the conclusions of the investigation performed in Chapter 6;
- the computation of background equivalent reflectivities is performed by the EMVORADO operator employing Mie scattering theory and taking into ac-

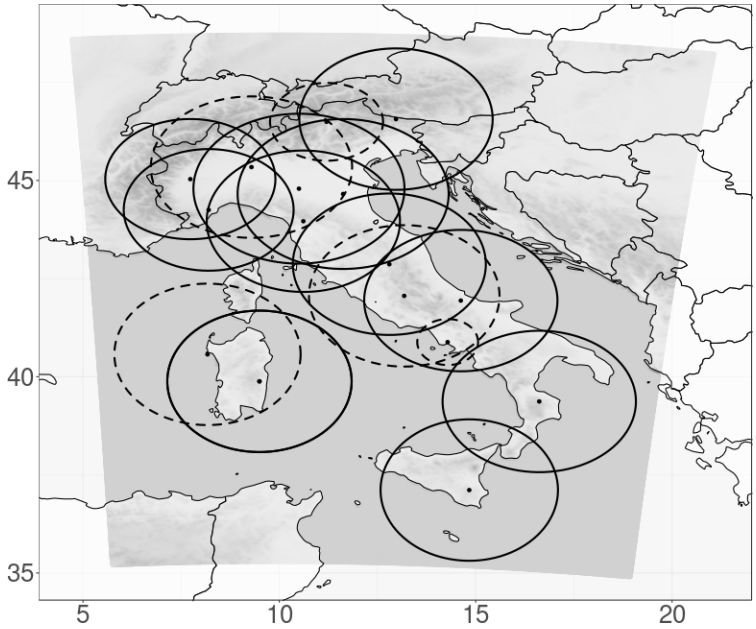


**Figure 8.1.** Same as Figure 4.4, reported here for convenience. Italian radar network overlapped to the integration domain of COSMO-2I (grey-scale). For each radar, the approximate coverage area is shown with a dashed line if the radar system contributes only to generate SRI composite employed in LHN and with a solid line if it is used also to directly assimilate reflectivity volumes through KENDA.

count attenuation, based on the conclusions of the investigation performed in Chapter 7;.

In this chapter, *conv+refl* experiment is compared to *conv+LHN*, which substantially replicates the operational set-up employed at ARPAE. The only difference between the two experiments regards the assimilation of radar data. In *conv+refl*, reflectivity volumes are assimilated as described above. In *conv+LHN*, SRI fields generated from the Italian radar network (both dashed and solid circles in Figure 8.1) are assimilated through LHN. Therefore, the comparison between the two experiments allows to evaluate if the assimilation of reflectivity volumes with the set-up identified in this study can improve analyses and forecasts accuracy compared to that obtained through LHN.

These two experiments are run over *sept2018*, *oct2018* and *nov2018* periods, described in Section 6.2.2. As can be observed in Figure 8.1, radar stations employed for the assimilation of reflectivity volumes do not coincide with those employed to derive SRI fields for LHN. The fairness of the comparison between the two exper-

iments is discussed in Section 8.1. Then, QPF accuracy is evaluated in terms of FSS and dichotomous scores in Section 8.2. Finally, verification of upper-air and surface atmospheric variables is performed and the obtained results are discussed in Section 8.3.

## 8.1 Accounting for inhomogeneity between radar datasets

In the comparison between *conv+refl* and *conv+LHN* experiments, the reflectivity volumes of five of the radars employed to derive SRI fields were not available to be directly assimilated; these five radars are depicted with a dashed circle in Figure 8.1. Accordingly, it can be argued that the results provided in this chapter do not show a fair comparison between LHN and the assimilation of reflectivity volumes.

However, it has to be observed that the areal coverage of the two datasets is very similar. Some differences can be observed over the sea or neighbouring countries but these regions are small compared to the whole radar network domain. Furthermore, in terms of QPF verification (Section 8.2), these regions are not considered since the verification domain is only the mainland of Italy. Regarding upper-air and surface variables, as will be described in Section 8.3, verification is performed over the whole COSMO-2I integration domain. Therefore, in this case, *conv+LHN* may be slightly advantaged compared to *conv+refl*, but the small difference in terms of areal coverage between the two radar datasets should ensure a very small impact.

Another problem associated to the inhomogeneity of the two radar datasets is that there are some cases in which data from a radar station are available to derive the SRI field but the reflectivity volume from the same or a close radar station is not available to be assimilated directly. The most relevant example among these few cases regards Sardinia region during *nov2018* period. For several days the radar located in Armidda (solid circle centered at 39.8°N 9.5°E) was not available neither for reflectivity assimilation nor to derive SRI fields. However, the close radar located in Capo Caccia (dashed circle centered at 40.6°N 8.2°E) was available for determining SRI fields. In these cases, performing verification over

Sardinia would clearly advantages *conv+LHN* experiment compared to *conv+refl* since in the latter no radar data are assimilated. To mitigate this problem, for forecasts initialized from analyses affected by this issue, the verification domain is restricted to exclude regions in which such discrepancies between radar datasets are observed (like Sardinia in the above example). This restriction of the verification domain is applied to both experiments.

Overall, inhomogeneities between the radar datasets employed for reflectivity assimilation and for generating SRI fields are small and in large part addressed by the way in which verification is performed. Therefore, the comparison between *conv+refl* and *conv+LHN* can be regarded as a fair comparison between assimilation of reflectivity volumes and LHN, even if it should be considered that *conv+LHN* is likely to be (very) slightly advantaged in our verification scores.

## 8.2 QPF verification

### 8.2.1 FSS

Verification of forecast precipitation in terms of FSS is performed as in the previous chapters and described in Section 5.2.2. Note that, according to Section 8.1, for some forecasts the verification domain may be restricted compared to that of Figure 5.2. Results are provided in Figure 8.2 considering, in the left panel, *sept2018* and *oct2018* together and, in the right panel, *nov2018* period. This choice reflects the different main precipitation kind observed in each period: in *sept2018* and *oct2018* precipitations are mainly convective while in *nov2018* mainly stratiform.

In order to assess the uncertainty on FSS values, here scores are provided with the 95% level of confidence (vertical bars) estimated through the bootstrap method (Efron and Tibshirani, 1994). From the original dataset of pairs of observed and forecast precipitation fractions, samples are drawn with replacement in order to create a new dataset with the same size of the original one. This operation is repeated several times obtaining a set of new datasets referred to as bootstrap resamples. Then, FSS is calculated for each bootstrap resample and percentiles of scores are used to estimate the uncertainty. In this study, 5000 bootstrap resamples are employed to estimate the 95% level of confidence for each FSS value.

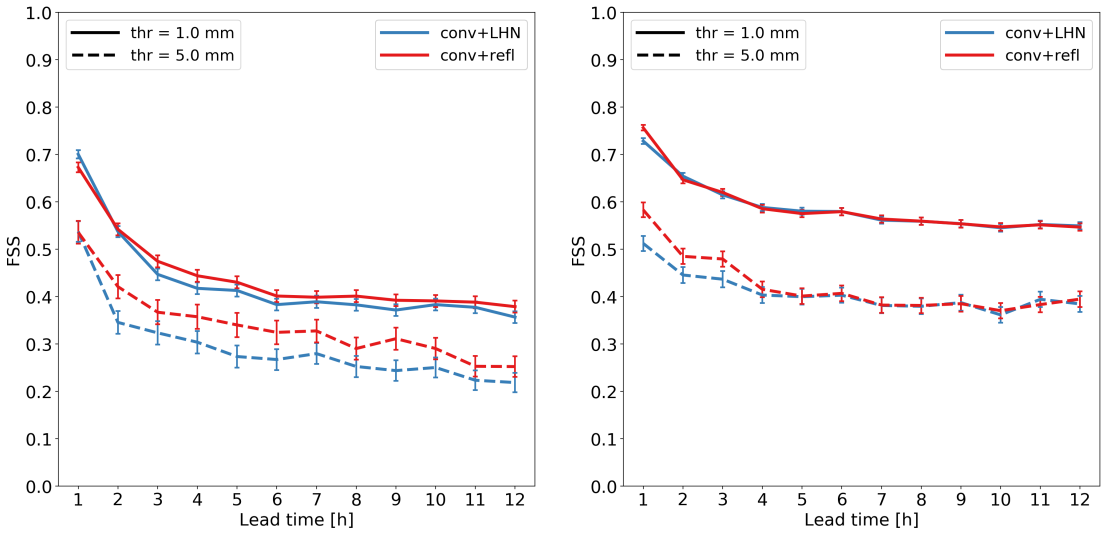


**Figure 8.2.** FSS verification as described in Section 5.2.2 for *conv+LHN* (blue) and *conv+refl* (red) experiments. In the left panel, scores are shown for *sept2018* and *oct2018* periods considered together while in the right panel for *nov2018* period. Vertical bars indicate 95% levels of confidence.

Considering *set2018* and *oct2018*, FSS scores are obtained employing 179 forecasts for each experiment. At lead time +1h, *conv+LHN* outperforms *conv+refl* when considering the 1 mm threshold and the improvement is statistically significant. However, no improvement can be observed for the 5 mm threshold. From the second to the last hour of forecast, FSS scores of *conv+refl* are higher than those of *conv+LHN* for both thresholds. Regarding the 1 mm threshold, the improvement is statistically significant only at +3h and +4h, while for the 5 mm threshold most of differences among the two experiments are large and statistically significant.

QPF verification over *nov2018* period consists of 124 forecast. At lead time +1h, a strong and statistically significant improvement can be observed comparing *conv+refl* to *con+LHN* at both thresholds. Considering the 1 mm threshold, the improvement is already lost at the second hour of forecast and the scores of the two experiments are very close until the end of the forecast range. However, a statically significant improvement can still be noticed for the 5 mm threshold at lead time +2h and +3h and a small (but not significant) improvement also at +4h.

Overall, the assimilation of reflectivity volumes improves QPF accuracy compared to the assimilation of SRI fields via LHN in all periods considered. However,

the positive impact is much stronger in *sept2018* and *oct2018* periods (up to the end of the forecast) than in *nov2018* period (up to +3h/+4h). This difference is likely to be linked to the different weather regime. In fact, as shown in Craig et al. (2012) and in Davolio et al. (2017), the impact of assimilation is constrained by the environment characteristics, defined in terms of the presence of convective equilibrium (Emanuel, 1994). Convection is said to be in equilibrium with the large-scale forcing if it consumes convective available potential energy (CAPE) at the same rate with which CAPE is generated by the large-scale forcing. In these conditions, convection is mainly determined by the large-scale flow and predictability is high (Keil et al., 2014). When synoptic forcing is weak and there is a strong inhibition in CAPE release, convection is said to be in non-equilibrium with the large-scale flow. In this case, CAPE accumulates and the development of precipitations is determined by local triggers capable to overcome the inhibition and to consume CAPE; accordingly, predictability is low (Keil et al., 2014). Regarding data assimilation, its positive impact in non-equilibrium conditions is generally strong since assimilation allows to improve the timing and location of triggers. On the other hand, in equilibrium conditions, the effect of the assimilation procedure is rapidly removed by the large scale forcing and, consequently, its positive impact is very short in time.

Even if it has not been verified, for example by computing the convective time scale (Done et al., 2006), meteorological conditions associated to the 3 periods in 2018 (see Section 6.2.2) suggest that convective equilibrium should be present in *nov2018* while non-equilibrium should be associated to *sept2018* and *oct2018*. A clue that reinforces this hypothesis is that predictability for *nov2018* is higher than that for the other two periods as demonstrated by the higher values of FSS. If this hypothesis is correct, results shown here are in agreement with those of Craig et al. (2012) and Davolio et al. (2017). In *sept2018* and *oct2018* periods, the assimilation of reflectivity volumes improves the analyses quality compared to LHN and, due to the strong impact of assimilation in non-equilibrium conditions, this results in a long lasting improvement in QPF accuracy. The improvement in analysis quality is present also in *nov2018* but, in this case, the improvement in QPF accuracy is limited in time because the positive impact of assimilation is rapidly destroyed by the large scale flow.

**Table 8.1.** Contingency table based on binary outcomes of observation and forecast.

| | | Observation | |
|---|---|---|---|
| | | yes | no |
| Forecast | yes | *hits* | *false alarms* |
| | no | *misses* | *correct negatives* |

### 8.2.2 Dichotomous scores

In order to strengthen results obtained via FSS, the QPF accuracy is verified also considering some dichotomous scores computed over hydro-meteorologically homogeneous areas in the Italian mainland and using only rain-gauges as observation dataset, that is observations completely independent from SRI fields assimilated in *conv+LHN* experiment.

#### Scores employed

Dichotomous scores are based on the contingency table which shows the frequency of forecast and observed events (Table 8.1). In case of precipitation, an event is defined as the exceedance of a threshold. Four dichotomous scores are considered here. The frequency bias index (FBI) measures the ratio of the frequency of forecast events to the frequency of observed events:

$$\text{FBI} = \frac{hits + false\ alarms}{hits + misses} \tag{8.1}$$

The score ranges from 0 to infinity and for FBI = 1 the forecast is in perfect agreement to observations in terms of FBI. A value of FBI $< 1$ indicates that the forecast underestimates precipitation while a value of FBI $> 1$ denotes an overestimation. It only measures relative frequency, not how the forecast corresponds to the observations at each point.

The probability of detection (POD) measures the ratio between correctly fore-

cast events and the total of observed events:

$$\text{POD} = \frac{hits}{hits + misses} \tag{8.2}$$

It ranges from 0 to 1 and POD = 1 indicates a perfect forecast in terms of POD. Since it does not account for *false alarms* it has to be employed in combination with an other verification score. For example, it can be associated to the success ratio (SR) which measures the ratio between correctly forecast events and the total of forecast events:

$$\text{SR} = \frac{hits}{hits + false\ alarms} \tag{8.3}$$

Also in this case the score can range from 0 to 1 and a perfect agreement between forecast and observations in terms of SR is associated to SR = 1. POD and SR are complementary verification scores since both are sensitive to *hits* but the former does not account for *false alarms* while the latter accounts for *false alarms* but it does not consider *misses*.

Finally, the threat score (TS) measures the the fraction of observed events that were correctly predicted:

$$\text{TS} = \frac{hits}{hits + false\ alarms + misses} \tag{8.4}$$

It ranges from 0 to 1 and TS = 1 indicates a perfect forecast in terms of TS. It does not consider correct negative events and it depends on the climatological frequency of events (poorer scores for rarer events) since some hits can occur purely due to random chance.

Since all the above dichotomous scores have merits and weakness, they have to be considered collectively. A practical way to do this is to exploit the geometric relationship between these four scores in order to construct a performance diagram (Roebber, 2009). In the performance diagram (see for example a panel in Figure 8.4) $x$- and $y$-axis represent, respectively, SR and POD, dashed lines denote FBI and solid labelled lines are TS. For good forecasts, POD, SR, FBI and TS approach unity, such that a perfect forecast lies in the upper right of the diagram. Deviations in a particular direction will indicate relative differences in POD and SR, and consequently in FBI and TS. Thus, an immediate visualization of differences in

performance is obtained.

### Implementation of the verification

As for FSS, dichotomous verification has been performed over the Italian mainland but with two important differences. First of all, in this case, only rain-gauges are employed as observation dataset. The reason behind this choice is that the rain-gauges dataset (hereafter referred to as RG) is completely independent from observations assimilated in the experiments. In fact, it can be argued that observations used for FSS, i.e. fields of precipitation estimated through the Italian radar network corrected by rain-gauges (hereafter, referred to as RAD-RG), may be slightly correlated to SRI fields assimilated via LHN at the beginning of the forecast. This can slightly advantage *conv+LHN* compared to *conv+refl* in terms of verification scores in the very first few hours of forecast. Even if it is not shown here, this has been actually observed comparing results of dichotomous verification obtained employing as observations RG and RAD-RG datasets. As expected, the "advantage" for *conv+LHN* scores is small and limited to the first 2 hours of forecast. Accordingly, previous results obtained via FSS are not invalidated by the use of the RAD-RG dataset but it has to be bore in mind that scores for *conv+LHN* at lead times +1h and +2h are likely to be slightly overestimated. By employing rain-gauges as observations, this (small) problem is solved in the dichotomous verification presented in this section.

Secondly, in dichotomous verification, areas depicted in Figure 8.3 are considered instead of regular boxes. These areas, ranging approximately from 190 to 7400 $km^2$, are defined by DPC for the Italian weather alert system and they are homogeneous with respect to the type and intensity of hydro-meteorological phenomena that may occur and their effects on the territory. To compute scores, for each area the average and maximum of forecast and observed precipitation are considered. Regarding forecast precipitation, it is first interpolated to rain-gauges location. Note that one could choose to compute average and maximum of forecast precipitation employing all model grid points in the selected area. Even if it is not shown, this leads to scores very similar to those presented here regarding average precipitation, but the same does not hold for maxima. In fact, rain-gauges

**Figure 8.3.** Hydro-meteorologically homogeneous areas defined by DPC for the Italian weather alert system and employed here for dichotomous verification.

are much less than model grid points and it is hardly conceivable that they can be representative for maximum precipitation in each area. Finally, according to Section 8.1 and similarly to what done in FSS verification, for some forecasts the verification domain may be restricted compared to that of Figure 8.3.

### Results

For both *conv+refl* and *conv+LHN* experiments, dichotomous verification is performed over *sept2018*, *oct2018* and *nov2018* periods. To summarize results, here all periods are considered together. However, even it is not shown, a behaviour similar to that described in Section 8.2.1 is observed when comparing verification scores obtained over *sept2018* and *oct2018* to those obtained over *nov2018*.

In Figure 8.4, performance diagrams for average precipitation are shown from lead time +1h to +4h. At the first hour of forecast, POD of *conv+LHN* is larger than that of *conv+refl* at all thresholds except 3 mm. However, corresponding values of SR for *conv+LHN* are not as good indicating an overestimation of average precipitation which can be also noticed by the FBI values significantly above 1.

On the other hand, SR of *conv+refl* is much better than that of *conv+LHN* at all thresholds and values are similar to the corresponding of POD. Accordingly, FBI is very close to 1, even if a slight underestimation can be noticed. In terms of TS, which better summarize the QPF accuracy, forecasts obtained by assimilating reflectivity volumes have better scores than those obtained by using LHN at each threshold and a remarkable improvement can be observed for the 3 mm one.

At lead time +2h, the positive bias associated to *conv+LHN* is reduced and the small negative bias of *conv+refl* is slightly enhanced. In terms of TS, the latter experiment has higher scores than the former at each threshold with a large improvement for the 1 mm and 3 mm ones. A similar behaviour can be observed also at +3h and +4h with a tendency for FBI to approach 1 for both experiments. From lead time +5h to +8h (Figure 8.5) differences among the two experiments in terms of verification scores become progressively smaller. However, up to +7h, SR of *conv+refl* is always larger than that of *conv+LHN* (with the exception of 3 mm threshold at +5h) and often the differences are statistically significant. Since corresponding values of POD are close among the two experiments, TS results improved for *conv+refl* at each threshold from +5h to +7h (except for 3 mm at +5h). From lead time +8h onwards (performance diagrams from +9 to +12h are not shown), the positive impact on QPF accuracy associated to assimilating reflectivity volumes instead of performing LHN is substantially lost since verification scores of *conv+refl* and *conv+LHN* become very close.

In Figure 8.6, performance diagrams for maximum precipitation are shown from lead time +1h to +4h. Considering the 5 mm and 10 mm thresholds, at lead time +1h SR values of *conv+refl* are larger than those of *conv+LHN*, while POD values are smaller. In this case, the FBI of the latter experiment is closer to 1 than the former, which underestimates maximum precipitations. However, in terms of TS, *conv+refl* is still better than *conv+LHN*. Same results hold for POD and SR when considering the 20 mm and 30 mm thresholds but, in this case, uncertainties are too large to assess which experiment performs better. A similar behaviour is observed at lead time +2h, even if differences among the two experiments in terms of FBI are smaller and both tend to slightly underestimate maxima. TS for *conv+refl* is significantly higher than that for *conv+LHN* at 5 mm and a smaller improvement can be observed also at 10 mm. However, results are very close for

the 20 mm threshold and worse for the 30 mm threshold. From lead time +3h to +7h (see also Figure 8.7), the improvement of *conv+refl* compared to *conv+LHN* is confirmed for the two lowest thresholds. For the other two thresholds, results are mixed but uncertainties are too large to determine which experiment performs better. Finally, as observed for average precipitation, from lead time +8h onwards scores of *conv+LHN* and *conv+refl* become very close.

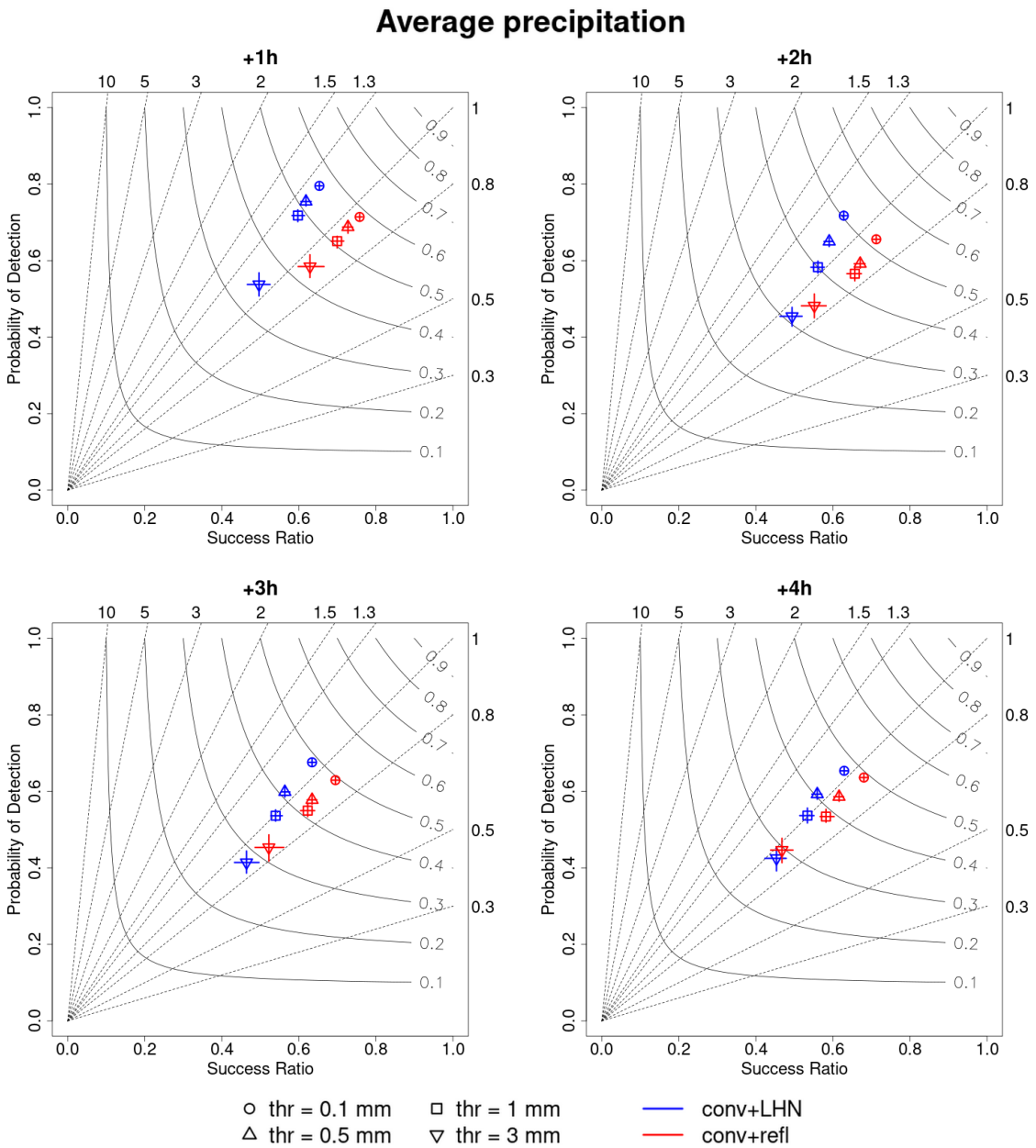


**Figure 8.4.** Performance diagrams for average precipitation at lead times indicated as title of each subplot. Different thresholds (symbols) are considered for experiments *conv+LHN* (blue) and *conv+refl* (red). Dashed lines represent FBI while solid labelled lines are TS. Horizontal and vertical bars associated to each symbol are 95% levels of confidence estimated with bootstrap.

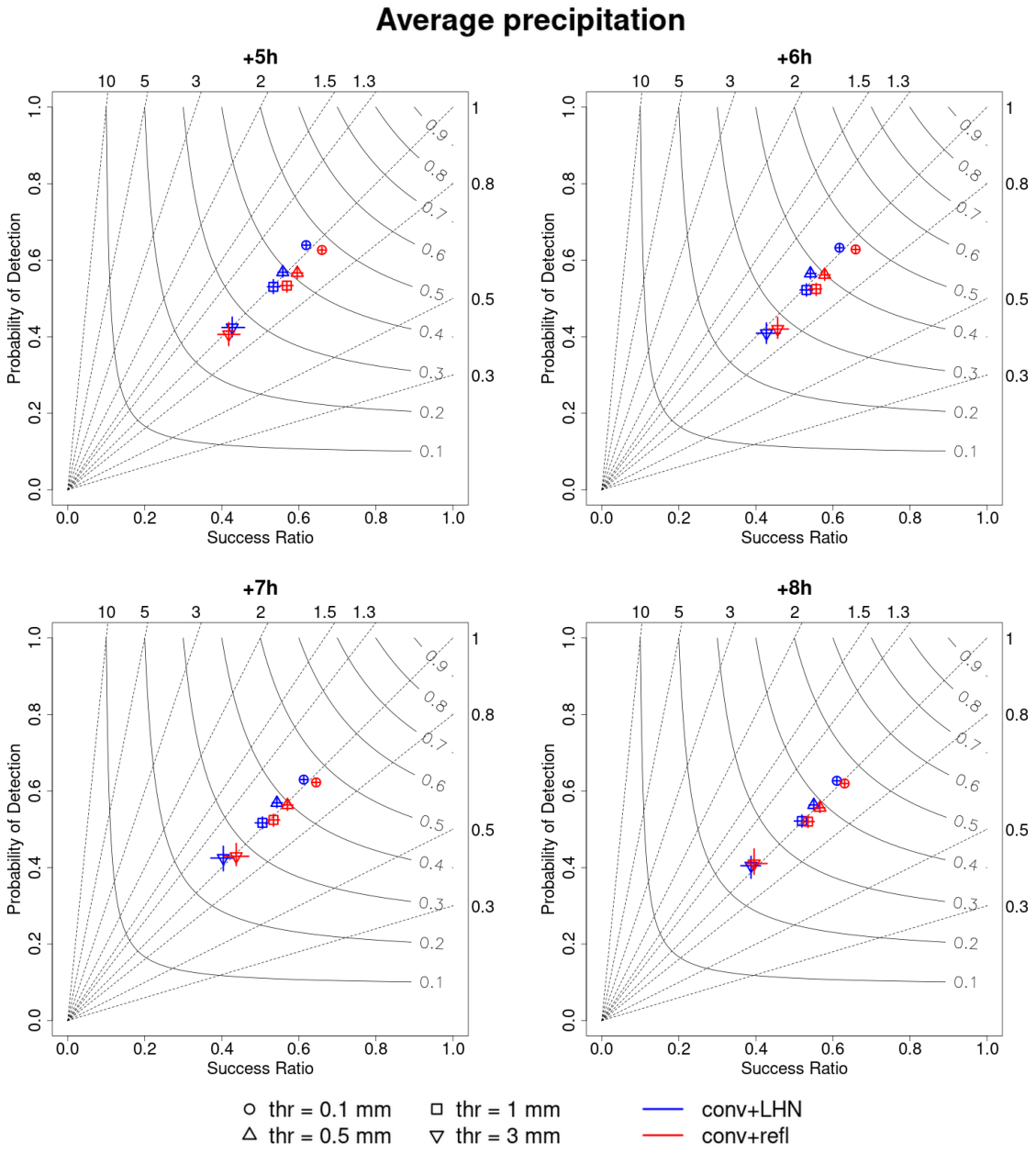


**Figure 8.5.** Same as Figure 8.4 but for lead times from +5h to +8h.

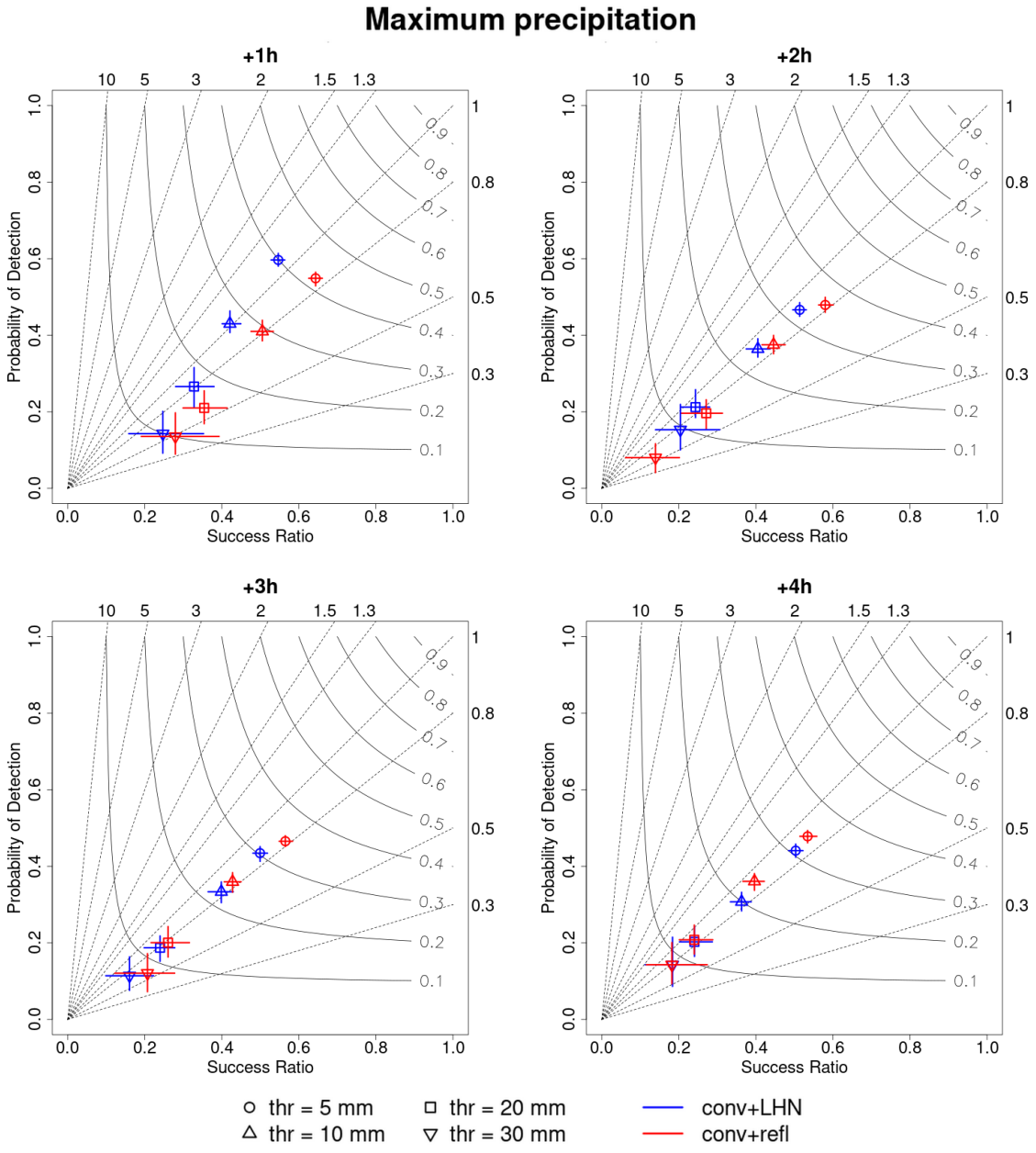


**Figure 8.6.** Same as Figure 8.4 but considering maximum precipitation for lead times from +1h to +4h.

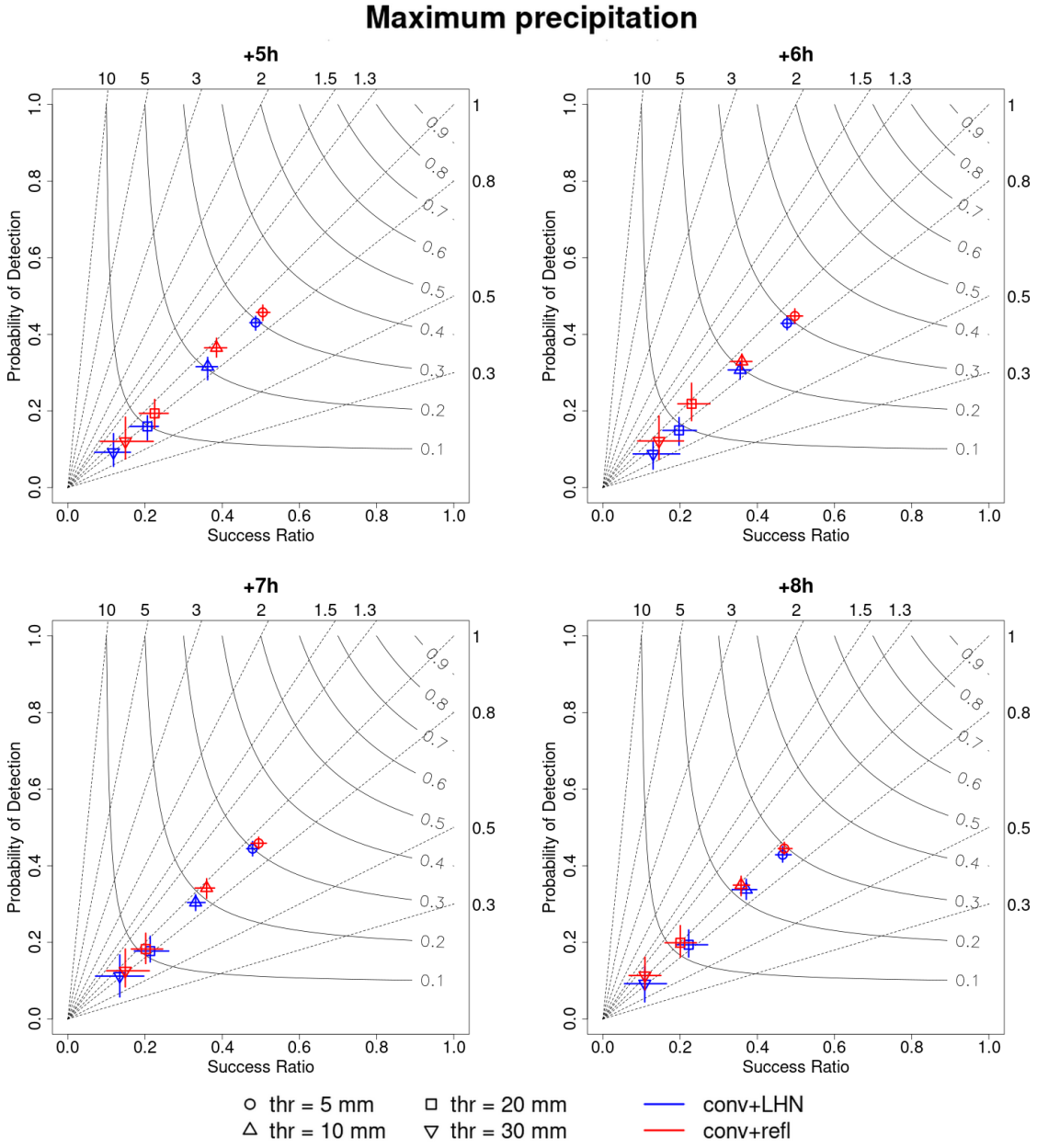


**Figure 8.7.** Same as Figure 8.4 but considering maximum precipitation for lead times from +5h to +8h.

To summarise, dichotomous verification applied to all forecasts (303 in total) shows an improvement in average precipitation accuracy over hydro-meteorologically homogeneous areas up to +7h when assimilating reflectivity volumes instead of performing LHN. The improvement is noticeable at all thresholds considered (0.1, 0.5, 1 and 3) and larger for the highest one. Same results hold when considering maximum precipitation and employing the 5 and 10 mm thresholds. For the highest thresholds (20 and 30 mm), the number of events is insufficient to draw conclusions. Despite the improvement, the assimilation of reflectivity volumes leads to a slight underestimation of average and maximum precipitation in the first 3/4 hours of forecast. A possible cause of this behaviour may be attributed to the 5 dBZ threshold applied to reflectivities before performing assimilation. In fact, due to this, if the background equivalent of all members of the ensemble is equal to 5 dBZ, no observation is assimilated. In other words, if precipitation is observed but not forecast by any member of the ensemble, it is not possible to correct the background state assimilating only reflectivity data. Since the use of a threshold is essential, this possible issue needs to be further investigated.

## 8.3 Upper-air and surface variables verification

Comparison between *conv+LHN* and *conv+refl* set-ups is performed also by verifying upper-air and surface atmospheric variables. Among upper-air variables, temperature and wind velocity from AIREP and relative humidity from TEMP are considered. Regarding the type of observations, the number of AIREP measurements is much higher than the TEMP ones and they have a greater spatial and temporal coverage; unfortunately, most AIREP measurements do not include relative humidity. Among surface variables, 2-meter temperature, 2-meter relative humidity, 10-meter horizontal components of wind velocity and surface pressure from SYNOP are examined.

### 8.3.1 Upper-air variables

Pairs of observation and corresponding forecast values are aggregated according to their geographical and vertical position and according to lead time of forecast

values. Regarding spatial aggregation, the model integration domain is divided into atmospheric volumes. This is achieved by defining some vertical layers and then dividing each one in horizontal squared boxes with a 2° side. For AIREP measurements vertical layers have a 2 km thickness while for TEMP measurements vertical levels are defined in pressure coordinate with variable distances among each other in order to obtain an approximate homogeneous filling of observations in the vertical. The temporal aggregation is performed defining lead time intervals of 3 hours centered at +3h, +6h and +9h; in addition, also the 1.5h intervals from analysis time to +1.5h and from +10.5 to +12h are considered.

Given a verification variable, for each time interval and for each atmospheric volume, i.e. each box in each vertical layer, bias and root mean square error (RMSE) are computed, provided that the sample consists of at least 100 pairs of observation and forecast value. Then, the average of bias and RMSE values over all atmospheric volumes is computed for each vertical layer at each forecast time interval. In this way, a unique value of bias and RMSE is obtained for each atmospheric layer and each time interval taking into account the inhomogeneity of observations datasets: each region has the same weight, independently from its observation density. Note that, according to Section 8.1, for some forecasts part of the model domain may be excluded from verification.

In Figure 8.8, the difference between RMSE of *conv+LHN* and of *conv+refl* for each atmospheric layer and each time interval is shown. Positive (green) values indicate an improvement in forecast accuracy when assimilating reflectivity volumes instead of performing LHN. Regarding temperature, a neutral or slightly positive impact in assimilating reflectivities can be observed up to +4.5h at each level but then the impact is lost. A more significant improvement can be noticed in wind speed over the whole forecast time range, with the only exception for the atmospheric layer between 3 and 5 km considering observations collected from analysis time to +1.5h. Similarly, a consistent improvement is observed for relative humidity with the positive impact which weakens with lead time. The improvement is stronger at mid and high levels, with the exception of the layer between 400 hPa and 600 hPa in the first time interval.

In Figure 8.9, the difference between the absolute value of bias of *conv+LHN* and of *conv+refl* is reported. This only indicates if *conv+refl* is closer to 0 com-

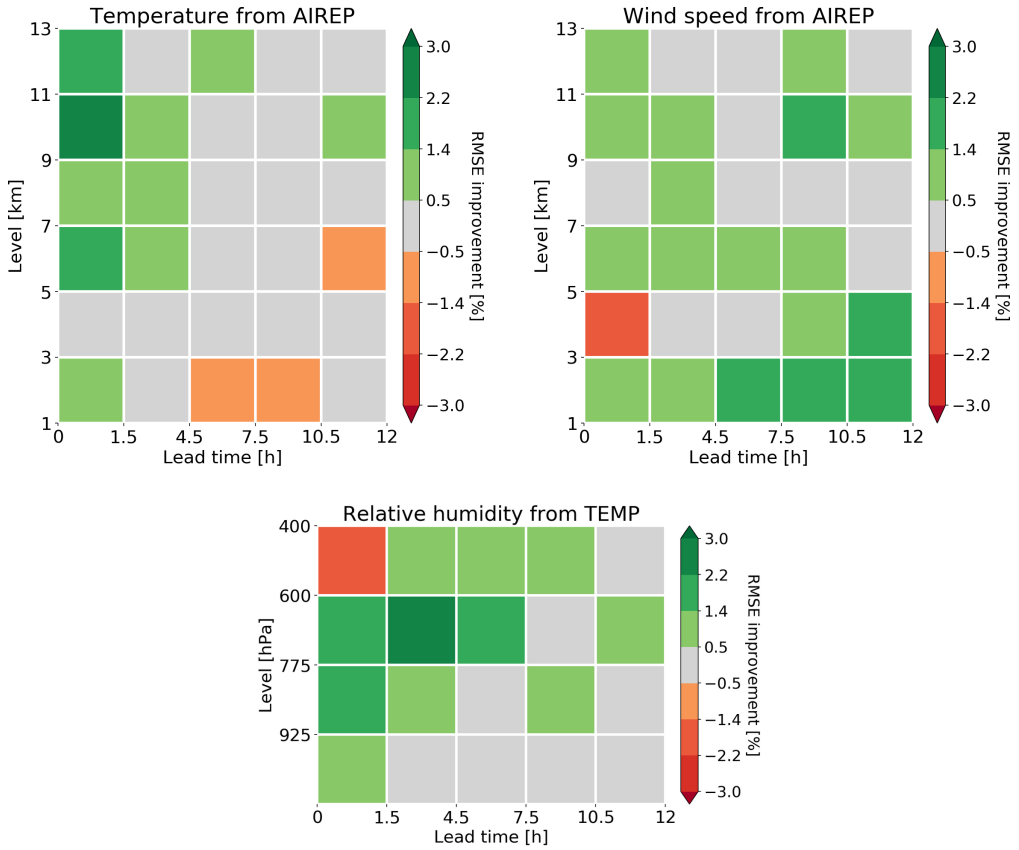


**Figure 8.8.** Difference (in percentage) between RMSE of *conv+LHN* and of *conv+refl* for the variable indicated as title of each subplot. For each coloured square, values on the $y$-axis indicate the vertical levels which define the corresponding layers while values on the $x$-axis the lead times which define the forecast intervals.

pared to *conv+LHN* without giving any information about the bias sign. In this case, values are reported in terms of units of the corresponding variable since some biases are close to 0 and the percentage difference may be misleading. Regarding temperature and wind velocity, the assimilation of reflectivity volumes has no impact in terms of bias, even if a very slight worsening can be observed for temperature between 1 and 3 km up to +7.5h. However, a slight but consistent improvement can be observed in relative humidity from 925 hPa to 600 hPa over the whole forecast range.

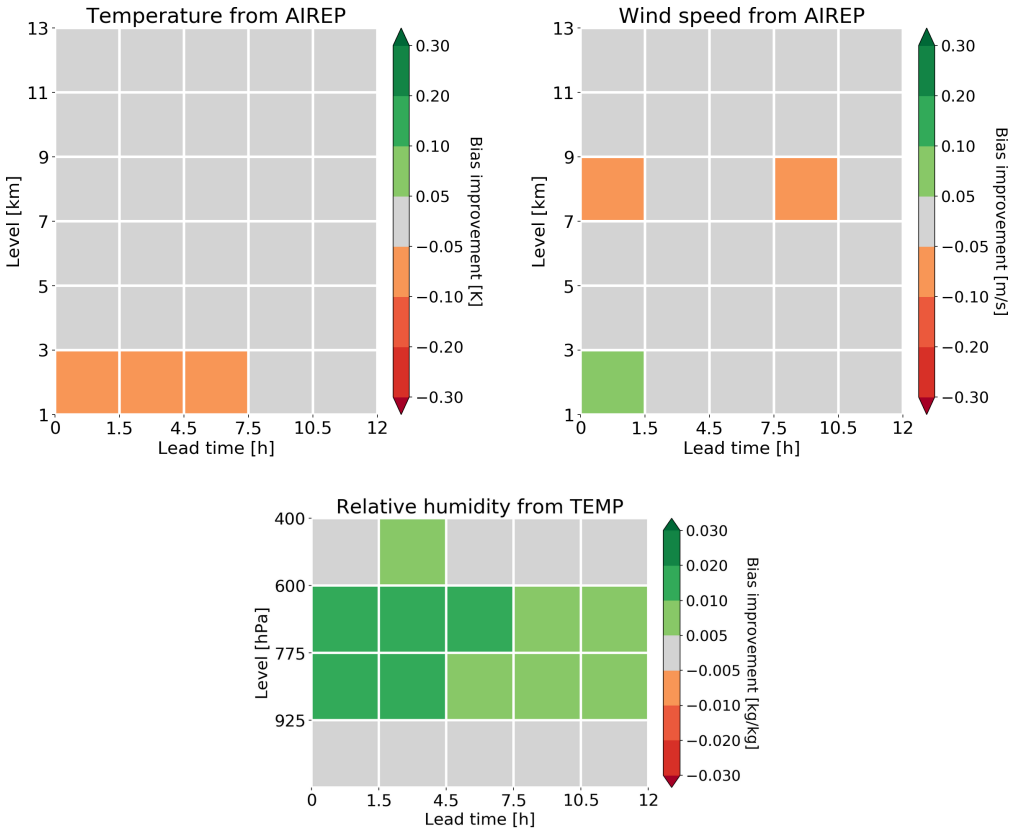


**Figure 8.9.** Same as Figure 8.8 but for the difference (in units of the corresponding variable) between the absolute value of bias of *conv+LHN* and of *conv+refl*.

### 8.3.2 Surface variables

A procedure similar to that described for upper-air verification is employed to perform surface variables verification. In this case, the spatial aggregation of observations is performed only horizontally since all measurements are at the same level for each variable. Furthermore, since SYNOP observations have a hourly time resolution, it is not necessary to aggregate them in time and, therefore, scores are computed each hour starting from the analysis time.

Bias and RMSE for *conv+LHN* and *conv+refl* experiments are shown in Figure 8.10. In terms of 2-meter temperature, the assimilation of reflectivity volumes slightly reduces RMSE compared to LHN at analysis time and in the first 5/6 hours of forecast. A more significant improvement can be observed for bias, which holds for the whole forecast range. Regarding 2-meter relative humidity, the impact

of assimilating reflectivities is neutral in terms of RMSE and slightly negative in terms of bias. In fact, the negative bias associated to *conv+LHN* is enhanced in *conv+refl* both at analysis time and during the whole forecast. A substantially neutral impact can be observed when considering the horizontal components of 10-meters wind velocity, except for a slight worsening in bias for the meridional component. Note that the reduction in bias and RMSE for both experiments each 3 hours from lead time +3h is due to the presence of SYNOP stations which time resolution is 3 hours instead of 1 hour. Finally, both RMSE and bias of *conv+refl* are slightly larger than those of *conv+LHN* during forecast.

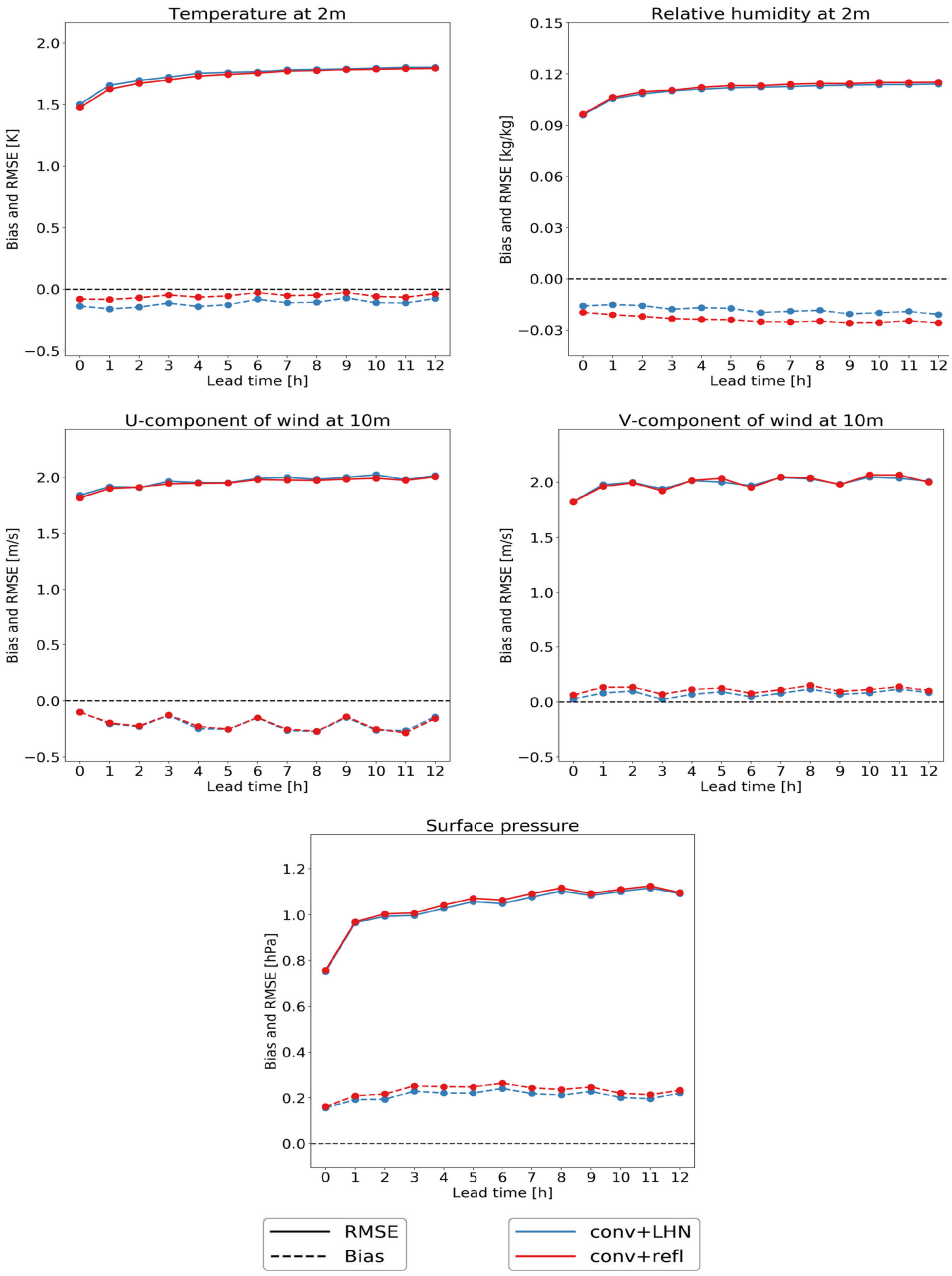


**Figure 8.10.** Bias (dashed lines) and RMSE (solid lines) for the variable indicated as title of each subplot for *conv+LHN* (blue) and *conv+refl* (red) experiments.

# Chapter 9

# Conclusion

The aim of this study, as stated in the Introduction, was:

*to investigate the critical aspects of assimilating in a local meteorological model radar reflectivity volumes using an ensemble Kalman filter scheme and to identify a suitable configuration which can be employed in an operational framework.*

For this purpose, 11 C-band radars of the Italian network have been employed to assimilate reflectivity volumes into the convection-permitting NWP model COSMO-2I, which is run operationally at ARPAE to provide high resolution weather forecasts for Italy. Reflectivity volumes from these radars, which have been provided to us in the native spherical coordinates, have been assimilated using a LETKF scheme, implemented for the COSMO model through the KENDA system. The EMVORADO operator has been employed to simulate equivalent radar reflectivities from the prognostic variables of the model. In all the experiments discussed in this study, the assimilation of radar volumes has been performed in combination to the assimilation of conventional observations (AIREP, SYNOP, and TEMP). This choice is consistent with what would be done in an operational framework, since it allows to exploit all available information on the state of the atmosphere.

The specific objectives stated in the Introduction to achieve the aim of this work are reported in the following, together with the results obtained.

**1) To evaluate the impact of employing different assimilation window lengths or subsets of observations and to investigate the consequent arise of imbalances**

This aim is addressed in Chapter 5. When the length of the assimilation window coincides with the length of the assimilation cycle, that is all observations collected during the forward integration of the model are assimilated, the use of cycles shorter than 60 minutes negatively affects QPF accuracy. This is due to the inability of the model to remove the spurious gravity waves which arise at each analysis step. In fact, if assimilation cycles are of 15 or 30 minutes, the forward integration of the model from one analysis to the next is too short to suppress such imbalances. Consequently, the presence of these spurious gravity waves undermines the analyses quality which, in turns, worsen forecasts accuracy.

On the other hand, the use of an assimilation window which is shorter than the length of the cycle, i.e. the assimilation of a subset of observations including the closest to the analysis time, leads to a slight improvement in QPF accuracy. In particular, employing 60 minutes cycles, it results advantageous to assimilate, for each radar, only the closest volume to the analysis time, while for conventional data, which have greater localization length scales than reflectivities, all observations collected during each cycle can be assimilated. It is worth noting that this configuration is associated to a reduction of computational costs since less reflectivity volumes are employed.

**2) To estimate the reflectivity observation error and its impact on the data assimilation system**

This topic is discussed in Chapter 6. An estimation of the reflectivity observation error (*roe*), based on Desroziers et al. (2005) diagnostics, is provided as a function of the distance of observations from the radar station. As far as the author knows, this kind of estimation has never been performed before for reflectivity volumes.

As a general behaviour, *roe* increases with horizontal distance while it decreases with vertical distance up to 4-6 km and then stabilizes. The former trend is likely to be associated to the increase with distance of the observed air volume size which leads to a more probable violation of some assumptions of the radar measurement,

like the uniform filling of the volume and the single scattering hypothesis. In addition, errors due to the correction for attenuation are likely to increase. The vertical trend can be explained by the fact that radar measurements are more prone to errors at low altitude, in particular in terms of clutter. In this regards, it is important to bear in mind that it is not guaranteed that the quality control procedure completely removes all measurement errors before the assimilation of observations. The general behaviour observed here is substantially confirmed when considering single radar stations and different periods to compute the estimation. Nevertheless, estimated values of *roe* can vary significantly.

Despite *roe* varies markedly with radar station, with distance of observations from radar and with meteorological conditions (i.e. period considered for the estimation), employing this more complex characterization of *roe* in the data assimilation procedure instead of a unique value for all reflectivities does not improve QPF accuracy. This is likely due to a combination of two reasons: the size of the sample employed for the estimation, which may be not large enough, and the fact that error correlations between pairs of observations are not taken into account, since a diagonal $\mathbf{R}$ matrix is employed. In fact, as estimated in Section 6.4, a significant error correlation characterizes all pairs of observations which respective horizontal distance is up to 38 km and the vertical one is up to 10 km. Accordingly, the use of a diagonal $\mathbf{R}$ matrix, as done in this work and in most data assimilation systems, partly invalidates the use of estimated values of *roe* in the data assimilation procedure. Moreover, the error correlations raise serious doubts about the effectiveness of using a diagonal $\mathbf{R}$ matrix.

**3) To investigate how different configurations of the radar operator affect the simulation of equivalent reflectivities and their consequent impact on the assimilation procedure**

This subject is covered in Chapter 7. The simulation of equivalent reflectivity volumes from prognostic model variables using Mie scattering theory provides higher values than those obtained employing Rayleigh one. Reflectivity distributions with the two scattering theories become similar when, in the Mie one, attenuation is taken into account.

The employment of these different configurations of the EMVORADO operator in the assimilation procedure shows that attenuation has to be taken into account in the simulation of background equivalents of reflectivity measurements. This is an unexpected conclusion since observed reflectivity volumes are already corrected for attenuation. Likely, a compensation of errors arises when taking into account attenuation in the radar operator, probably because the correction for attenuation in observed measurements is prone to large errors.

**4) To evaluate if the assimilation of reflectivity volumes can improve forecast accuracy compared to the current widespread assimilation of estimated precipitation**

The set-up identified in this study for the assimilation of reflectivity volumes is compared to the operational one employed at ARPAE, in which precipitation estimated from the Italian radar composite is assimilated through LHN. The confrontation has been carried out over almost 40 days in September, October and November 2018 and 303 forecasts have been considered. As far as the author knows, this is the most extended comparison ever performed between the two ways of assimilating radar data both in terms of the number of forecasts involved and in terms of the number of verification scores employed.

Results show a statically significant improvement in QPF accuracy when assimilating reflectivity volumes instead of estimated precipitation. On average, the improvement holds up to lead time +7h but it is more remarkable and it lasts longer in forecasts performed in September and October than in those run in November. For the former two months, the positive impact can be observed up to the end of the forecast range (12 hours) while, for the latter month, it completely disappears from lead time +5h. This different behaviour is likely to be associated to the different weather regime observed in each period and, in turns, to the presence or absence of convective equilibrium.

The assimilation of reflectivity volumes also determines a general improvement in upper-air forecast variables. In particular, RMSE for temperature, relative humidity and wind velocity is reduced during a part or the whole forecast range, while the impact on bias is neutral or slightly positive for relative humidity. In

terms of surface variables verification, a slight improvement can be observed for 2-meter temperature, a slight worsening for 2-meter relative humidity and surface pressure while the impact is substantially neutral on the horizontal components of wind velocity.

According to the results obtained, in an operational framework the assimilation of reflectivity volumes is able to outperform the assimilation of radar-estimated precipitation. In light of this result, at ARPAE the assimilation of reflectivity volumes is planned to be implemented operationally in 2020. To achieve this, the comparison with LHN will be extended to some further cases and the procedure to receive and process data in quasi-real time will be implemented. If there will not be hiccups, ARPAE could be the first meteorological centre in the world in which reflectivity volumes will be assimilated in a high resolution NWP model through an EnKF scheme.

# Final remarks and potential improvements

The assimilation of reflectivity volumes through a LETKF scheme is still at a preliminary stage and several aspects needs to be further investigated. Nevertheless, it is already capable to outperform the assimilation of radar-estimated precipitation by LHN, even in an operation framework as that considered in this study. This result is particularly remarkable since LHN has been tested and employed in several NWP models for more than 20 years. In light of this result, even if LHN is very simple to implement, cheap from a computational point of view and provides good results, the assimilation of reflectivity volumes will be the future of convective scale data assimilation due to its wide potential of improvement.

Among the aspects which deserve a deeper investigation and which may lead to a further improvement in the assimilation of radar reflectivities, there are some issues generally associated to the shortening of assimilation cycles. Despite the negative results obtained here, two factors may significantly improve the results in this direction. First of all, it has to be evaluated the impact of using some initialization techniques to remove imbalances in the analyses, such as the Incremental Analysis Update (Bloom et al., 1996) or the divergence adjustment procedure proposed by Hamrud et al. (2015). Secondly, the role of the balance constrains applied

to the analysis, like the hydrostatic balance or the saturation adjustment to avoid super-saturation, has to be evaluated. In particular, the hydrostatic balance has a positive impact in large scale NWP models, but the same is not guaranteed for convective scale data assimilation (Vetra-Carvalho et al., 2012). Even if both initialization and balancing methods play a crucial role for short assimilation cycles, since analysis is computed more frequently, a better characterization of both of them is likely to have a positive impact also for longer cycles.

Another promising direction in order to fully exploit the information on the atmospheric state provided by reflectivity observations is to employ a better characterization of the $\mathbf{R}$ matrix. In fact, as demonstrated in this study, the assumption of a diagonal $\mathbf{R}$ matrix, made in most operational data assimilation systems, is violated when assimilating reflectivities. A possible choice to deal with that is to apply thinning to radar observations in combination with superobbing, as illustrated in Section 6.4. However, the increase of available computational resources in the next years will soon allow to account, at least in part, of error correlations between pair of observations, overcoming the use of a diagonal $\mathbf{R}$.

Finally, as suggested by the results obtained regarding attenuation in the EMVORADO operator, a difficult but important task would be to estimate bias affecting reflectivity observations in order to correct measurements before being assimilated. As explained in Section 7.2, several issues make this bias correction difficult. In particular, biases on reflectivities are likely to be dependent on many factors, like the specifics of the radar station and the weather regime, and it is not clear how to deal with them. However, its characterization, at least in an approximate form, can remarkably enhance the positive impact of assimilating reflectivities.

# Appendix A

# Assimilation of reflectivity volumes in combination with LHN

In the experiments carried out during the *feb2017* period, the assimilation of reflectivity volumes from the four radars of ARPA Piemonte, ARPAL and ARPAE Emilia-Romagna is performed in combination with LHN, for which SRI fields generated from the Italian radar composite are employed. This process is not strictly rigorous since it can be argued that observations from ARPA Piemonte, ARPAL and ARPAE Emilia-Romagna radars are assimilated "twice". Actually, there are several reasons why this approach can be considered valid, as discussed in Section 5.1.1 and in Gastaldo et al. (2018).

In this appendix, it is shown that this choice does not affect substantially the conclusions drawn in Chapter 5 and in Section 6.1. In fact, the assimilation of reflectivities in combination with LHN is performed in all the experiments and, more importantly, results obtained when assimilating reflectivity volumes in combination with LHN do not differ significantly from those obtained when LHN is switched off. In order to demonstrate this, an experiment referred to as *rad60_nolhn* has been run over the *feb2017* period employing the same set-up of *rad60* but without performing LHN. Results of QPF verification in terms of FSS are reported in Figure A.1, in which also the scores of *rad15* and *rad30* experi-

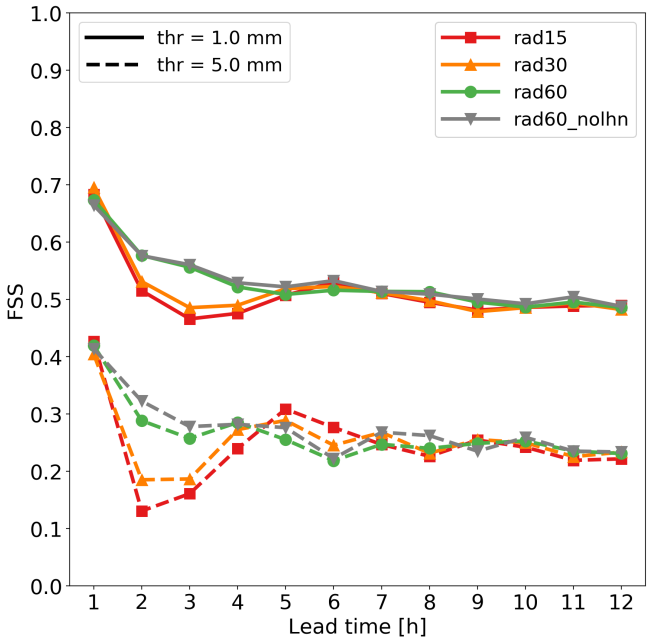


**Figure A.1.** Same as Figure 5.4, but including also scores for the *rad60_nolhn* experiment.

ments are shown to better evaluate the differences among *rad60_nolhn* and *rad60*. In other words, this figure is the same as Figure 5.4 but with the addition of the experiment *rad60_nolhn*.

For the 1 mm threshold, scores for *rad60_nolhn* are essentially identical to those of *rad*. Slight differences among the two experiments can be observed for the 5 mm threshold at lead times +2h, +3h and +8h, but in magnitude they are much smaller than those observable at +2h and +3h among *rad60* and *rad15* or *rad30*. According to these results, the impact of performing LHN over the whole Italian country when reflectivity volumes from radars of ARPA Piemonte, ARPAL and ARPAE Emilia-Romagna are assimilated is substantially neutral.

# List of Figures

# List of Tables

# Bibliography

Aksoy, A., Dowell, D. C., and Snyder, C.: A Multicase Comparative Assessment of the Ensemble Kalman Filter for Assimilation of Radar Observations. Part I: Storm-Scale Analyses, Monthly Weather Review, 137, 1805–1824, https://doi.org/10.1175/2008MWR2691.1, 2009.

Aksoy, A., Dowell, D. C., and Snyder, C.: A Multicase Comparative Assessment of the Ensemble Kalman Filter for Assimilation of Radar Observations. Part II: Short-Range Ensemble Forecasts, Monthly Weather Review, 138, 1273–1292, https://doi.org/10.1175/2009MWR3086.1, 2010.

Anderson, J. L.: An Ensemble Adjustment Kalman Filter for Data Assimilation, Monthly Weather Review, 129, 2884–2903, https://doi.org/10.1175/1520-0493(2001)129<2884:AEAKFF¿2.0.CO;2, 2001.

Anderson, J. L. and Anderson, S. L.: A Monte Carlo Implementation of the Nonlinear Filtering Problem to Produce Ensemble Assimilations and Forecasts, Monthly Weather Review, 127, 2741–2758, https://doi.org/10.1175/1520-0493(1999)127<2741:AMCIOT¿2.0.CO;2, 1999.

Auger, F., Hilairet, M., Guerrero, J. M., Monmasson, E., Orlowska-Kowalska, T., and Katsura, S.: Industrial Applications of the Kalman Filter: A Review, IEEE Transactions on Industrial Electronics, 60, 5458–5471, https://doi.org/10.1109/TIE.2012.2236994, 2013.

Baldauf, M., Seifert, A., Förstner, J., Majewski, D., Raschendorfer, M., and Reinhardt, T.: Operational Convective-Scale Numerical Weather Prediction with the

COSMO Model: Description and Sensitivities, Monthly Weather Review, 139, 3887–3905, https://doi.org/10.1175/MWR-D-10-05013.1, 2011.

Bannister, R. N.: A review of operational methods of variational and ensemble-variational data assimilation, Quarterly Journal of the Royal Meteorological Society, 143, 607–633, https://doi.org/10.1002/qj.2982, 2016.

Bathmann, K.: Justification for estimating observation-error covariances with the Desroziers diagnostic, Quarterly Journal of the Royal Meteorological Society, 144, 1965–1974, https://doi.org/10.1002/qj.3395, 2018.

Battan, L. J.: Radar observation of the atmosphere, University of Chicago Press, 1973.

Benjamin, S. G., Weygandt, S. S., Brown, J. M., Hu, M., Alexander, C. R., Smirnova, T. G., Olson, J. B., James, E. P., Dowell, D. C., Grell, G. A., Lin, H., Peckham, S. E., Smith, T. L., Moninger, W. R., Kenyon, J. S., and Manikin, G. S.: A North American Hourly Assimilation and Model Forecast Cycle: The Rapid Refresh, Monthly Weather Review, 144, 1669–1694, https://doi.org/10.1175/MWR-D-15-0242.1, 2016.

Berner, J., Fossell, K. R., Ha, S.-Y., Hacker, J. P., and Snyder, C.: Increasing the Skill of Probabilistic Forecasts: Understanding Performance Improvements from Model-Error Representations, Monthly Weather Review, 143, 1295–1320, https://doi.org/10.1175/MWR-D-14-00091.1, 2015.

Bick, T., Simmer, C., Trömel, S., Wapler, K., Hendricks Franssen, H.-J., Stephan, K., Blahak, U., Schraff, C., Reich, H., Zeng, Y., and Potthast, R.: Assimilation of 3D radar reflectivities with an ensemble Kalman filter on the convective scale, Quarterly Journal of the Royal Meteorological Society, 142, 1490–1504, https://doi.org/10.1002/qj.2751, 2016.

Bishop, C. H., Etherton, B. J., and Majumdar, S. J.: Adaptive Sampling with the Ensemble Transform Kalman Filter. Part I: Theoretical Aspects, Monthly Weather Review, 129, 420–436, https://doi.org/10.1175/1520-0493(2001)129<0420:ASWTET¿2.0.CO;2, 2001.

Blahak, U.: An Approximation to the Effective Beam Weighting Function for Scanning Meteorological Radars with an Axisymmetric Antenna Pattern, Journal of Atmospheric and Oceanic Technology, 25, 1182–1196, https://doi.org/10.1175/2007JTECHA1010.1, 2008.

Blayo, E., Cosme, E., and Vidard, A.: Introduction to Data Assimilation, Tech. rep., Laboratorie Jean Kuntzmann, 2011.

Bloom, S. C., Takacs, L. L., da Silva, A. M., and Ledvina, D.: Data Assimilation Using Incremental Analysis Updates, Monthly Weather Review, 124, 1256–1271, https://doi.org/10.1175/1520-0493(1996)124<1256:DAUIAU¿2.0.CO;2, 1996.

Bonavita, M., Torrisi, L., and Marcucci, F.: Ensemble data assimilation with the CNMCA regional forecasting system, Quarterly Journal of the Royal Meteorological Society, 136, 132–145, https://doi.org/10.1002/qj.553, 2010.

Bormann, N., Bonavita, M., Dragani, R., Eresmaa, R., Matricardi, M., and McNally, A.: Enhancing the impact of IASI observations through an updated observation-error covariance matrix, Quarterly Journal of the Royal Meteorological Society, 142, 1767–1780, https://doi.org/10.1002/qj.2774, 2016.

Buehner, M., Houtekamer, P. L., Charette, C., Mitchell, H. L., and He, B.: Intercomparison of Variational Data Assimilation and the Ensemble Kalman Filter for Global Deterministic NWP. Part I: Description and Single-Observation Experiments, Monthly Weather Review, 138, 1550–1566, https://doi.org/10.1175/2009MWR3157.1, 2010a.

Buehner, M., Houtekamer, P. L., Charette, C., Mitchell, H. L., and He, B.: Intercomparison of Variational Data Assimilation and the Ensemble Kalman Filter for Global Deterministic NWP. Part II: One-Month Experiments with Real Observations, Monthly Weather Review, 138, 1567–1586, https://doi.org/10.1175/2009MWR3158.1, 2010b.

Burgers, G., Jan van Leeuwen, P., and Evensen, G.: Analysis Scheme in the Ensemble Kalman Filter, Monthly Weather Review, 126, 1719–1724, https://doi.org/10.1175/1520-0493(1998)126<1719:ASITEK¿2.0.CO;2, 1998.

Campbell, W. F., Satterfield, E. A., Ruston, B., and Baker, N. L.: Accounting for Correlated Observation Error in a Dual-Formulation 4D Variational Data Assimilation System, Monthly Weather Review, 145, 1019–1032, https://doi.org/10.1175/MWR-D-16-0240.1, 2017.

Chen, M. and Huang, X.-Y.: Digital Filter Initialization for MM5, Monthly Weather Review, 134, 1222–1236, https://doi.org/10.1175/MWR3117.1, 2006.

Clark, P., Roberts, N., Lean, H., Ballard, S. P., and Charlton-Perez, C.: Convection-permitting models: a step-change in rainfall forecasting, Meteorological Applications, 23, 165–181, https://doi.org/10.1002/met.1538, mET-14-0154.R1, 2016.

Cohn, S. E. and Parrish, D. F.: The Behavior of Forecast Error Covariances for a Kalman Filter in Two Dimensions, Monthly Weather Review, 119, 1757–1785, https://doi.org/10.1175/1520-0493(1991)119<1757:TBOFEC¿2.0.CO;2, 1991.

Courtier, P., Andersson, F., Hackley, W., Vasiljevic, D., Hamrud, M., Hollingsworth, A., Rabier, F., Fisher, M., and Pailleux, J.: The ECMWF implementation of three dimensional variational assimilation (3D-Var). I: Formulation, Quarterly Journal of the Royal Meteorological Society, 124, 1783–1807, https://doi.org/10.1002/qj.49712455002, 1998.

Craig, G. C., Keil, C., and Leuenberger, D.: Constraints on the impact of radar rainfall data assimilation on forecasts of cumulus convection, Quarterly Journal of the Royal Meteorological Society, 138, 340–352, https://doi.org/10.1002/qj.929, 2012.

Cuo, L., Pagano, T. C., and Wang, Q. J.: A Review of Quantitative Precipitation Forecasts and Their Use in Short- to Medium-Range Streamflow Forecasting, Journal of Hydrometeorology, 12, 713–728, 2011.

Davies, H. C.: A lateral boundary formulation for multi-level prediction models, Quarterly Journal of the Royal Meteorological Society, 102, 405–418, https://doi.org/10.1002/qj.49710243210, 1976.

Davolio, S. and Buzzi, A.: A Nudging Scheme for the Assimilation of Precipitation Data into a Mesoscale Model, Weather and Forecasting, 19, 855–871, https://doi.org/10.1175/1520-0434(2004)019<0855:ANSFTA¿2.0.CO;2, 2004.

Davolio, S., Silvestro, F., and Gastaldo, T.: Impact of Rainfall Assimilation on High-Resolution Hydrometeorological Forecasts over Liguria, Italy, Journal of Hydrometeorology, 18, 2659–2680, https://doi.org/10.1175/JHM-D-17-0073.1, 2017.

Desroziers, G., Berre, L., Chapnik, B., and Poli, P.: Diagnosis of observation, background and analysis-error statistics in observation space, Quarterly Journal of the Royal Meteorological Society, 131, 3385–3396, https://doi.org/10.1256/qj.05.108, 2005.

Dixon, M., Li, Z., Lean, H., Roberts, N., and Ballard, S.: Impact of Data Assimilation on Forecasting Convection over the United Kingdom Using a High-Resolution Version of the Met Office Unified Model, Monthly Weather Review, 137, 1562–1584, https://doi.org/10.1175/2008MWR2561.1, 2009.

Doms, G. and Baldauf, M.: A Description of the Nonhydrostatic Regional COSMO Model, Part I: Dynamics and Numerics, Tech. rep., 2018.

Doms, G., Förstner, J., Heise, E., Herzog, H.-J., Mironov, D., Raschendorfer, M., Reinhardt, T., Ritter, B., Schrodin, R., Schulz, J.-P., and Vogel, G.: A Description of the Nonhydrostatic Regional COSMO Model, Part II: Physical Parameterization, Tech. rep., 2011.

Done, J. M., Craig, G. C., Gray, S. L., Clark, P. A., and Gray, M. E. B.: Mesoscale simulations of organized convection: Importance of convective equilibrium, Quarterly Journal of the Royal Meteorological Society, 132, 737–756, https://doi.org/10.1256/qj.04.84, 2006.

Dong, J. and Xue, M.: Assimilation of radial velocity and reflectivity data from coastal WSR-88D radars using an ensemble Kalman filter for the analysis and forecast of landfalling hurricane Ike (2008), Quarterly Journal of the Royal Meteorological Society, 139, 467–487, https://doi.org/10.1002/qj.1970, 2013.

Dowell, D., Zhang, F., Wicker, L., Snyder, C., and Crook, N.: Wind and Tempeture retrievals in the 17 May 1981 Arcadia, Oklahoma, supercell: Ensemble Kalman filter experiments, Monthly Weather Review, 132, 1982–2005, https://doi.org/10.1175/1520-0493(2004)132<1982:WATRIT¿2.0.CO;2, 2004.

Dowell, D. C., Wicker, L. J., and Snyder, C.: Ensemble Kalman Filter Assimilation of Radar Observations of the 8 May 2003 Oklahoma City Supercell: Influences of Reflectivity Observations on Storm-Scale Analyses, Monthly Weather Review, 139, 272–294, https://doi.org/10.1175/2010MWR3438.1, 2011.

Ebert, E. E.: Fuzzy verification of high-resolution gridded forecasts: a review and proposed framework, Meteorological Applications, 15, 51–64, https://doi.org/10.1002/met.25, 2008.

Efron, B. and Tibshirani, R.: An Introduction to the Bootstrap, Chapman & Hall, 1994.

Emanuel, K.: Atmospheric Convection, Oxford University Press, 1994.

Errico, R. M.: Spectra Computed from a Limited Area Grid, Monthly Weather Review, 113, 1554–1562, https://doi.org/10.1175/1520-0493(1985)113<1554:SCFALA¿2.0.CO;2, 1985.

Evensen, G.: Using the extended Kalman filter with a multilayer quasi-geostrophic ocean model, Journal of Geophysical Research: Oceans, 97, 17 905–17 924, https://doi.org/10.1029/92JC01972, 1992.

Evensen, G.: Sequential data assimilation with a nonlinear quasi-geostrophic model using Monte Carlo methods to forecast error statistics, J. Geophys. Res, 99, 10 143–10 162, 1994.

Ferting, E. J., Harlim, J., and Hunt, B. R.: A comparative study of 4D-VAR and a 4D Ensemble Kalman Filter: perfect model simulations with Lorenz-96, Tellus A, 59, 96–100, https://doi.org/10.1111/j.1600-0870.2006.00205.x, 2007.

Gal-Chen, T. and Somerville, R. C. J.: On the use of a coordinate transformation for the solution of the Navier-Stokes equations, J. Comput. Phys., 17, 209–228, https://doi.org/10.1016/0021-9991(75)90037-6, 1975.

Gardiner, C. W.: Handbook of Stochastic Methods,, Spinger, 2 edn., 1985.

Gaspari, G. and Cohn, S. E.: Construction of correlation functions in two and three dimensions, Quarterly Journal of the Royal Meteorological Society, 125, 723–757, https://doi.org/10.1002/qj.49712555417, 1999.

Gastaldo, T., Poli, V., Marsigli, C., Alberoni, P. P., and Paccagnella, T.: Data assimilation of radar reflectivity volumes in a LETKF scheme, Nonlinear Processes in Geophysics, 25, 747–764, https://doi.org/10.5194/npg-25-747-2018, 2018.

Ghil, M. and Malanotte-Rizzoli, P.: Data Assimilation in Meteorology and Oceanography, vol. 33 of *Advances in Geophysics*, pp. 141–266, Elsevier, https://doi.org/10.1016/S0065-2687(08)60442-2, 1991.

Gustafsson, N., Janjić, T., Schraff, C., Leuenberger, D., Weissmann, M., Reich, H., Brousseau, P., Montmerle, T., Wattrelot, E., Bučánek, A., Mile, M., Hamdi, R., Lindskog, M., Barkmeijer, J., Dahlbom, M., Macpherson, B., Ballard, S., Inverarity, G., Carley, J., Alexander, C., Dowell, D., Liu, S., Ikuta, Y., and Fujita, T.: Survey of data assimilation methods for convective-scale numerical weather prediction at operational centres, Quarterly Journal of the Royal Meteorological Society, 144, 1218–1256, https://doi.org/10.1002/qj.3179, 2018.

Hamill, T. M.: Ensemble-based atmospheric data assimilation, in: Predictability of Weather and Climate, chap. 6, pp. 124–156, Cambridge Press, 2006.

Hamrud, M., Bonavita, M., and Isaksen, L.: EnKF and Hybrid Gain Ensemble Data Assimilation. Part I: EnKF Implementation, Monthly Weather Review, 143, 4847–4864, https://doi.org/10.1175/MWR-D-14-00333.1, 2015.

Harnisch, F. and Keil, C.: Initial Conditions for Convective-Scale Ensemble Forecasting Provided by Ensemble Data Assimilation, Monthly Weather Review, 143, 1583–1600, https://doi.org/10.1175/MWR-D-14-00209.1, 2015.

Higham, N. J.: Computing the nearest correlation matrix—a problem from finance, IMA Journal of Numerical Analysis, 22, 329–343, https://doi.org/10.1093/imanum/22.3.329, 2002.

Houtekamer, P. L. and Mitchell, H. L.: Data Assimilation Using an Ensemble Kalman Filter Technique, Monthly Weather Review, 126, 796–811, https://doi.org/10.1175/1520-0493(1998)126<0796:DAUAEK>2.0.CO;2, 1998.

Houtekamer, P. L. and Mitchell, H. L.: A Sequential Ensemble Kalman Filter for Atmospheric Data Assimilation, Monthly Weather Review, 129, 123–137, https://doi.org/10.1175/1520-0493(2001)129<0123:ASEKFF>2.0.CO;2, 2001.

Houtekamer, P. L. and Mitchell, H. L.: Ensemble Kalman filtering, Quarterly Journal of the Royal Meteorological Society, 131, 3269–3289, https://doi.org/10.1256/qj.05.135, 2005.

Houtekamer, P. L. and Zhang, F.: Review of the Ensemble Kalman Filter for Atmospheric Data Assimilation, Monthly Weather Review, 144, 4489–4532, https://doi.org/10.1175/MWR-D-15-0440.1, 2016.

Houtekamer, P. L., Mitchell, H. L., Pellerin, G., Buehner, M., Charron, M., Spacek, L., and Hansen, B.: Atmospheric Data Assimilation with an Ensemble Kalman Filter: Results with Real Observations, Monthly Weather Review, 133, 604–620, https://doi.org/10.1175/MWR-2864.1, 2005.

Hunt, B. R., Kostelich, E. J., and Szunyogh, I.: Efficient data assimilation for spatiotemporal chaos: A local ensemble transform Kalman filter, Physica D: Nonlinear Phenomena, 230, 112–126, https://doi.org/10.1016/j.physd.2006.11.008, data Assimilation, 2007.

Janjić, T., Bormann, N., Bocquet, M., Carton, J. A., Cohn, S. E., Dance, S. L., Losa, S. N., Nichols, N. K., Potthast, R., Waller, J. A., and Weston, P.: On the representation error in data assimilation, Quarterly Journal of the Royal Meteorological Society, 144, 1257–1278, https://doi.org/10.1002/qj.3130, 2017.

Jazwinski, A.: Stochastic processes and filtering theory, no. 64 in Mathematics in science and engineering, Acad. Press, New York, 1970.

Jones, C. D. and Macpherson, B.: A latent heat nudging scheme for the assimilation of precipitation data into an operational mesoscale model, Meteorological Applications, 4, 269–277, https://doi.org/10.1017/S1350482797000522, 1997.

Jung, Y., Xue, M., and Tong, M.: Ensemble Kalman Filter Analyses of the 29–30 May 2004 Oklahoma Tornadic Thunderstorm Using One- and Two-Moment Bulk Microphysics Schemes, with Verification against Polarimetric Radar Data, Monthly Weather Review, 140, 1457–1475, https://doi.org/10.1175/MWR-D-11-00032.1, 2012.

Kalman, R. E.: A new approach to linear filtering and prediction problems, Journal of basic Engineering, 82, 35–45, 1960.

Keil, C., Heinlein, F., and Craig, G. C.: The convective adjustment time-scale as indicator of predictability of convective precipitation, Quarterly Journal of the Royal Meteorological Society, 140, 480–490, https://doi.org/10.1002/qj.2143, 2014.

Koinstinen, J. and Puhakka, T.: An improved spatial gauge-radar ad-justment technique, in: Proc. $20^{th}$ Conference on Radar Meteorology, pp. 179–186, AMS, 1981.

Lange, H. and Craig, G. C.: The Impact of Data Assimilation Length Scales on Analysis and Prediction of Convective Storms, Monthly Weather Review, 142, 3781–3808, https://doi.org/10.1175/MWR-D-13-00304.1, 2014.

Leuenberger, D. and Rossa, A.: Revisiting the latent heat nudging scheme for the rainfall assimilation in convective system, in: Proc. of $3^{th}$ European Radar Conference on Radar Meteorology and Hydrology (ERAD), pp. 162–167, Visby, Gotland, Sweden, 6–10 September, 2004.

Leuenberger, D. and Rossa, A.: Revisiting the latent heat nudging scheme for the rainfall assimilation of a simulated convective storm, Meteorol. Atmos. Phys., 98, 195–215, 2007.

Marshall, J. S. and Palmer, W. M. K.: The distribuition of raindrop with size, Journal of Meteorology, 5, 165–166, https://doi.org/10.1175/1520-0469(1948)005<0165:TDORWS>2.0.CO;2, 1948.

Meng, Z. and Zhang, F.: Limited-Area Ensemble-Based Data Assimilation, Monthly Weather Review, 139, 2025–2045, https://doi.org/10.1175/2011MWR3418.1, 2011.

Michelson, D.: Quality Control of Weather Radar Data for Quantitative Application, Ph.D. thesis, University of Salford, 2003.

Michelson, D., Einfalt, T., Holleman, I., Gjertsen, U., Friedrich, K., Haase, G., Lindskog, M., and Jurczyk, A.: Weather radar data quality in Europe – quality control and characterization, Tech. rep., COST Action 717, 2005.

Mie, G.: Beiträge zur Optik trüber Medien, speziell kolloidaler Metallösungen, Annalen der Physik, 330, 377–445, https://doi.org/10.1002/andp.19083300302, 1908.

Mitchell, H. L., Houtekamer, P. L., and Pellerin, G.: Ensemble Size, Balance, and Model-Error Representation in an Ensemble Kalman Filter, Monthly Weather Review, 130, 2791–2808, https://doi.org/10.1175/1520-0493(2002)130<2791:ESBAME>2.0.CO;2, 2002.

Miyoshi, T., Sato, Y., and Kadowaki, T.: Ensemble Kalman Filter and 4D-Var Intercomparison with the Japanese Operational Global Analysis and Prediction System, Monthly Weather Review, 138, 2846–2866, https://doi.org/10.1175/2010MWR3209.1, 2010.

Nastrom, G. D. and Gage, K. S.: A Climatology of Atmospheric Wavenumber Spectra of Wind and Temperature Observed by Commercial Aircraft, Journal of the Atmospheric Sciences, 42, 950–960, https://doi.org/10.1175/1520-0469(1985)042<0950:ACOAWS>2.0.CO;2, 1985.

Nichols, N. K.: Mathematical concepts of data assimilation, in: Data Assimilation: Making Sense of Observations, pp. 13–39, Springer, 2010.

Oguchi, T.: Electromagnetic wave propagation and scattering in rain and other hydrometeors, Proceedings of the IEEE, 71, 1029–1078, https://doi.org/10.1109/PROC.1983.12724, 1983.

Ott, E., Hunt, B. R., Szunyogh, I., Zimin, A. V., Kostelich, E. J., Corazza, M., Kalnay, E., Patil, D., and Yorke, J. A.: A local ensemble Kalman filter for atmospheric data assimilation, Tellus A: Dynamic Meteorology and Oceanography, 56, 415–428, https://doi.org/10.3402/tellusa.v56i5.14462, 2004.

Raghavan, S.: Radar Meteorology, Atmospheric and Oceanographic Sciences Library, Springer Netherlands, 2003.

Rainwater, S., Bishop, C. H., and Campbell, W. F.: The benefits of correlated observation errors for small scales, Quarterly Journal of the Royal Meteorological Society, 141, 3439–3445, https://doi.org/10.1002/qj.2582, 2015.

Raschendorfer, M.: The new turbulence parametrization of LM, COSMO newsletter, 1, 89–97, 2001.

Rinehart, R.: Radar for Meteorologists: You, Too Can be a Radar Meteorologist, pt. 3, Department of Atmospheric Sciences, University of North Dakota, 1990.

Rinollo, A., Vulpiani, G., Puca, S., Pagliara, P., Kaňák, J., Lábó, E., Okon, L., Roulin, E., Baguis, P., Cattani, E., Laviola, S., and Levizzani, V.: Definition and impact of a quality index for radar-based reference measurements in the H-SAF precipitation product validation, Natural Hazards and Earth System Sciences, 13, 2695–2705, https://doi.org/10.5194/nhess-13-2695-2013, 2013.

Ritter, B. and Geleyn, J.-F.: A Comprehensive Radiation Scheme for Numerical Weather Prediction Models with Potential Applications in Climate Simulations, Monthly Weather Review, 120, 303–325, https://doi.org/10.1175/1520-0493(1992)120<0303:ACRSFN>2.0.CO;2, 1992.

Roberts, N. M. and Lean, H. W.: Scale-Selective Verification of Rainfall Accumulations from High-Resolution Forecasts of Convective Events, Monthly Weather Review, 136, 78–97, https://doi.org/10.1175/2007MWR2123.1, 2008.

Roebber, P. J.: Visualizing Multiple Measures of Forecast Quality, Weather and Forecasting, 24, 601–608, https://doi.org/10.1175/2008WAF2222159.1, 2009.

Röpnack, A., Hense, A., Gebhardt, C., and Majewski, D.: Bayesian Model Verification of NWP Ensemble Forecasts, Monthly Weather Review, 141, 375–387, https://doi.org/10.1175/MWR-D-11-00350.1, 2013.

Rossa, A., Nurmi, P., and Ebert, E.: Overview of methods for the verification of quantitative precipitation forecasts, pp. 419–452, Springer Berlin Heidelberg, Berlin, Heidelberg, https://doi.org/10.1007/978-3-540-77655-0_16, 2008.

Sauvageot, H.: Rainfall measurement by radar: a review, Atmospheric Research, 35, 27–54, https://doi.org/10.1016/0169-8095(94)90071-X, 1994.

Schär, C., Leuenberger, D., Fuhrer, O., Lüthi, D., and Girard, C.: A New Terrain-Following Vertical Coordinate Formulation for Atmospheric Prediction Models, Monthly Weather Review, 130, 2459–2480, https://doi.org/10.1175/1520-0493(2002)130<2459:ANTFVC>2.0.CO;2, 2002.

Schraff, C., Reich, H., Rhodin, A., Schomburg, A., Stephan, K., Periáñez, A., and Potthast, R.: Kilometre-scale ensemble data assimilation for the COSMO model (KENDA), Quarterly Journal of the Royal Meteorological Society, 142, 1453–1472, https://doi.org/10.1002/qj.2748, 2016.

Skamarock, W. C.: Evaluating Mesoscale NWP Models Using Kinetic Energy Spectra, Monthly Weather Review, 132, 3019–3032, https://doi.org/10.1175/MWR2830.1, 2004.

Snook, N., Xue, M., and Jung, Y.: Multiscale EnKF Assimilation of Radar and Conventional Observations and Ensemble Forecasting for a Tornadic Mesoscale Convective System, Monthly Weather Review, 143, 1035–1057, https://doi.org/10.1175/MWR-D-13-00262.1, 2015.

Snyder, C.: Introduction to the Kalman filter, in: Advanced Data Assimilation for Geosciences: Lecture Notes of the Les Houches School of Physics: Special Issue, June 2012, pp. 75–120, Oxford Scholarship Online, 2015.

Sobash, R. A. and Stensrud, D. J.: The Impact of Covariance Localization for Radar Data on EnKF Analyses of a Developing MCS: Observing System Simu-

lation Experiments, Monthly Weather Review, 141, 3691–3709, https://doi.org/10.1175/MWR-D-12-00203.1, 2013.

Sokol, Z.: Effects of an assimilation of radar and satellite data on a very-short range forecast of heavy convective rainfalls, Atmospheric Research, 93, 188–206, https://doi.org/10.1016/j.atmosres.2008.11.001, 4th European Conference on Severe Storms, 2009.

Stauffer, D. R. and Seaman, N. L.: Use of Four-Dimensional Data Assimilation in a Limited-Area Mesoscale Model. Part I: Experiments with Synoptic-Scale Data, Monthly Weather Review, 118, 1250–1277, https://doi.org/10.1175/1520-0493(1990)118<1250:UOFDDA>2.0.CO;2, 1990.

Stephan, K., Klink, S., and Schraff, C.: Assimilation of radar-derived rain rates into the convective-scale model COSMO-DE at DWD, Quarterly Journal of the Royal Meteorological Society, 134, 1315–1326, https://doi.org/10.1002/qj.269, 2008.

Stewart, L. M., Dance, S. L., Nichols, N. K., Eyre, J. R., and Cameron, J.: Estimating interchannel observation-error correlations for IASI radiance data in the Met Office system†, Quarterly Journal of the Royal Meteorological Society, 140, 1236–1244, https://doi.org/10.1002/qj.2211, 2014.

Szturc, J., Ośródka, K., and Jurczyk, A.: Quality Control Algorithms Applied on Weather Radar Reflectivity Data, in: Doppler Radar Observations, chap. 12, IntechOpen, Rijeka, https://doi.org/10.5772/39000, 2012.

Talagrand, O.: Assimilation of Observations, an Introduction (Special Issue Data Assimilation in Meteology and Oceanography: Theory and Practice), Journal of the Meteorological Society of Japan. Ser. II, 75, 191–209, https://doi.org/10.2151/jmsj1965.75.1B_191, 1997.

Tiedtke, M.: A Comprehensive Mass Flux Scheme for Cumulus Parameterization in Large-Scale Models, Monthly Weather Review, 117, 1779–1800, https://doi.org/10.1175/1520-0493(1989)117<1779:ACMFSF>2.0.CO;2, 1989.

Tippett, M. K., Anderson, J. L., Bishop, C. H., Hamill, T. M., and Whitaker, J. S.: Ensemble Square Root Filters, Monthly Weather Review, 131, 1485–1490, https://doi.org/10.1175/1520-0493(2003)131<1485:ESRF>2.0.CO;2, 2003.

Tong, M. and Xue, M.: Ensemble Kalman Filter Assimilation of Doppler Radar Data with a Compressible Nonhydrostatic Model: OSS Experiments, Monthly Weather Review, 133, 1789–1807, https://doi.org/10.1175/MWR2898.1, 2005.

Van Leeuwen, P. J.: Particle Filtering in Geophysical Systems, Monthly Weather Review, 137, 4089–4114, https://doi.org/10.1175/2009MWR2835.1, 2009.

Vetra-Carvalho, S., Dixon, M., Migliorini, S., Nichols, N. K., and Ballard, S. P.: Breakdown of hydrostatic balance at convective scales in the forecast errors in the Met Office Unified Model, Quarterly Journal of the Royal Meteorological Society, 138, 1709–1720, https://doi.org/10.1002/qj.1925, 2012.

Vulpiani, G., Montopoli, M., Passeri, L. D., Gioia, A. G., Giordano, P., and Marzano, F. S.: On the Use of Dual-Polarized C-Band Radar for Operational Rainfall Retrieval in Mountainous Areas, Journal of Applied Meteorology and Climatology, 51, 405–425, https://doi.org/10.1175/JAMC-D-10-05024.1, 2012.

Waller, J. A., Simonin, D., Dance, S. L., Nichols, N. K., and Ballard, S. P.: Diagnosing Observation Error Correlations for Doppler Radar Radial Winds in the Met Office UKV Model Using Observation-Minus-Background and Observation-Minus-Analysis Statistics, Monthly Weather Review, 144, 3533–3551, https://doi.org/10.1175/MWR-D-15-0340.1, 2016.

Waller, J. A., Dance, S. L., and Nichols, N. K.: On diagnosing observation-error statistics with local ensemble data assimilation, Quarterly Journal of the Royal Meteorological Society, 143, 2677–2686, https://doi.org/10.1002/qj.3117, 2017.

Wattrelot, E., Caumont, O., and Mahfouf, J.-F.: Operational Implementation of the 1D+3D-Var Assimilation Method of Radar Reflectivity Data in the AROME Model, Monthly Weather Review, 142, 1852–1873, https://doi.org/10.1175/MWR-D-13-00230.1, 2014.

Wernli, H., Paulat, M., Hagen, M., and Frei, C.: SAL—A Novel Quality Measure for the Verification of Quantitative Precipitation Forecasts, Monthly Weather Review, 136, 4470–4487, https://doi.org/10.1175/2008MWR2415.1, 2008.

Wernli, H., Hofmann, C., and Zimmer, M.: Spatial Forecast Verification Methods Intercomparison Project: Application of the SAL Technique, Weather and Forecasting, 24, 1472–1484, https://doi.org/10.1175/2009WAF2222271.1, 2009.

Weston, P. P., Bell, W., and Eyre, J. R.: Accounting for correlated error in the assimilation of high-resolution sounder data, Quarterly Journal of the Royal Meteorological Society, 140, 2420–2429, https://doi.org/10.1002/qj.2306, 2014.

Whitaker, J. S. and Hamill, T. M.: Ensemble Data Assimilation without Perturbed Observations, Monthly Weather Review, 130, 1913–1924, https://doi.org/10.1175/1520-0493(2002)130<1913:EDAWPO>2.0.CO;2, 2002.

Wicker, L. J. and Skamarock, W. C.: Time-Splitting Methods for Elastic Models Using Forward Time Schemes, Monthly Weather Review, 130, 2088–2097, https://doi.org/10.1175/1520-0493(2002)130<2088:TSMFEM>2.0.CO;2, 2002.

Wilson, J. W. and Brandes, E. A.: Radar Measurement of Rainfall—A Summary, Bulletin of the American Meteorological Society, 60, 1048–1060, https://doi.org/10.1175/1520-0477(1979)060<1048:RMORS>2.0.CO;2, 1979.

Wu, W.-S., Parrish, D. F., Rogers, E., and Lin, Y.: Regional Ensemble–Variational Data Assimilation Using Global Ensemble Forecasts, Weather and Forecasting, 32, 83–96, https://doi.org/10.1175/WAF-D-16-0045.1, 2017.

Xue, M., Tong, M., and Droegemeier, K. K.: An OSSE Framework Based on the Ensemble Square Root Kalman Filter for Evaluating the Impact of Data from Radar Networks on Thunderstorm Analysis and Forecasting, Journal of Atmospheric and Oceanic Technology, 23, 46, https://doi.org/10.1175/JTECH1835.1, 2006.

Yang, S.-C., Kalnay, E., Hunt, B., and Neill, E. B.: Weight interpolation for efficient data assimilation with the Local Ensemble Transform Kalman Filter, Quar-

terly Journal of the Royal Meteorological Society, 135, 251–262, https://doi.org/10.1002/qj.353, 2009.

Zawadzki, I. I.: Statistical Properties of Precipitation Patterns, Journal of Applied Meteorology, 12, 459–472, https://doi.org/10.1175/1520-0450(1973)012<0459:SPOPP>2.0.CO;2, 1973.

Zeng, Y.: Efficient Radar Forward Operator for Operational Data Assimilation within the COSMO-model, Ph.D. thesis, Institute of Meteorology and Climate Research of the Karlsruhe Institute of Technology, 2013.

Zeng, Y., Blahak, U., and Jerger, D.: An efficient modular volume-scanning radar forward operator for NWP models: description and coupling to the COSMO model, Quarterly Journal of the Royal Meteorological Society, 142, 3234–3256, https://doi.org/10.1002/qj.2904, 2016.

Zhang, F., Snyder, C., and Sun, J.: Impacts of Initial Estimate and Observation Availability on Convective-Scale Data Assimilation with an Ensemble Kalman Filter, Monthly Weather Review, 132, 1238–1253, https://doi.org/10.1175/1520-0493(2004)132<1238:IOIEAO>2.0.CO;2, 2004.

# Acknowledgements

I am grateful to the several people who contributed to the development of this thesis. First of all, I want to thank my supervisor Dr. Chiara Marsigli for all the time she dedicated to me and for allowing me to approach the world of research. Moreover, I am particularly grateful to her since she was always available to discuss ideas and to encourage my work, guiding me with wisdom but leaving me room to work in my own way. At the same time, I want to express my gratitude to all the people of the numerical weather prediction team of ARPAE, for the constant support they gave to me in various forms. A special mention goes to Dr. Virginia Poli with whom it has been a great pleasure to work both from a personal point of view and for how she enriched me professionally. I also want to thank particularly Dr. Tiziana Paccagnella for the constant encouragement and assistance. Regarding ARPAE people, I am grateful also to people of the radar group for providing data and support, as well as to Dr. Maria Stefania Tesini for her help about verification.

My sincere gratitude also goes to Prof. Federico Porcù and to Prof. Rolando Rizzi for their assistance from the University of Bologna. In particular, I want to thank the former for reviewing the thesis and for the useful discussions on radar measurements and their processing. I want also to thank the data assimilation colleagues of the COSMO consortium with whom it was particularly fruitful to discuss the results of the thesis. Furthermore, I am grateful to Environment and Climate Change Canada for giving me the chance to work with its data assimilation group and in particular to Dr. Peter Houtekamer for supervising me during this internship. Moreover, I am grateful to both DPC and to ARPA Piemonte for providing radar data. Finally, I want to thank both University of Bologna and ARPAE for funding this work.